Modeling of Diesel injection in subcritical and supercritical conditions

Songzhi Yang

▶ **To cite this version:**

Songzhi Yang. Modeling of Diesel injection in subcritical and supercritical conditions. Fluids mechanics [physics.class-ph]. Université Paris Saclay (COmUE), 2019. English. NNT : 2019SACLC045 . tel-02296577

HAL Id: tel-02296577
https://theses.hal.science/tel-02296577

Submitted on 25 Sep 2019

HAL is a multi-disciplinary open access archive for the deposit and dissemination of scientific research documents, whether they are published or not. The documents may come from teaching and research institutions in France or abroad, or from public or private research centers.

L'archive ouverte pluridisciplinaire **HAL**, est destinée au dépôt et à la diffusion de documents scientifiques de niveau recherche, publiés ou non, émanant des établissements d'enseignement et de recherche français ou étrangers, des laboratoires publics ou privés.

NNT : 2019SACLC045

Modelling of Diesel injection in subcritical and supercritical conditions

Thèse de doctorat de l'Université Paris-Saclay
préparée à CentraleSupélec

École doctorale n°579 : Sciences mécaniques et énergétiques, matériaux et géosciences (SMEMAG)
Spécialité de doctorat : Mécanique des fluides

Thèse présentée et soutenue à Rueil Malmaison, le 5 juillet 2019 par

Songzhi Yang

Composition du Jury :

Richard SAUREL Professeur, Aix-Marseille Université, France	Président
Manolis GAVAISES Professeur, City University of London, UK	Rapporteur
Xiangyu HU Professeur, Technical University of Munich, Germany	Rapporteur
Thomas SCHMITT Docteur, Université Paris-Saclay (EM2C) ,France	Examinateur
Angela DI LELLA Docteur, IFPEN, France	Examinateur
Chaouki HABCHI Docteur, HDR, IFPEN, France	Directeur de thèse

Thèse de doctorat

ÉCOLE DOCTORALE
Sciences mécaniques et énergétiques, matériaux et géosciences (SMEMAG)

Titre : Modélisation de l'injection Diesel dans des conditions sous-critiques et supercritiques

Mots clés : écoulement diphasique compressible, Peng-Robinson EoS, cavitation, injection transcritiques

Résumé : Pour satisfaire aux dernières réglementations en matière d'émissions, des progrès importants sont encore attendus des moteurs à combustion interne. De plus, améliorer l'efficacité du moteur pour réduire les émissions et la consommation de carburant est devenu plus essentiel qu'auparavant. Mais, de nombreux phénomènes complexes restent mal compris dans ce domaine, tels que le processus d'injection de carburant. Nombreux logiciels pour la dynamique des fluides numérique (CFD) prenant en compte le changement de phase (comme la cavitation) et la modélisation de l'injection ont été développés et utilisés avec succès dans le processus d'injection. Néanmoins, il existe peu de codes CFD capables de simuler avec précision des conditions d'injection transcritiques, à partir d'une condition de température de carburant sous-critique vers un mélange supercritique dans la chambre de combustion. En effet, la plupart des modèles existants peuvent simuler des écoulements à phase unique, éventuellement dans des conditions supercritiques, ou des écoulements diphasiques dans des conditions sous-critiques. Par conséquent, il manque un modèle complet capable de traiter les conditions transcritiques, y compris la transition de phase possible entre les régimes souscritiques et supercritiques, Plus précisément, un modèle à 6-équation entièrement compressibles incluant les équations de bilan des phases liquide et gazeuse résolues séparément ; et un modèle à 4-équation qui résout les équations des bilans liquide et gazeux en équilibre mécanique et thermique sont proposés dans ce manuscrit. L'équation d'état Peng-Robinson EoS est sélectionné pour fermer les deux systèmes et pour faire face aux éventuels changements de phase et à la transition ou à la séparation des phases. En particulier, un solveur d'équilibre de phase a été développé et validé. Ensuite, une série de tests académiques 1D portant sur les phénomènes d'évaporation et de condensation effectués dans des conditions sous-critiques et supercritiques a été simulée et comparée aux données de la littérature et aux résultats académiques disponibles. Ensuite, les modèles d'écoulement en deux phases entièrement compressibles (systèmes à 6-équation et à 4- équation) ont été utilisés pour simuler les phénomènes de cavitation dans une buse 3D de taille réelle afin d'étudier l'effet de l'azote dissous sur la création et le développement de la cavitation. Le bon accord avec les données expérimentales prouve que le solveur proposé est capable de gérer le comportement

Université Paris-Saclay
Espace Technologique / Immeuble Discovery
Route de l'Orme aux Merisiers RD 128 / 91190 Saint-Aubin, France

ou entre les écoulements monophasiques et diphasiques, de manière dynamique. Cette thèse a pour objectif de relever ce défi.Pour cela, des modèles d'écoulement diphasique compressible de fluide réel basés sur une approche eulérienne-eulérienne avec prise en compte de l'équilibre de phase ont été développés et discutés dans le présent travail.

complexe du changement de phase dans des conditions sous-critiques. Enfin, la capacité du solveur à traiter l'injection transcritique à des pressions et températures élevées a été validée par la modélisation réussie de l'injecteur Spray A du réseau de combustion moteur (ECN).

Title : Modelling of Diesel injection in subcritical and supercritical conditions

Keywords : compressible two phase flow, Peng-Robinson EoS, cavitation, transcritical injection

Abstract: To satisfy the stringent emission regulations, important progress is still be expected from internal combustion engines. In addition, improving engine efficiency to reduce the emission and fuel consumption has become more essential than before. But many complex phenomena remain poorly understood in this field, such as the fuel injection process. Numerous software programs for computational fluid dynamics (CFD) considering phase change (such as cavitation) and injection modelling, have been developed and used successfully in the injection process. Nevertheless, there are few CFD codes able to simulate correctly transcritical conditions starting from a subcritical fuel temperature condition towards a supercritical mixture in the combustion chamber. Indeed, most of the existing models can simulate either single-phase flows possibly in supercritical condition or two-phase flows in subcritical condition; lacking therefore, a comprehensive model which can deal with transcritical condition including possible phase transition from subcritical to supercritical regimes, or from single-phase to two-phase flows, dynamically. This thesis aims at dealing with this challenge. For that, real fluid compressible two-phase flow models based on Eulerian-Eulerian approach with the consideration of phase equilibrium have been developed and discussed in the present work.

More precisely, a fully compressible 6-equation model including liquid and gas phases balance equations solved separately; and a 4-equation model which solves the liquid and gas balance equations in mechanical and thermal equilibrium, are proposed in this manuscript. The Peng-Robinson equation of state (EoS) is selected to close both systems and to deal with the eventual phase change or phase transition. Particularly, a phase equilibrium solver has been developed and validated. Then, a series of 1D academic tests involving the evaporation and condensation phenomena performed under subcritical and supercritical conditions have been simulated and compared with available literature data and analytical results. Then the fully compressible two-phase flow models (6-Equation and 4-Equation systems) have been employed to simulate the cavitation phenomena in a real size 3D nozzle to investigate the effect of dissolved N_2 on the inception and developing of cavitation. The good agreement with experimental data proves the solver can handle the complex phase change behavior in subcritical condition. Finally, the capability of the solver in dealing with the transcritical injection at high pressure and temperature conditions has been further validated through the successful modelling of the engine combustion network (ECN) Spray A injector.

Acknowledgement

Firstly, I would like to convey my most gratitude and thanks to my advisors, Dr. Chaouki Habchi and Dr. Rafael Lugo for their considerable, valuable, continuous guidance and encouragement during my Ph.D study. May Rafael rest in peace. I have learnt a lot from them not only in the knowledge side, most importantly, the manner of doing research and the attitude of working as a team. I believe all these traits will positively influence my future career. I would like to thank Dr. Ping Yi for her help in developing four-equation model. I also convey my sincere thanks to Prof. Jean-Charles de Hemptinne, Dr. Di Lella Angela and Dr. Pascal Mougin for giving valuable guidances in the development of thermodynamics model, as well as to new Ph.D student Jafari Sajad for his help in carefully reviewing the paper or manuscript.

Secondly, I would like to thank the colleagues in IFPEN, especially in previous R102 department. To name but a few, I would like to thank Kumar Rajesh for his generous help in preparing the injectors mesh. I also express my sincere thanks to Dr. Christian Angelberger, Dr. Julien Bohbot, Dr. Nicolas Gillet, Dr. Benjamin Reveille, Dr. Louis-Marie Malbec and Dr. Anthony Velghe for their technical help and guidance during the thesis. I would like to thank Zhihao Ding for helping me solve the python problems. Special thanks are given to Dr. Gilles Bruneaux for his help in providing guidance in ECN injector modelling and also his kind help in reviewing the paper. I also express my sincere gratitude to Cédric Gazoppi for his always kindness, rapidness and patience in helping resolve the Linux problems I have encountered during these years.

Thirdly, I would like to thank Prof. Xiangyu Hu for accepting me to visit their lab (Chair of Aerodynamics and Fluid mechanics) at Technische Universität München (TUM). Many practical advices have been gleaned from Dr. Xiangyu Hu, Jianhang Wang and Dr. Shucheng Pan in improving the computational efficiency of UV flash.

Then, I would like to thank Prof. Manolis Gavaises for his valuable guidance in every IPPAD progress meeting and Nikolaos Chatziarsenis, Amalia Petrova for their timely organizing every IPPAD meeting, as well as arranging many meaningful trainings and seminars which have enriched our Ph.D life significantly. I would also like to thank the other 13 ESRs for sharing the happy moments and interesting discussions together during each meeting which will become valuable memories in my mind.

Last but not least, I would like to thank Dr. Qiu Lu for providing technical guidance during developing phase equilibrium model and Dr. Daniel Duke for sharing the experimental data for cavitation simulation.

Finally, I would like to give particular thanks to my families in China and EECP. The Ph.D will never be achieved if without their continuous encouragement and support.

Contents

List of Publications

- Journals

1. Yi P., Yang S., Habchi C., et al., A multicomponent real-fluid fully compressible four-equation model for two-phase flow with phase change [J]. Physics of Fluids, 2019, 31(2): 026102. (Featured article)
2. Yang S., Yi P., Habchi C., Real-fluid injection modelling and LES simulation of the ECN Spray A injectorusing a fully compressible two-phase flow approach, International Journal of Multiphase flow, 2019 (Under review)
3. Yang S., Habchi C.,et al., Cavitation modelling with real fluid equation of state considering dissolved gas. A&S, 2019 (Under review)

- Conferences

4. Yang S., Habchi C., and Lugo R., Subcritical and supercritical flow modeling using real-fluid Equation of State. A basic study of contact interface transport. IICR Workshop, Chania, Greece, DOI=10.13140/RG.2.2.34176.33289.
5. Yang S., Habchi C., Yi P, et al., Towards a multicomponent real-fluid fully compressible two-phase flow model[C]. ICLASS, 2018.
6. Yang S, Habchi C., Yi P., et al., Cavitation Modelling Using Real-Fluid Equation of State[C]//Proceedings of the 10th International Symposium on Cavitation (CAV2018). ASME Press, 2018.
7. Yi P, Jafari S, Yang S, Habchi C, et al. Numerical analysis of subcritical evaporation and transcritical mixing of droplet using a tabulated multicomponent vapor-liquid equilibrium model [C]. ILASS, 2019
8. Wang J, Yang S., Habchi C., et al., A multi-component real-fluid two-phase flow solver with high-order finite-difference schemes [C]. ILASS, 2019
9. Yang S., Habchi C. A Gibbs-Equilibrium Real-fluid Model (GERM2) for most of the thermodynamic conditions - Applications to the 3D simulation of cavitation and transcritical injection, SAE Congress, 2020 (Abstract submitted).

1 Preface

1.1 Introduction

The demand for higher efficiency and less emissions performance of internal combustion engines (ICE) has resulted in increasing effort regarding the injection system and mixture preparation. It is well-known that high injection pressure and decreasing nozzle diameter can improve the mixing of fuel with air and combustion in ICE. However, physical properties are changing significantly as pressure and temperature increase and the state of fluids deviates from ideal gas [1]. In subcritical conditions, due to a significant fuel surface tension, the formed non-continuous interface between the liquid and the gas results in primary atomization in which obvious droplets are formed [2]. However, as the pressure increases, the situation becomes quite different. The effects of surface tension diminish which restricts the formation of droplets and promotes diffusion dominated mixing processes [3]. Actually, as pressure approaches to the mixture critical point, which is a thermodynamic singularity, the mixture properties can exhibit liquid-like densities, gas-like diffusivities, and pressure-dependent solubility [4]. In addition, the surface tension and latent heat of the liquid become negligible [5]. As shown in earlier research about single component jet in liquid rocket engine [5], [6] with the increase of injection pressure, the spray undergoes a drastic change from two-phase break-up phenomenon to continuous diffusive mixing process which corresponds to the transition from the subcritical regime to the supercritical regime (see Figure 1.1 and ref. [7]).

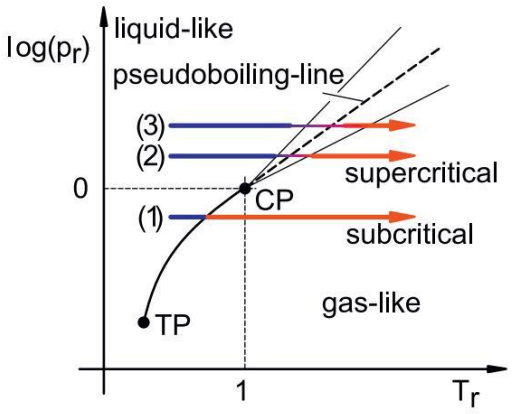

P_r: reduced pressure $P_r = \frac{P}{P_c}$; T_r: reduced temperature $T_r = \frac{T}{T_c}$

Figure 1.1 Diagram of the supercritical state space (applied to single component) and comparison of subcritical (1) and supercritical isobaric processes (2) and (3) [7].

Similar transition appears in multicomponent jet, as illustrated in the recent experimental results concerning the diesel injection at high pressure and temperature condition [8]. However, the transition criterion from subcritical to diffusive mixing regime is not rigorously following the variation of the pure fuel critical point. As found by Crua et al. [8], this transition is based on the value of $T_r\sqrt{P_r}$ of the fuel (see Figure 1.2). They have shown that the time taken by a droplet to transit to diffusive mixing depends on the pressure and temperature of the gas surrounding the droplet as well as the liquid fuel properties, such as liquid viscosity and volatility. Two-phase classical evaporation has been confirmed as a significant feature of diesel spray mixing, even at ambient gas conditions nominally above the pure fuel's critical point. As a matter of fact, from the thermodynamics point of view (without considering any flow or turbulent eddies), the transition from subcritical regime to supercritical regime should happen at the local mixture critical point, which are determined by the local mixture composition. However, Vapor-Liquid-equilibrium (VLE) analysis does not include the information related to surface tension. The interface thickness has been shown to increase sharply with the ambient temperature. Indeed, Dahms et al. [3] used

a real-fluid model combined with linear gradient theory to quantify the transition from non-continuous two-phase flow evaporation to continuous gas-liquid diffusion layer. As revealed in their study, the gas-liquid interfacial diffusion layers develop not only because of the vanishing surface tension forces, but also because of the reduction of mean free molecular path (λ) and broadening interfaces thickness (ℓ). This also characterises the decreasing of Knudsen number ($Kn = \frac{\lambda}{\ell}$) . Therefore, the interface thickness plays a key role in multicomponent transition between classical (subcritical) evaporation and single phase diffusive mixing process. However, as stated in their work [3], the primary breakup and evaporation are not the dominant process that affect the air-fuel mixing process when Knudsen number is smaller than 0.1. Instead, it is the diffusion process that has the strongest impact and controls the air-fuel mixing.

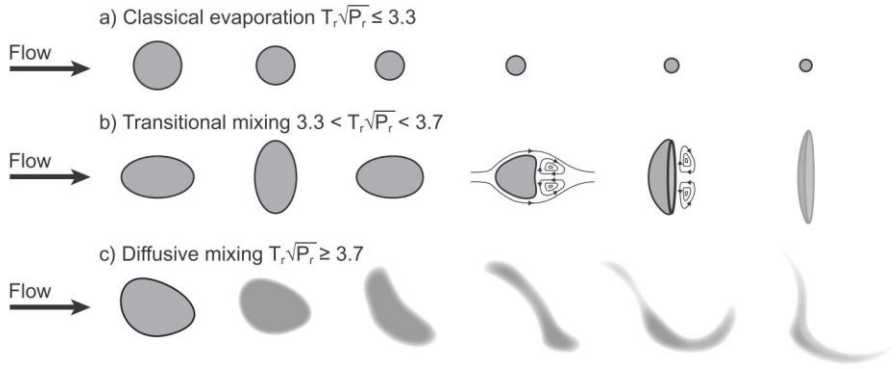

Figure 1.2 Evolution of individual n-dodecane droplets into gas at different ambient pressure and temperature. Each image represents the moving droplet. The figures in brackets indicate the reduced temperatures (Tr) and pressures (Pr) [8].

The above recent experimental results and thermodynamic analysis have stimulated great interest in exploring the multicomponent real fluid transition process. Up to now, most research involving this supercritical or transcritical conditions are focused on the liquid fuel injection in rocket engines [1], [4], [9], [10]. Numerical studies about the transcritical injection in diesel engine are very limited. Moreover, there are very few

computational fluid dynamics (CFD) codes able to simulate correctly a mixing regime starting from a subcritical fuel temperature condition towards a supercritical mixture in the combustion chamber. Indeed, most of them are not considering phase change or phase splitting, and then the possibility of interface existence or creation, respectively. In fact, most of the existing models can simulate either single or two-phase flow in subcritical conditions [11] [12] , or supercritical conditions [10], [13]–[15] lacking a comprehensive model which can deal with both simultaneously. Thereby, the current Ph.D study is aimed at developing a solver which is capable of modelling fuel injection in ICE with the consideration of subcritical, transcritical and supercritical regimes.

This thesis is part of the IPPAD project [16] entitled “Effect of 4500bar injection pressure and supercritical phase change of surrogate and real-world fuels enriched with additives and powering Diesel engines, on soot emissions reduction”, which is funded by the EU-H2020 programme. Simulation tools, to be developed in this Ph.D program include cavitation modelling, coupling the in-nozzle flow with the macroscopic fuel jet development and mixing in diesel-like engine conditions. Appropriate equation of states (EOS) for the highly non-ideal properties of fuels, at elevated pressures and temperatures, will be implemented in a comprehensive two-fluid modelling approach. Fuel injection in ICE at supercritical conditions will be addressed in order to study the transition to the diffusive mixing regime similarly to the experimental work from Crua et al. [8]. The developed simulation tools, currently missing from the literature and from commercial software, will be validated using experimental data bases acquired from the Engine Combustion Network (ECN), in which IFPEN is strongly involved. This thesis concerns an IFPEN scientific challenge V6: "Modelling of coupled phenomena" and will particularly focus on ICE simulation tools improvement. The detailed processes of cavitating in-nozzle flow, fuel injection and mixing, under subcritical and supercritical conditions will be thermodynamically

improved using real-fluid equation of states, and experimentally as well as basically validated.

1.2 Bibliographic Study

1.2.1 Diesel Injection modelling

I. Main concerns in diesel injection modeling

Driven by the target of optimizing combustion and reducing emissions, the research about ICE has been prevalent for several decades. Along with the rapid development of high-performance computing, Computational Fluid Dynamics (CFD) becomes more and more helpful in understanding Internal Combustion Engines (ICE). In particular, the modelling of injector can help to predict the liquid and vapor fuel distributions, soot precursor formation and the effect of cavitation on sprays and erosion damage [48]. To be more specific, cavitation phenomenon appears frequently in the upstream of the spray inside the nozzle especially in high injection pressure conditions. The mechanism of cavitation is attributed to rapid pressure drop, especially starting from location with geometrical changes like the holes entrance. However, except the erosion damage that cavitation may bring in, cavitation can improve downstream liquid atomization and evaporation process through higher spray angles, thus inducing better air-fuel mixing and optimizing auto-ignition and combustion processes, accordingly. Up to now, many researchers [12], [17]–[25] have adopted various numerical modeling and experimental strategies to understand the cavitation phenomenon and the effect on spray and combustion. This is reason why a comprehensive understanding of spray characteristics is required [23]. The spray is strongly influenced by the fuel physical properties and ambient conditions [24], [25]. At cold conditions, the spray is prone to be modelled as non-evaporating jet. The main physics involves primary atomization and gas entrainment; but also the secondary breakup, droplet drag and coalescence, etc. However, as the pressure and temperature

increase, more complex physical phenomena like evaporation becomes important for the spray mixing modelling, and whether this process will continue to exist under very high pressure and temperature is not clarified yet. This is the reason why the investigations about the high pressure and temperature conditions have witnessed a surge in recent years. Current thesis is also focusing on this domain. Other intriguing points about diesel injection modelling like combustion and soot emissions are not investigated in this thesis.

II. Current models for diesel injection modeling

As for spray modelling, the involved models generally can be divided into Eulerian or Lagrangian two types. Usually, the liquid is simulated as droplets in a Lagrangian way and gas is solved on the Eulerian mesh [26]. It is well-known that there exists a very dense spray zone close to the nozzle exit in which much refined mesh resolution is required to resolve the flow correctly. Because of the existence of intact liquid core in the dense spray zone, the Lagragian model is not appropriate any more. Thereby, it is reasonable to switch to the Eulerian model when modelling this zone. But in the downstream of the spray, the two-phase fluid becomes much dilute, which qualifies the use of the Lagrangian model (Figure 1.3). This is where the Eulerian-Lagrangian Spray and Atomization (ELSA) modelling idea comes from [27]. Lebas et al. [28] proposed an Eulerian single phase approach, combined with a vaporization model of Lagrangian tracked droplets to model diesel sprays more precise. In the dense zone close to the nozzle, Eulerian model is applied and switch to Lagrangian model once the liquid volume fraction reaches a critical value.

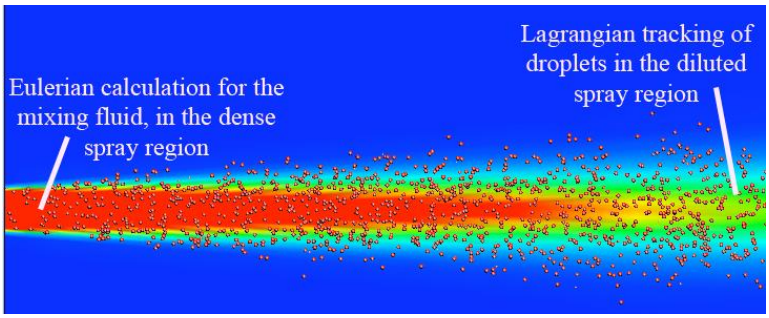

Figure 1.3 Euler/Lagrange transition - dense spray region in red colour [28].

However, in this kind of modelling , there are still some challenges to be addressed [26]. The first problem is the extremely large spatial gradient from the injector to chamber which makes the continuous modelling from the in-nozzle cavitating flow to external spray become much more difficult. Because of this, the early research were prone to employ phenomenological models to capture some of the relevant physics occurring during injection process like cavitation model, atomization models, droplet drag model, etc. In addition, a series of parameters like spray angle, the droplet velocity or the flow velocity, etc have to be prescribed before the simulation start. More recently, Kuensberg Sarre et al. [29] developed a nozzle flow model which takes into account the nozzle geometry, cavitation and injection pressure. Then the obtained flow information from internal flow are prescribed to the multidimensional Lagrangian spray modelling.

The models employed for the injector simulations have presented a wide variety based on the physics involved. For example, the main physics inside the nozzle is cavitation. Based on the distinction of dealing with interface, they are comprised of sharp interface models and diffused interface ones [21]. As for the sharp interface models, the general strategy is to locate the position of interface and the involved models are interface tracking, VOF and Level-Set, etc. The other alternative is not tracking the interface position and this corresponds to the so-called diffused interface models. In this case, the fluid is considered as continuum flow with a numerically diffused interface. The models are composed of single fluid model (i.e. homogeneous mixing

model) and two fluid models [21]. For the single fluid model, liquid and gas flow are assumed as mixing homogeneously and own the same velocity, pressure and temperature. Thus, only one continuity equation, energy equation and momentum equation are resolved for the whole system. In addition, this model can be combined with different phase change sub-grid models. For example, the homogeneous relaxation model employs a finite relaxation rate to control the phase change process to progressively reach the equilibrium state [30], [31]. On the other hand, homogeneous equilibrium model is assuming the equilibrium state reached instantly [32]. In contrast, the two fluid model needs to resolve the liquid and gas flow equations system separately and simultaneously. The mass transfer between the liquid and gas phase are computed by additional phase change models. Compared with single fluid model, two fluid model is expected to provide more accurate information like different phase temperature, pressure or velocity, but more costly. Relevant studies about two fluids model in dealing with cavitation can be found in refs. [19], [33], [34].

Nowadays, as aforementioned, the rapid development of computer performance has paved a way for researchers to turn to fully coupled Eulerian methods to be capable of realizing the whole injection simulation process. For example, Xue et al. [35] implemented a coupled approach to integrate the internal nozzle flow with the downstream spray under the Eulerian framework. Eulerian diffused interface approach is adopted to describe the near nozzle sprays. The obtained near nozzle mass density distribution at ECN spray A non-evaporating condition can correlate well with X-ray experimental data. The study also proves the Eulerian model can predict better physics in the near nozzle region than Lagrangian model. Similar researches can be found in refs. [36], [37].

Another reason that makes Eulerian based model prevalent is the demand for accurately simulating supercritical and transcritical injection. As noted in the introduction, the spray is mostly dominated by evaporation and diffusion mixing

process instead of the interphase transport rate of mass and energy at droplet surfaces at high pressure and temperature conditions [38]. The local transport timescales are smaller than mixing timescale which qualifies the phase equilibrium assumption for liquid droplet [38]. Thereby, the omission of the non-equilibrium droplet breakup process, collision modelling is possible, particularly when the fuel is injected at high ambient density (>15 kg/m^3) [39]. The injection modelling in high pressure and temperature is also the target in current thesis. Therefore, a detailed bibliographic study about supercritical injection is described in the following paragraph.

1.2.2 Supercritical, transcritical injection modeling

During injection, the jet physical phenomenon may experience drastic variations with increasing operating pressure and temperature. Based on the operating conditions, the jet thermodynamics regimes can be categorized into subcritical and supercritical. The jet in the chamber at subcritical conditions is dominated by atomization with clear droplets and ligaments forming from the liquid core (see Figure 1.4) [40]. As stated before, many researchers have contributed to better understand the mechanism of atomization [2], [21], [28]. In contrast, there are much less investigations about supercritical injection in diesel engine. But abundant previous studies about supercritical injection modeling are focused on liquid rocket engines (LRE) domain [4], [41], [42]. High pressure and high temperature can have significant impact on thermal properties of fuel. The jet characteristics at supercritical injection have been demonstrated by a series of experiments as in [40], [43]. All these previous information can enlighten us to better understand the supercritical regime in diesel engine and to improve current supercritical/transcritical injection modeling. Nevertheless, most of the models for the supercritical regime are limited to the single component dense fluids or multi-component diffusive mixing without considering phase transition. For example, Müller et al. [13] has used LES method based on different SGS models to compute the pure nitrogen injection in supercritical and

transcritical conditions. An interesting conclusion from their research is that the SGS model has minor effect on the mean density evolution and it is the eddies formed from large-scale Kelvin-Helmholtz instability that affect the most of the jet mixing. Banuti [7] has recently used molecular dynamics simulations and fluid reference data to reveal some non-linearity of physical properties for pure component at supercritical conditions (Figure 1.5). Particularly, they confirmed that there exists a widow line which corresponds to a pseudo-boiling curve in supercritical zone (Figure 1.1). This line divides fluid into gas-like and liquid-like in supercritical condition, as shown in Figure 1.1. Heat capacity and density go through a peak when crossing the widow line (Figure 1.1). Besides, as discussed in the introduction Section, Dahms et al. [3] also have proved the transition from liquid to gaseous states is indeed much smoother for transcritical conditions than in subcritical conditions. They have developed a real fluid model using the Benedict–Webb–Rubin (BWR) equation of state and Linear Gradient Theory to compute and analyse the vapor-liquid interfacial structure. In their research, the conventional understanding about disappearance of surface tension leading to the diffusion dominated mixing in supercritical condition has been questioned. Instead, the analysis shows that surface tension does not vanish instantly. Rather, the interface thickens at time beyond the equilibrium solution, favoring the reduction in intermolecular forces, i.e., surface tension. In addition, the gas-liquid interfacial diffusion layers develop not only because of the vanishing surface tension forces, but also because of the reduction of mean free molecular path (λ) and broadening interfaces thickness (ℓ). This also characterises the decreasing of Knudsen number ($Kn = \frac{\lambda}{\ell}$) in the same time as the surface tension. This research work has concluded that the flow is a two-phase non-continuum flow when the Knudsen-number is less than 0.1. Otherwise, a single phase dense fluid should be considered as the right model. Therefore, improving our understanding of fuel atomization and mixing processes at the microscopic scale is essential for the development of physically-correct models and the validation of numerical simulations.

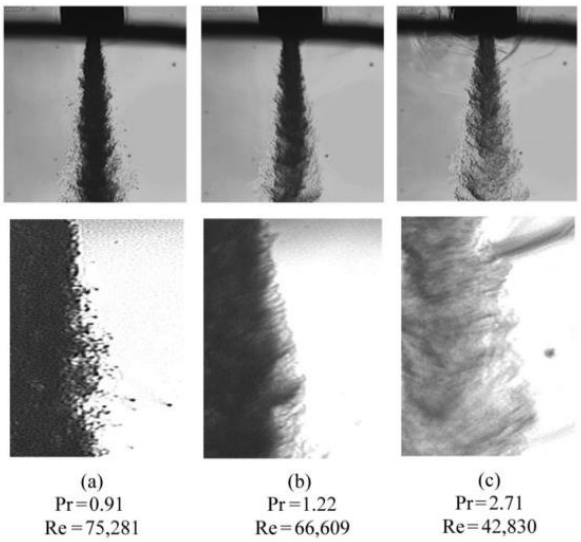

Figure 1.4 Injection of liquid N_2 from subcritical to supercritical pressure condition [40].

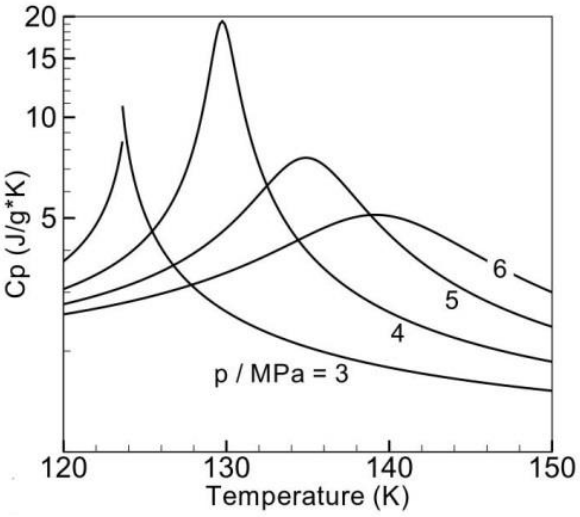

Figure 1.5 Specific isobaric heat capacity Cp of N_2 at sub- and supercritical pressures [7].

As a matter of fact, in real diesel engine injection system, the problem is even more complex. This complexity is explained by two issues. Firstly, single component system is not the main concern anymore. Instead, the injection process involves many components. In this case, the mixture critical point which depends on the mixture composition, has to be considered instead of the pure fuels' critical point (CP). As

seen in Figure 1.7, the critical temperature has not varied abruptly as the concentration of nitrogen in the mixture is less than 0.8. In contrast, critical pressure of the mixture has changed significantly with the variation of molar fraction of nitrogen. The abrupt change of mixture critical point has made the transcritical injection modeling become more complex. Taking ECN spray A [44] as an example, the liquid n-dodecane at 363K is injected into combustion chamber filled with nitrogen at its supercritical conditions (900K, 60 bar). The pressure and temperature (60bar, 900K) inside the chamber is above the fuel critical point (18.2bar, 658K). In the injection process, based on liquid position, the flow has presented different regimes. Figure 1.6 is the T-x diagram of n-$C_{12}H_{26}$ and N_2 system at pressure of 60 bar which corresponds to the chamber condition in ECN Spray A. In this figure, point (a) and point(c) are situated at single phase state, in which point(a) represents the fluid inside the liquid core which usually stays at low temperature and higher pressure with respect to the critical pressure of fuel. Point (b) represents the two-phase state of the fluid which is mixed with nitrogen. The two-phase state starts with the molar fraction of N_2 at 0.074. As the molar fraction of nitrogen mixed in the fluid is more than 0.5 (Figure 1.7), the mixture critical pressure will soar to hundreds of bars which far exceeds the chamber pressure (60bar). In this situation, the flow is mostly situated at two-phase zone with respect to the ambient pressure 60bar. The conventional phase change like evaporation will surely appear. However, as the molar fraction of N_2 is above ~0.9, the critical pressure of the mixture is much closer to N_2 (33.7bar) and lower than chamber pressure. Under this condition, the temperature of the mixing layer is also approximated to the chamber value (900K), much higher than mixture critical temperature. The flow will present the characteristics of supercritical fluid corresponding to point (c) in Figure 1.6. Phase change is impossible in this situation and the flow is more prone to gas dynamics. This state also corresponds to the mixing layer outside the liquid core. The mixing of nitrogen is not completed instantly which implies the fluid has been through complex regimes variations from initial Point (a) to

Point (c). If the chamber pressure is greater than the mixture critical pressure maximum value inside the whole computational domain, the jet is evolving in a diffusive mixing supercritical regime. Otherwise, interfaces (even significantly thickened) will exist at some locations (cells) where the local mixture critical pressure is higher than the combustion chamber pressure. In this case, one cannot know from a priori-analysis where the flow will be subcritical or supercritical. Thereby, the overall injection process may contain both the subcritical and supercritical regimes. This implies there exists possibility that phase transition phenomenon may occur during the mixing procedure. Actually, Poursadegh et al. [45] recently has investigated the criterion for the jet to bypass the subcritical phase change zone to diffusion mixing regime. Their research has redefined the critical value of Knudsen number for the controlling of fluid transition. As concluded in their study, the two-phase zone or conventional evaporating jet is still the dominant physics in diesel injection. This can also be confirmed by the phase diagram in Figure 1.6 for the Spray A conditions, for instance. The fluid has been through a large vapor-liquid coexistent zone compared with much smaller single phase zone. Moreover, this specific process has been confirmed by recent experimental research by Crua et al. [8]. They have proved that two-phase classical evaporation exists as a significant feature of diesel spray mixing, even at ambient gas conditions nominally above the fuel's critical point. Another interesting point is the mostly coinciding of the 'Frozen Adiabatic Mixing Temperature' with 'True Adiabatic Mixing Temperature' presented at Figure 1.6. The deviation between them only appears at the range of 0.5-0.9 with respect to the molar fraction of N_2. This seems to explain well the good correlation of Spray A modeling results with experimental data even using only the mixing regime without considering phase change process [15]. Up to now, most models used for transcritical modeling have only taken into account the mixing of the fuel and gas and neglected the complex phase transition phenomenon[13]–[15], [46]. The omitting of phase transition implies neglecting the possible evaporation or condensation at interfaces.

Qiu and Reitz [47] have used the phase equilibrium model to investigate the occurrence of condensation in supercritical conditions.

In addition, the non-ideality of physical properties in supercritical or transcritical regime makes the selection of a real fluid equation of state essential. Considering the good compromise between computation efficiency and accuracy, Peng-Robinson EoS has been selected by some researchers for the transcritical injection modeling [32], [47], [48]. However, it is well-known that PR EoS has some disadvantages in predicting the liquid density and derivative property such as speed of sound speed at high pressure. There are some researchers [49] who have used PC-SAFT EoS to simulate the supercritical and transcritical real-fluid mixing process without considering phase transition. To accurately capture the phase transition phenomenon in transcritical injection process, most researchers have chosen phase equilibrium model [32], [38], [47]. The phase equilibrium method in the multiphase flow is based on the assumption that the characteristic time of reaching equilibrium is much smaller than the flow timescale which corresponds to the transient stiff relaxation method used in recent multiphase flow research [33], [50]. In addition, the multiphase flow models adopted for the transcritical modeling are dominated by the fully conservative 4-equation model [32], [51]. It is well known that one of the notorious characteristics about the fully conservative equation is the serious spurious oscillations appearing in the contact discontinuity [51]. This spurious oscillations become even more serious when involving non-linear equation of state like PR EoS. Ma et al. [51] have proposed the double flux model based on the stable entropy method aimed at damping the pressure oscillations appearing in the transcritical modeling. Matheis and Hickel [32] have utilized both the fully conservative Navier-Stokes equation and quasi-conserved energy equation to model the transcritical injection in ECN spray A condition, in which, however, the quasi-conservative model has presented uncontrolled error in temperature due to the pressure based non-conservative energy equation, especially when using relatively rough meshes. Other similar strategy like introducing of

artificial mass diffusivity to the continuity and momentum equations by Kawai et al. [52] can also help eliminating the spurious oscillations in the velocity field.

All of the previous researches have provided valuable insight into current work. But the comprehension of transcritical regime is still not sufficient with its intricacies involving turbulent mixing, non-ideal thermodynamics and transport anomalies [4]. Up to now, there are very few CFD codes able to simulate correctly transcritical conditions starting from a subcritical fuel temperature condition towards a supercritical mixture in the combustion chamber. Indeed, as mentioned before, most of the existing models can simulate either single or two-phase flow in subcritical conditions, or purely supercritical mixing without considering phase transition, lacking a comprehensive model which can deal with transcritical conditions including possible phase transition (including nucleation of bubbles and droplets and their evaporation and condensation). This thesis aims at dealing with this challenge.

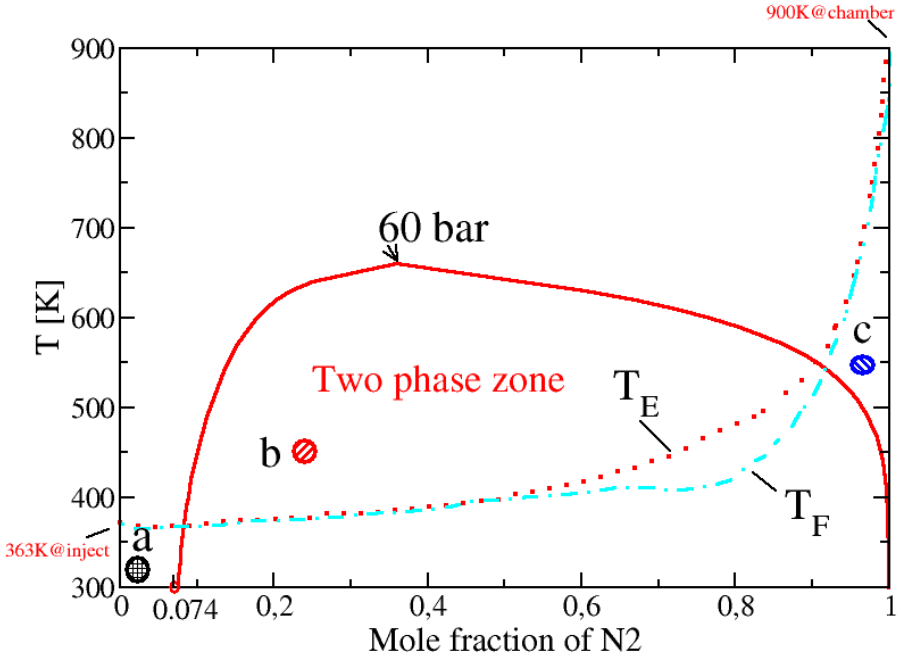

Figure 1.6 T-x phase diagram of n-$C_{12}H_{26}$ and N_2 at spray A condition. T_E illustrates the True Adiabatic Mixing Temperature considering phase stability. T_F denotes Frozen Adiabatic Mixing Temperature without considering phase change. Point (a) represents the liquid core zone in which the temperature is around 363K. Point (b) is located between the liquid core and chamber gas and part of chamber gas has entrained in the liquid fuel. Point (c) represents the exterior layer of spray where flow is dominated by high temperature gas.

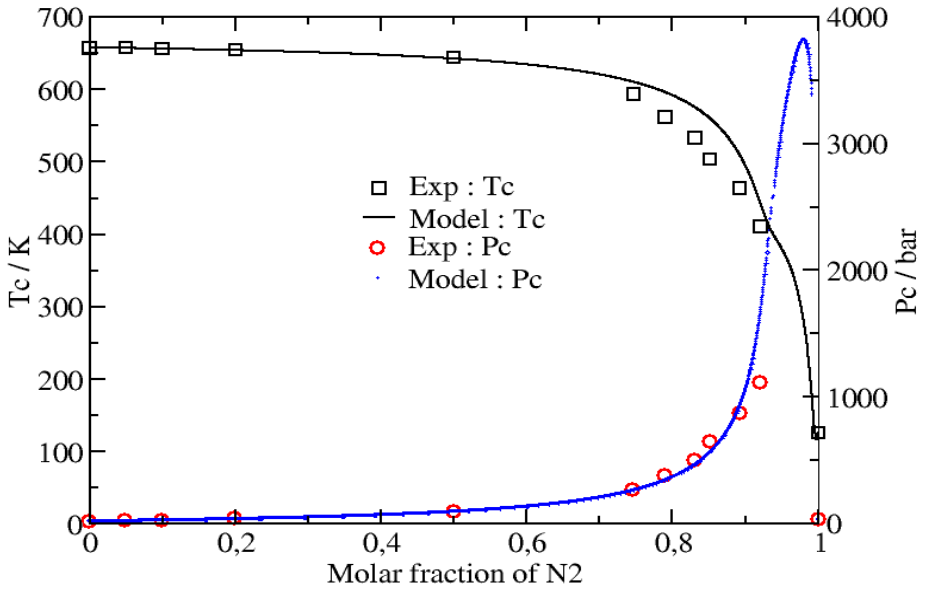

Figure 1.7 Comparison of mixture critical point (Tc, Pc) (n-$C_{12}H_{26}$-N_2) computed by commercial software Simulis [53] based on Peng-Robinson EoS with experimental data.

1.3 State of art about this thesis

The research here has been based on a fully compressible two fluid 7-Equation model, initiated by Baer and Nunziato [54] and developed for two-phase problems by Saurel and Abgrall [50]. This model has resolved liquid phase and gas phase separately which enables the determination of thermodynamic and kinematic variables of each phase. Moreover, it can be combined with complex equations of state and is able to deal with multicomponent problems. In ref. [50], the reliability of this model in solving interface and strong shock waves has been proved. The other important advantage of two fluid model lies in its ability in solving contact discontinuity problem appeared in the interface, which has been proved in ref. [54]. Wang [19] has extended this 7-Equation flow solver to 8-equation flow model combined a with phase equilibrium model. This model is able to deal with multi-component flows with phase change. But the phase change of non-condensable gas is eliminated in Wang's model. Currently, the a 7-Equation model has been implemented in the in-house code IFP-C3D [55]. Habchi et al. [33] has implemented a Gibbs Energy Relaxation Model

(GERM) to be capable of dealing with phase change under subcritical condition. Based on GERM, Bejoy [2] developed the two-phase surface density model to make the modeling of atomization process possible. Overall, the solver is able to simulate full jet including the cavitation, atomization, evaporation, etc. Due to the equation of state used in the original solver is Stiffened Gas EoS in liquid phase and ideal Gas EoS for gas phase, the modeling of high temperature, pressure jet are strongly restricted. Thereby, the thesis is aimed to solve this problem. In current research, a multi-component phase equilibrium solver combined with Peng Robinson EoS was developed and coupled with a 6-Equation as well as a reduced 4-Equation quasi-conservative flow system. This solver shall be able to model the subcritical, supercritical as well as transcritical regimes with the consideration of phase transition (i.e. nucleation and condensation process, etc) simultaneously.

1.4 Objective and thesis Organization

The main objective of this study is to develop a fully compressible two-phase flow model using real-fluid EoS based on thermodynamics equilibrium theory. Particularly, the target was to extend the in-house code (IFP-C3D), which already includes a 7-Equation model [33] that can model cavitating in-nozzle flow and primary atomization in subcritical conditions, to supercritical and transcritical conditions applicable for multicomponent flow with real-fluid EoS.

This manuscript has been organized as follows: The developing of the thermodynamic solver is described in Section 2. Section 3 introduces the original 7-Equation model, the updated 6-Equation systems as well as more reduced 4-Equation system. The detailled procedures related to the implementation of thermal solver into flow solver are illustrated. A series of 1D academic test cases based on the developed 4-Equation and 6-Equation systems including advection tube, shock tube and expansition tube are performed and reported in Section 4. Section 5 presents the 2D/3D cavitation modeling in a real-size nozzle with 6-Equation and 4-Equation systems. The 3D modelling results are compared to X-ray experimental data and the effect of dissolved N_2 on cavitation inception and development, as well as the nucleation process are discussed. Section 6 presents the results of 4-Equation system in simulating the diesel injection process with transcritical conditions at low injection pressure and high injection pressure conditions, respectively. The results of high injection pressure scenario corresponds to the ECN Spray A modelling and the comparisons with experimental data are also presented. Then the summary of the thesis, conclusion and future work are presented in Section 7.

2 Developing of Phase Equilibrium Solver

The main thermodynamic ingredients used in this work are gathered below from a few references in the literature. The most important details are discussed in order to be able to properly implement them in a new thermodynamic solver which will be coupled with the flow solvers described in Chapter 4 and 5.

2.1 Equation of State and thermodynamics properties

As mentioned above, ideal gas equation of state cannot predict the thermal non-idealities behaviors accurately in high temperature and pressure condition, as shown in Figure 1.5. Considering the good compromise between computational efficiency and accuracy, the real fluid Peng Robinson EoS (Equation (2.1) has been selected as the thermal closure term of transport equation system as detailed in Chapter 4 and 5. Since the thesis is aimed to solve the multi-component system, van der Waals mixing rule (Equation (2.2)) is adopted for the computation of mixture thermal properties. The equation of state is defined as:

$$P = \frac{RT}{v-b} - \frac{a(T)}{v(v+b)+b(v-b)} \tag{2.1}$$

Where, $a(T) = 0.45724\frac{R^2{T_c}^2}{P_c}\alpha(T)$, $b = 0.07780\frac{RT_c}{P_c}$, $\alpha(T) = (1+m(1-\sqrt{T_r})^2$

$$m = 0.37464 + 1.5422\omega - 0.26992\omega^2$$

The equation of state relates the pressure P to the temperature T and the molar volume v. R denotes ideal gas constant. P_c and T_c are the component critical points and ω is the acentric factor. These properties have been available for each compound. For the mixture, the one fluid model is used and van der Waals mixture rules are used as follows,

$$\mathrm{a} = \sum\sum x_i \cdot x_j \cdot a_{ij}$$

$$a_{ij} = \sqrt{a_i a_j}\left(1 - k_{ij}\right) \tag{2.2}$$

$$b = \sum x_i \cdot b_i$$

Where x_i is the molar fraction for component i. k_{ij} is binary interaction parameter that can be fitted on available experimental data in order to well represent the phase diagram of the binary system.

The compressibility factor is defined according to

$$Z = \frac{Pv}{RT} \tag{2.3}$$

In which v is the specific molar volume.

With Peng Robinson (PR) EoS, the compressibility factor can be calculated by

$$Z^3 - (1 - B)Z^2 + (A - 3B^2 - 2B)Z - (AB - B^2 - B^3) = 0 \tag{2.4}$$

With

$$A = \frac{aP}{R^2T^2}, \qquad B = \frac{bP}{RT}$$

If the temperature and the pressure are known, the cubic equation should be solved and will give one or three real roots. In the latter case, the smaller root corresponds to a liquid phase, the greater to the vapor one and the intermediate root has no physical meaning.

A main thermodynamic property for liquid-vapor modelling is the fugacity and fugacity coefficient of the Peng and Robinson EoS is computed by:

$$ln(\varphi_i) = \frac{b_i}{b}(Z - 1) - \log(Z - B) \tag{2.5}$$

$$+ \frac{A}{2\sqrt{2}B}\left[\frac{b_i}{b} - \frac{2\sum_j x_j a_{ij}}{a}\right] ln\left[\frac{Z + \left(1 + \sqrt{2}\right)B}{Z + \left(1 - \sqrt{2}\right)B}\right]$$

Where x_j is phase composition for different component.

With fugacity coefficient, fugacity can be written as

$$fugacity_i = \varphi_i x_i P \tag{2.6}$$

Fugacity are involved in the calculation of the chemical potentials of each species and phase equilibria are expressed on the basis of the equality of the chemical potentials of each species between the phases present.

Another important property is the molar internal energy which is computed from the sum of the residual part $u_d$and an ideal gas part u_0 [56]. The ideal gas state is calculated with specific polynomial equation (see [57]) and the residual term is deduced from equation of state using its definition,

$$u_d = u - u_0 = \int_{\infty}^{v} \left[T\left(\frac{\partial P}{\partial T}\right) - P \right] dv \tag{2.7}$$

By using PR EoS, u_{d} can be written as,

$$u_d = \frac{T\frac{da}{dT} - a}{2\sqrt{2}b} ln\left[\frac{v + \left(1+\sqrt{2}\right)b}{v + \left(1-\sqrt{2}\right)b}\right] \tag{2.8}$$

Similarly, molar enthalpy (h) can be calculated using its residual function (h_d) and the molar enthalpy of ideal gas h_0, written as:

$$h_d = h - h_0 = \int_{0}^{P} \left[v - T\left(\frac{\partial v}{\partial T}\right) \right] dP \tag{2.9}$$

In which h_d is computed from the equation of state:

$$\frac{h_d}{RT} = \frac{\frac{\partial a}{\partial T}\left(\frac{P}{TR^2}\right) - A}{2\sqrt{2}B} ln\left[\frac{Z + \left(1+\sqrt{2}\right)B}{Z + \left(1-\sqrt{2}\right)B}\right] + Z - 1 \tag{2.10}$$

The same as the computation of entropy, it can be formulated as,

$$S_d = S - S_0 = Rl\,n(Z) + \int_{\infty}^{v} \left[\left(\frac{\partial P}{\partial T}\right)_v - \frac{R}{v}\right] dv \tag{2.11}$$

With

$$\frac{S_d}{R} = \frac{\frac{\partial a}{\partial T}\left(\frac{P}{TR^2}\right)}{2\sqrt{2}B} ln\left[\frac{Z + \left(1+\sqrt{2}\right)B}{Z + \left(1-\sqrt{2}\right)B}\right] + ln(Z - B) \tag{2.12}$$

The computation of sound speed is formulated as according to ref. [58],

$$C_s = \sqrt{\left(\frac{\partial P}{\partial \rho}\right)_S} = \sqrt{\left(\frac{\partial P}{\partial \rho}\right)_T + \frac{T}{C_v \rho^2}\left(\frac{\partial P}{\partial T}\right)_\rho^2} \tag{2.13}$$

Constant volume heat capacity is computed with the numerical expression as,

$$C_v = \frac{u(T + \Delta T, v) - u(T, v)}{\Delta T} \tag{2.14}$$

In the simulation, ΔT is adopted with 10K for the sake of accuracy. The alternative method is to use the analytical expression to compute directly.

Then constant pressure heat capacity is easy to get by the relation with constant volume heat capacity, formulated as,

$$C_p = C_v + \frac{T}{\rho^2}\left(\frac{\partial P}{\partial T}\right)_\rho^2 \left(\frac{\partial P}{\partial \rho}\right)_T^{-1} \tag{2.15}$$

The isothermal compressibility β_T is used to compute the isothermal change of the specific volume with the pressure, defined as following [59].

$$\beta_T = -\frac{1}{v}\left(\frac{\partial v}{\partial P}\right)_T \tag{2.16}$$

The adiabatic compressibility β_s is an indication of the volume change as pressure changes at constant entropy and derived as,

$$\beta_s = -v\left(\frac{\partial P}{\partial v}\right)_s \tag{2.17}$$

The adiabatic bulk modulus, B_s, is the reciprocal of the adiabatic compressibility.

$$B_s = -v\left(\frac{\partial v}{\partial P}\right)_s \tag{2.18}$$

The aforementioned speed of sound C_s can also be reformulated with adiabatic bulk modulus by Equation (2.18) [59].

$$C_s = \sqrt{-v^2\left(\frac{\partial P}{\partial v}\right)_S} = \sqrt{vB_s} \tag{2.19}$$

2.2 Phase Equilibrium Theory

Based on the second law of thermodynamics, one isolated system owns the maximum entropy at the equilibrium state. As shown in Equation (2.21), the change of entropy for a multiphase system can be formulated according to internal energy Equation (2.20). From the mathematical point of view, the maximum value corresponds to the stationery point of the function. If applied to Equation (2.21), the extreme point

appears when $\mathrm{d}S = 0$. At equilibrium state, u_j, v_j, n_i are subject to constraints Equations (2.22). With u_j, v_j, n_i as independent variables, the Equation (2.21) can be written as Equation (2.23). To satisfy the equilibrium constraints, these terms $\left(\frac{1}{T_i} - \frac{1}{T_j}\right)$, $\left(\frac{P_i}{T_i} - \frac{P_j}{T_j}\right)$, $(\frac{\mu_k^i}{T_i} - \frac{\mu_k^j}{T_j})$ in Equation (2.23) should equal zero. The solution $(T_i = T_j, P_i = P_j, \mu_k^i = \mu_k^j)$ implies the temperature and the pressure must be uniform throughout the system and the chemical potentials of one component should be the same for each phase of the system at equilibrium. But the chemical potentials between individual component are not surely identical [60].

$$\mathrm{d}u = \mathrm{T}dS - \mathrm{P}\mathrm{d}v + \sum_k \mu_k \, dn_k \tag{2.20}$$

$$dS = \sum\nolimits_j^{N_p} \frac{\mathrm{d}u_j}{T_j} + \sum\nolimits_{i \neq j}^{N_p} \frac{P_j}{T_j} \mathrm{d}v_j - \sum\nolimits_{i \neq j}^{N_p} \sum_k^{N_c} \frac{\mu_k^j}{T_j} \mathrm{dn}_k^j \tag{2.21}$$

$$\sum\nolimits_j^{N_p} \mathrm{d}u_j = 0; \ \sum\nolimits_j^{N_p} \mathrm{d}v_j = 0; \ \sum\nolimits_j^{N_p} \mathrm{dn}_k^j = 0 \ , \mathrm{k} = 1 \ldots N_c \tag{2.22}$$

$$dS = \sum\nolimits_{i \neq j}^{N_p} (\frac{1}{T_i} - \frac{1}{T_j}) du_j + \sum\nolimits_{i \neq j}^{N_p} (\frac{P_i}{T_i} - \frac{P_j}{T_j}) dv_j + \sum\nolimits_{i \neq j}^{N_p} \sum_k^{N_c} (\frac{\mu_k^i}{T_i} - \frac{\mu_k^j}{T_j}) dn_k^j \tag{2.23}$$

where, i, j are phase index. N_p denotes the phase number. N_c, K are both component index.

Most of systems studied are at constant pressure and temperature. In this situation, for a spontaneous process, the change of Gibbs energy follows Equation (2.24).

$$\mathrm{dG} < \mathrm{T}\mathrm{d}S - \mathrm{P}\mathrm{d}v + \mathrm{d}(\mathrm{P}v) - \mathrm{d}(\mathrm{T}S) \tag{2.24}$$

With the constant pressure and temperature, this equation turns as,

$$\mathrm{dG} < 0 \tag{2.25}$$

This indicates phase equilibrium process proceeds as the direction of decreasing global Gibbs free energy. Thus, the final equilibrium state corresponds to the global minimum value for the Gibbs energy [60] corresponding to the maximum value of entropy. It is worth noting that Gibbs energy minimization is usually preferred to entropy maximization for an isothermal and isobaric system.

2.3 Vapor Liquid Equilibrium

The most frequently involved phase equilibrium problem is the vapor-liquid two-phase equilibrium (VLE) system which is also the main concern in current study. For more complex situations like Vapor-Liquid-Liquid multiphase equilibrium system are out of the domain for current thesis. Generally, a full vapor liquid equilibrium calculation includes two parts: (1) stability test and (2) isothermal-isobaric flash (TP flash) which may include a phase split (i.e. phase transition) calculation [60]. The aim of the stability test is to verify the stability of the system. If the result of stability test indicates the system as unstable, it implies an extra phase can be added (or subtracted) in order to stabilize the system. Otherwise, the so-called TP flash computation have to be performed to obtain the final phase composition. More theoretical descriptions are provided below.

2.3.1 Stability Test

Stability analysis is to test the stability of one closed system. Usually, the thermodynamics condition is at given temperature and pressure. The stability analysis needs to decide whether there exists a new phase which can decrease the original overall Gibbs free energy. The test starts by firstly assuming there exists a new phase. Then we compute the variation of Gibbs energy ΔG with respect to the initial value (Equation (2.26)). If $\Delta G > 0$, it implies the original system is stable and the new added phase can only enhance the overall Gibbs energy. Otherwise, a phase spilt can occur to decrease the overall Gibbs energy making the system become more stable.

$$\Delta G = \sum_i (\mu_i' - \mu_i)\delta n_i < 0 \tag{2.26}$$

Where, μ_i' , μ_i are the chemical potential of the new phase and original phase for each component respectively. δn_i is the molar number of each phase for different component.

One of the most mature and efficient method to resolve this problem is Tangent Plane Distance test (TPD test) initiated by Baker [61] and developed by Michelsen [62]. This model is according to Gibbs energy minimization method. It is well-known that the minimum point of Gibbs free energy corresponds to phase equilibrium state in the system. The relevant equation to be solved in TPD test is

$$\mathrm{F(y)} = \sum_{i}^{n_c} y_i(\mu_i(y_i) - \mu_i(z_i)) \tag{2.27}$$

Constrained by,

$$y_i > 0,\ \sum y_i = 1$$

Where, i is component index. n_c denotes the number of component. y_i, z_i is the molar fraction of trial phase and feed for each component respectively.

Geometrically, F(y) represents the vertical distance from the tangent hyperplane to the molar Gibbs energy surface at given feed composition z_i to the energy surface at composition y_i [62]. The stability requires $\mathrm{F(y)} \geq 0$ for any trial phase. Otherwise, if there exists some points that leads to $\mathrm{F(y)} < 0$, the original system is unstable and phase split (i.e. nucleation) can happen. Therefore, the final problem is transformed to locate the minimum point of objective function $\mathrm{F(y)}$. This corresponds to the stationary point of the function where the derivative of the variable equaling zero. When applied to an equation of state, the objective function F(y) can be written with fugacity coefficient as follows,

$$\mathrm{g(y)} = \sum_{i}^{n_c} y_i(ln(y_i) + ln(\varphi(y_i)) - \mathrm{h}_i) \tag{2.28}$$

$$\mathrm{h}_i = ln(z_i) - ln(\varphi(z_i))$$

In this equation, the phase molar fraction has to be positive, subject to the constraints shown as in Equation (2.29). To furtherly simplify the computation, Michelsen has formulated an unconstrained objective function based on new variable Y_i, defined as.

$$\mathrm{Y}_i = y_i \exp(-k) \tag{2.29}$$

$$y_i = \mathrm{Y}_i / \sum \mathrm{Y}_i$$

Where, k is a constant.

Correspondingly, the objective function transforms into:

$$g^*(Y_i) = 1 + \sum_i^{n_c} Y_i(ln(Y_i) + ln(\varphi(Y_i)) - h_i - 1) \tag{2.30}$$

In which $h_i = ln(z_i) - ln(\varphi(z_i))$

The new function (Equation (2.30)) is proven to own the same stationery point as Equation (2.28) [62]. The sign of function value at stationary point resembles before as well. Nevertheless, the second objective function is still recommended for its less constraints. To have a more efficient computation and avoid negative mole fractions during the iterations, Michelsen suggested to replace the iteration variable with $\alpha_i = 2\sqrt{Y_i}$. The first order derivative of objective function is

$$\frac{\partial g^*(Y_i)}{\partial \alpha_i} = \sqrt{Y_i}(ln(Y_i) + ln(\varphi(Y_i)) - h_i) \tag{2.31}$$

There are multiple ways to initialize the molar number Y_i. The conventional initializing method proposed by Michelsen [62] is by using equilibrium constant K_i to obtain an initial gas-like and liquid-like molar number formulated as Equation (2.32).

$$1)\ Y_i = K_i z_i;\ \ 2) Y_i = z_i/K_i \tag{2.32}$$

The method is able to ensure the searching space as big as enough. Nevertheless, sometimes it is still difficult to locate the stationary point or avoiding finding the trifle point. Li et al. [63] has furtherly extended this strategy by adding several other transformed equations formulated as Equation (2.33).

$$3)\ Y_i = \sqrt[3]{K_i z_i};\ \ 4)\ Y_i = \frac{1}{\sqrt[3]{z_i/K_i}};\ 5)\ Y_i = 0.9/z_i \tag{2.33}$$

For hydrocarbon systems at low pressure, equilibrium constant K_i can be well reasonably approximated by the Wilson equation,

$$K_i = \frac{P_{c_i}}{P}\exp(5.42\left(1 - \frac{T_{c_i}}{T}\right)) \tag{2.34}$$

Where P_{c_i}, T_{c_i} are critical pressure and temperature of each component.

To locate the stationary points of objective function, many algorithms are available. The most direct algorithm is Successive Substitution (SS) and Accelerated Successive Substitution (ASS). The direct substitution method has a liner convergence rate and can find the local minimum value rapidly in the case that the dependence of fugacity coefficient on phase composition is low. The accelerated algorithm recommended by Michelsen is General Dominant Eigenvalue Method [60], [64], [65] and Broydens method [66]. The second order Newton minimization strategy can be also an alternative for these problems. But to implement high order newton algorithm, a Hessian matrix become essential. To reduce the computation cost of Hessian matrix, some researchers [65], [67] have recommended the Quasi-Newton with Broyden-Fletcher-Golfarb-Shanno (BFGS) update to approximately replace inversed Hessian matrix. The BFGS update has the heredity of positive definiteness and can find the local extremes. However, the Quasi-Newton method usually needs to be combined with line search method to ensure the searching path is proper. As a trade-off between computation efficiency and accuracy, the present study has implemented Successive Substitution (SS) and BFGS methods. During computation, the Successive Substitution (SS) method is performed firstly. If no stationary points or trifle points are found, the computation will be switched to BFGS method. The implementation details of BFGS method can be found in ref. [68]. One point worth mentioning is that these methods have a strong dependency on initial values and belong to the local minimization method. Even local minimization methods normally converge to the global minimum of Gibbs free energy with good initialization, it still cannot always guarantee the convergence around critical point. Thereby, some researchers have turn to more complex and time-consuming global searching algorithm. For example, Nichita et al. [69] has adopted the tunneling method along with the reduced variable approach to solve the global stability problem. More bibliographical study about global stability test can be found in ref. [70]. Undoubtedly, global optimizing algorithm can provide more reliable results then local minimization.

Nevertheless, it still may not locate all the stationary points around the critical point zone and the computational cost is much higher than local searching method. Thereby, the study here is prone to choose a local minimization method with a sound initialization as a trade -off between accuracy and efficiency. Once the stationary points are found, the tangent plane distance or objective function are computed again to decide the stability state. If the tangent plane distance or objective function value are all positive at the stationery point, the system is proved at stable state. Otherwise, a new phase can be generated to reduce the global Gibbs free energy.

2.3.2 Phase Split Model

To obtain the real phase composition for an unstable system, phase split calculation is mandatory. Of course, the prerequisite is that stability test (TPD test) has already verified the system as unstable at given temperature and pressure. According to thermodynamics equilibrium theory, at constant temperature and pressure, the equilibrium state requires the chemical potential or the partial molar Gibbs free energy of liquid phase and vapor phase to be equal. When applied to equation of state, this can be transformed into the equaling of the fugacity as Equation (2.35):

$$f_i^l = f_i^v \tag{2.35}$$

$$\mathrm{x}_i \varphi_i^l \mathrm{P} = \mathrm{y}_i \varphi_i^v \mathrm{P} \tag{2.36}$$

$$K_i = \frac{y_i}{x_i} = \frac{\varphi_i^l}{\varphi_i^v} \tag{2.37}$$

Where, φ_i^l, φ_i^v are the fugacity coefficient for the liquid and vapor phase of each component respectively.

One key equation to be solved during phase split computation is the well-known Rachford-Rice equation (Equation (2.38)) or material balance equation. For a general liquid-vapor equilibrium system, this equation can be written as,

$$\sum_{i=1}^{N_c} \frac{z_i(\mathrm{K}_i - 1)}{1 + \psi_v(\mathrm{K}_i - 1)} = 0 \tag{2.38}$$

In which, z_i is mole number of component or feed. K_i is equilibrium constant. N_c denotes number of components and ψ_v is vapor molar fraction.

Phase composition y_i, x_i can be computed from Equation (2.38) with the relation $\sum_{i=1}^{N_c} y_i = 1$, $\sum_{i=1}^{N_c} x_i = 1$ and finally written as,

$$y_i = \frac{z_i \mathrm{K}_i}{1 + \psi_v(\mathrm{K}_i - 1)}$$
$$x_i = \frac{K_i}{1 + \psi_v(K_i - 1)} \tag{2.39}$$

To resolve Equation (2.38), a variety of algorithms are available in the literature. The classical algorithm is direct successive substitute (SS) method, which can be seen in refs. [65], [71]. In this algorithm, K_i is updated in outer loop by Equations (2.39) and (2.37). ψ_v is computed in inner-loop with Newton-Raphson algorithm with objective Equation (2.41). This SS method can converge rapidly in systems where the fugacity coefficient has a weak dependence on phase composition [65]. However, the convergence becomes extremely slow when approaching phase boundary or critical point zone. The traditional approach is to estimate an phase composition for two-phase and initialize the computation. If one phase vanishes during iterating, it turns out to be single phase system [60]. Actually, a more efficient way to start the computation is using the approximated phase composition from TPD test. Then the computation can be combined with General Dominant Eigenvalue Method (GDEM) acceleration algorithm after several iterations [64]. This method has been proved effective in most situations even around phase boundary or critical point. In addition, Gibbs free energy minimization method is also proposed by Michelsen [65]. The involved objective function is as Equation (2.40). This equation can be resolved by Newton secondary order minimization algorithm like Murray algorithm [72] which can ensure a safe convergence at low computational cost in critical regions. But the computational time and complexity far exceed the SS algorithm + GDEM acceleration algorithm. Nichita et al. [73] has extended the Gibbs energy

minimization with a global Tunneling optimization method for multiphase equilibria calculation. The objective equation is formulated the same as Equation (2.41).

$$\overline{G(n)} = \frac{G(n)}{RT} = \sum_{i=1}^{nc}\sum_{j=1}^{np} n_{ji} ln(f_{ji}\,(x_j)) \tag{2.40}$$

Constrained by

$$n_i = \sum_{j=1}^{np} n_{ji}\,, \qquad 0 \le n_{ji} \le n_i, \qquad i = 1, nc, \qquad j = 1, np$$

This global searching method is explored because the local searching algorithm may fail to find the correct solution when faced with non-convex function in a more complex system such as the Liquid-Liquid-Vapor equilibrium system. Similar analysis has also been mentioned by Baker, et al. [61].

$$obj(\psi_v) = \sum_{i=1}^{N_c} \frac{z_i(\mathrm{K}_i - 1)}{1 + \psi_v(\mathrm{K}_i - 1)} \tag{2.41}$$

$$\frac{\partial obj(\psi_v)}{\partial \psi_v} = -\sum_{i=1}^{N_c} \frac{z_i(\mathrm{K}_i - 1)^2}{(1 + \psi_v(\mathrm{K}_i - 1))^2} \tag{2.42}$$

Okuno et al. [74] has reformulated the Rachford-Rice equation and turned the root finding algorithm such as aforementioned successive substitute algorithm into the minimization of a convex function. The objective function is written as Equation (2.43). The constraint region (Equation(2.44)- (2.45)) is to ensure the non-negativity of phase component. This method has been proved rather efficient and robust even in dealing with phase boundary and around critical point zone.

$$F(\beta) = \sum_{i=1}^{N_c} (-z_i\, ln(|t_i|)) \tag{2.43}$$

$$t_i = 1 - \sum_{j=1}^{N_p - 1} \beta_j(1 - \mathrm{K}_{ij}),\ \mathrm{i}=1, N_c$$

N_p denotes the number of phase.

This equation is subject to

$$\alpha_i^T \beta \le b_i \tag{2.44}$$

Where, β is phase mole fraction. α_i, b_i define as,

$$\alpha_i = 1 - \mathrm{K}_{ij} \tag{2.45}$$

$$b_i = min\left\{1 - z_i, min\{(1 - \mathrm{K}_{ij})\}\right\},\ \mathrm{i}=1, N_c,\ \mathrm{j}=1, N_p$$

Even though the global searching algorithm may provide an accurate solution, the computational cost is extremely large compared with local search method. For the CFD modeling, an acceptable solution and efficient computation are the main concern. Hence a local searching algorithm has been chosen in current research.

Distinct with the conventional flash computation which requires the positive sign of phase mole fraction to ensure the final positive phase composition, Curtis and Michelsen [75] has proposed the unconstrained negative flash method. The negative flash approach does not need to constrain the phase mole fraction during iterating process. Actually, a non-negative phase equilibrium composition exists and satisfy the mass balance equation (Equation (2.38)) even for single phase if vapor mole fraction ψ_v lies in the range of $\frac{1}{1-K_{max}} < \psi_v < \frac{1}{1-K_{min}}$, where K_{max}, K_{min} represents the maximum and minimum value of phase equilibrium constant, respectively. These two limits are the two asymptotes of Rachford-Rice equation. This new algorithm has been proven helpful in ensuring the continuity of thermal properties in the phase boundary and checking the phase state in compositional reservoir simulation [75]. The other advantage by using negative flash is to be able to avoid solving TPD test. The resultant ψ_v from negative flash computation can directly indicate phase state. But it turns out that the resultant vapor fraction and phase composition is very sensitive to the initialized equilibrium constant which leaves the robustness of this method into question.

2.4 Isoenergetic-Isochoric Flash

The isoenergetic-isochoric or internal energy-specified volume (UV) flash is usually performed to simulate the dynamic filling of a process vessel [76]–[79]. This computation is needed in CFD modelling as the process of searching P, T from u,

v and n as explained in Section 3.4.1. The related formulas are shown as Equation (2.46). Unlike the usual isothermal-isobaric (TP) flash or isenthalpic-isobaric (HP) flash, no intensive variables like temperature and pressure are known as a priori. Instead, the temperature and pressure are the solutions needed to be found. In the current CFD work, UV flash is needed to compute the final temperature, pressure and composition using updated internal energy (u^*), specific volume (v^*) and composition given by the flow solver (4-Equation model or 6-Equation model described in following chapters). Due to the high complexities, until now, there is still very limited research about this kind of flash. Previous research concerning resolving this flash is through nested loop method by adopting $\frac{1}{T}$, $ln(P)$ and $ln(K)$ or $ln(T)$, $ln(P)$, molar number as independent variables and keep iterating until converging to the correct u^* and v^*in Equation (2.46) [76], [80]. The key part of this method is isothermal flash (TP flash). Later on, some researchers have been inspired by the work of Michelsen [80] and replace the iterating variable $ln(T)$, $ln(P)$ and molar number with $ln(T)$, v and molar number [77]. According to [77], the new iterating method can improve the convergence around phase boundary. Recently, a more efficient and robust algorithm based on global entropy maximization method has been proposed by Castier [79]. According to phase equilibrium theory, the equilibrium state also corresponds to the maximized entropy in this system. Unlike previous method, this algorithm has adopted the internal energy, volume and molar number of each phase as independent variables. According to Castier [79], this method can give better performance around phase boundary. But compared with the nested loop method, entropy maximization algorithm is much more complex to implement. Considering the current research objective is focused on the simple vapor-liquid equilibrium system, the conventional nested loop approach can satisfy the need. Therefore, the nested loop approach [76] coupled with TP flash has been selected for current study.

$$u^* = \psi_v u_v + (1-\psi_v)u_l$$
$$v^* = \psi_v v_v + (1-\psi_v)v_l \quad (2.46)$$
$$z_i^* = \psi_v y_i + (1-\psi_v)x_i$$

In which, u^*, v^* are specific internal energy and specific volume, respectively. z_i^* is the overall molar fraction for each component.

2.5 Single phase non-equilibrium thermodynamics

Except the two-phase equilibrium state, there also exists single phase state. In this situation, the process of computing P and T from u^*, v^* becomes much simpler. The equation needs to be resolved only is energy balance equation (Equation (2.47)). For PR EoS, the relation between internal energy and temperature is implicit. An iterating process is necessary to obtain temperature. Then P can be computed directly by Equation (2.1). The other important point related with single phase is to decide the phase state (liquid phase or vapor phase). This become extremely important in supercritical condition because the limit between liquid and vapor is much blur compared with subcritical condition. The choosing of fluid state is based on compressibility factor. If three roots are detected, the minimum value with lowest Gibbs energy will be selected. If only one root is found, it will be compared with critical value 3.5*B. B is computed with Equation (2.4). If lower than the critical value, it will be regarded as liquid. Otherwise, it will be vapor. The middle value of the cubic equation is dismissed to avoid the non-stable situation.

$$u^* = \psi_v u_v + (1-\psi_v)u_l \quad (2.47)$$

$\psi_v = 0$ for single liquid phase; $\psi_v = 1$ for pure vapor phase

2.6 Validation of Vapor-Liquid Equilibrium

To validate the vapor-liquid equilibrium model, isothermal-isobaric flash are computed for four binary hydrocarbon and nitrogen system which are widely used in industry. The thermal properties for each component are summarized in Table 2.1. T_c, P_c are the critical temperature and pressure respectively. ω is acentric factor. M_w denotes the molar weight of the species. BIP stands for binary interaction parameter which is taken from the references [81]–[84]. The calculation results are compared with experimental data [81]–[84] as presented in Figure 2.1. It can be noticed from the plots that the match with experimental data is good at low pressures but fails at high pressures, especially close to the critical point. Since the only tunable parameter for the equation of state model is the binary interaction parameter (BIP), it is expected that using temperature dependent interaction parameters could improve the accuracy [82], [84]. It is noteworthy to mention that the mixture critical pressure rises significantly as the concentration of nitrogen is increasing, as previously depicted in Figure 1.7. Whereas the mixture critical temperature reduces as more nitrogen exists in the mixture. In addition, a linear relation between the critical point of a mixture and that of each pure species does not exist. This is an interesting point that could be investigated in future work in order to build better UV flashes.

Table 2.1 Thermal properties and binary interaction parameter for the hydrocarbon and nitrogen system.

Species	T_c/K	P_c/bar	ω	M_w/kg/mol^3	BIP
nC5h12	469.7	33.7	0.2515	0.072	0.0657
nC6h14	507.6	30.25	0.301261	0.086	0.0657
nC7h16	540.3	27.36	0.3495	0.10	0.0971
nC12h26	658	18.2	0.576385	0.17034	0.19
N2	126.2	33.9	0.0377	0.028	0

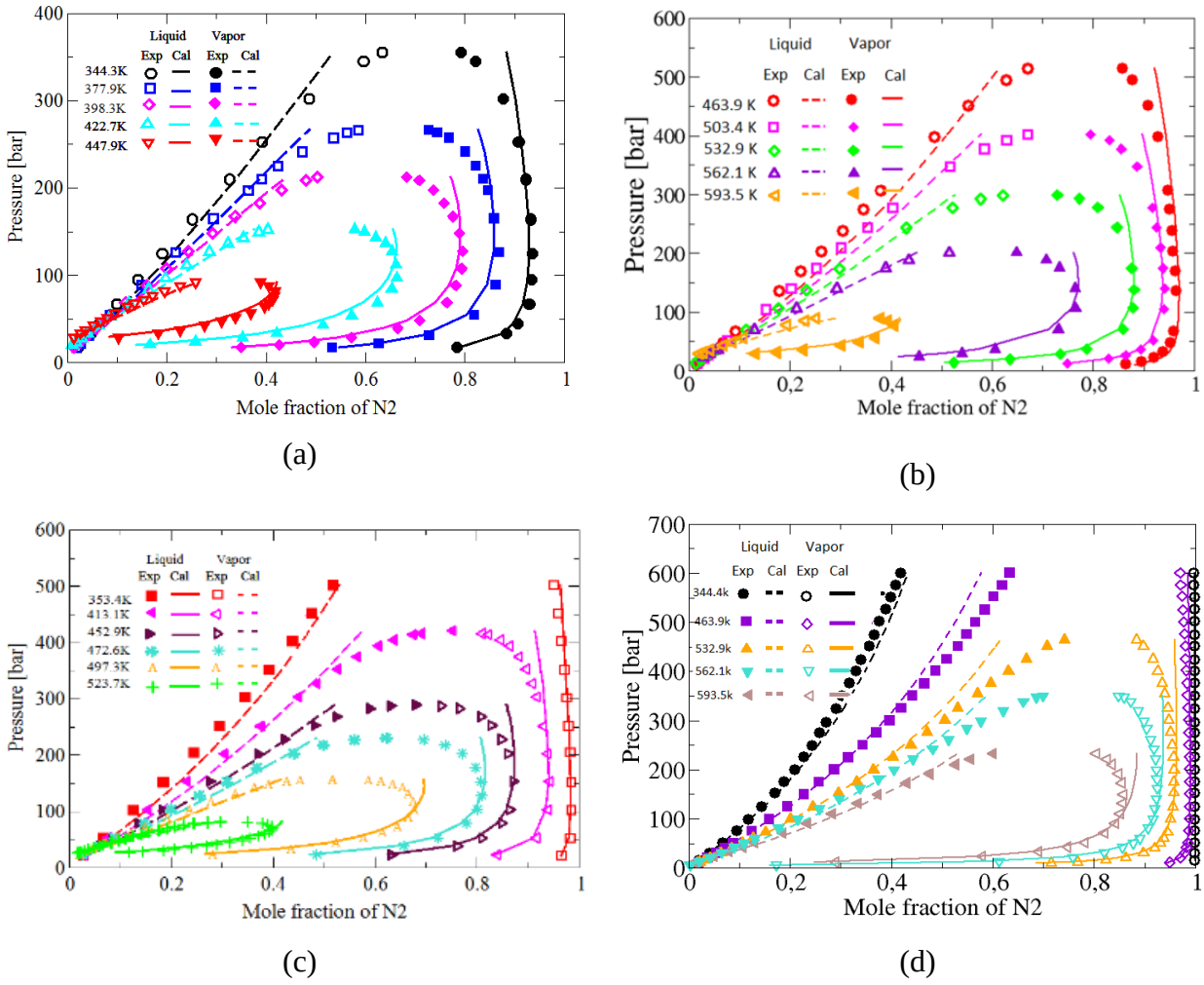

Figure 2.1 Vapor-liquid equilibrium of hydrocarbon and nitrogen mixture. (a) n-C5H12 and N2; (b) n-C6H14 and N2; (c) n-C7H16 and N2; (d) n-C12H26 and N2.

2.7 Chapter Conclusion

This chapter has introduced the fundamentals of thermodynamics equilibrium theory and describe a series of thermal models selected in current study. Specifically, the detailed theoretical background about stability analysis, phase split computation and Isoenergetic-Isochoric flash have been presented. Validation of vapor-liquid equilibrium calculation with experimental data for different hydrocarbons and nitrogen systems has also been conducted.

3 Mathematical model of flow solver

3.1 The original 7-Equation models

This thesis is based on the in-house code IFP-C3D [55]. This solver already contains the fully compressible two-fluid 7-Equation model initiated by Baer and Nunziato [54], and proposed for two-phase flows by Saurel and Abgrall [50]. This fully non-equilibrium 7-Equation model is the most general two-phase flow model, in which each phase has its own pressure, velocity and temperature, and is governed by its own set of conservation equations. More precisely, it is based on a fully compressible model composed of three balance equations for the gas phase and three balance equations for the liquid phase, together with a transport equation for one of the phase volume fraction. In this two-fluid model, gas and liquid thermodynamics are solved independently by two different equation of state (EoS). Particularly, the liquid phase is described by a single-component Stiffened Gas (SG) EoS and gas phase is solved with a multi-component ideal gas EoS. The 7-Equation balance system is described by Equations (3.1)-(3.7), as they have been implemented in IFP-C3D by Habchi [33]. Among them, Equation (3.1) is the transport equation of liquid volume fraction. The right-hand side (RHS) of this equation includes different source terms which correspond to the contributions of the relaxation of pressure $\dot{\alpha}_P$, temperature $\dot{\alpha_T}$ and Gibbs energy relaxation term $\frac{\dot{m}}{\rho^I}$ ($\dot{m} = \sum_k \dot{m}_{g,k}$) at interfaces where, k denotes the species index. Such a non-equilibrium model is built using relaxation methods with finite characteristic time for velocity, pressure, temperature and chemical potential at the phase interface [54], [85]. The instantaneous stiff relaxation approaches have been proven to be numerically stable when applied to the pressure and velocity relaxation [50]. At the same time, these stiff relaxation procedures have also been used for the temperature and Gibbs free energy terms [33], [86]. The ρ^I term in Equation (3.1) denotes the density at the interface. Equations (3.2)-(3.4)

(respectively (3.5)-(3.7)) represent gas (respectively liquid) phase balance equations. Subscript p denotes phase state (gas or liquid). In the continuity Equations ((3.2), (3.5)), the RHS terms $\dot{m}_{g,k}, \dot{m}_{l,k}$ are the evaporated or condensed mass due to the chemical potential relaxation process. Mass is conserved during phase transition process, $\dot{m}_{g,k} + \dot{m}_{l,k} = 0$. In the momentum and energy equations (3.3), (3.4) and (3.6), (3.7), $\tau_{p,ij}^{L,T}$ is the shear stress tensor expressed as $\tau_{p,ij}^{L,T} = \tau_{p,ij}^{L} + K_0 \tau_{p,ij}^{T}$ with, $K_0 = 1$ for turbulent flows. The superscripts *L, T* denotes laminar and turbulent flow, respectively. In this work, 2D or 3D test cases are simulated using the Large Eddy Simulation (LES) framework, where the subgrid scale Smagorinsky model is adopted [33]. The interfacial velocity V_I and interfacial pressure P_I are assumed according to Baer and Nunziato model ($V_I = V_{l,i}$, $P_I = P_g$). In the energy Equations (3.4), (3.7), e_g, e_l represent the internal energy of gas phase and liquid phase, respectively. Since energy is not fully conserved, the equation system belongs to the quasi-conservative type. The $q_{p,i}^{L,T}$ term is the heat flux and similar to the shear stress, it is modelled as $q_{p,i}^{L,T} = -\lambda_p^{L,T} \frac{\partial T_p}{\partial x_i}$, where the term at right hand side is the heat conduction term (Fourier's law). The turbulent contribution for the heat conduction coefficient λ_p^T is taken from a specified turbulent Prandtl number, $Pr_t = 0.9$. However, the laminar conductivity coefficient contribution, computed with Wilke and Lee correlation [87], is only considered for liquid phase. The velocity relaxation term F_d appeared in Equations (3.3)-(3.4), (3.6)-(3.7) represents the effect of the drag force at the interface on the variation of momentum and internal energy. The internal energy at the interface e_I as defined by Zein *et al*. [86] is also used to account for internal energy variation due to phase change.

$$\frac{\partial \alpha_l}{\partial t} + V_I \frac{\partial \alpha_l}{\partial x_i} = \dot{\alpha}_P + \dot{\alpha_T} + \frac{\dot{m}}{\rho^I} \tag{3.1}$$

$$\frac{\partial \alpha_g \rho_{g,k}}{\partial t} + \frac{\partial \alpha_g \rho_{g,k} V_{g,i}}{\partial x_i} = \dot{m}_{g,k} \tag{3.2}$$

$$\frac{\partial \alpha_g \rho_g V_{g,i}}{\partial t} + \frac{\partial \alpha_g \rho_g V_{g,i} V_{g,j}}{\partial x_i} = \frac{\partial a_g P_g}{\partial x_i} + \mathrm{P}_I \frac{\partial \alpha_g}{\partial x_i} + \frac{\partial \alpha_g \tau_{g,ij}^{L,T}}{\partial x_i} + F_d \tag{3.3}$$

$$\begin{aligned} &\frac{\partial \alpha_g \rho_g e_g}{\partial t} + \frac{\partial \alpha_g \rho_g V_{g,i} e_g}{\partial x_i} \\ &= -\alpha_g P_g \frac{\partial V_{g,i}}{\partial x_i} - \frac{\partial \alpha_g q_{g,i}^{L,T}}{\partial x_i} + \alpha_g \tau_{g,ij}^{L,T} \frac{\partial V_{g,i}}{\partial x_j} + V_I F_d + P_I \dot{\alpha}_P + \kappa \dot{\alpha_T} + e_I \dot{m} \end{aligned} \tag{3.4}$$

$$\frac{\partial \alpha_l \rho_{l,k}}{\partial t} + \frac{\partial \alpha_l \rho_{l,k} V_{l,i}}{\partial x_i} = -\dot{m}_{g,k} \tag{3.5}$$

$$\frac{\partial \alpha_l \rho_l V_{l,i}}{\partial t} + \frac{\partial \alpha_l \rho_l V_{l,i} V_{l,j}}{\partial x_i} = \frac{\partial a_l P_l}{\partial x_i} + \mathrm{P}_I \frac{\partial \alpha_l}{\partial x_i} + \frac{\partial \alpha_l \tau_{l,ij}^{L,T}}{\partial x_i} - F_d \tag{3.6}$$

$$\begin{aligned} &\frac{\partial \alpha_l \rho_l e_l}{\partial t} + \frac{\partial \alpha_l \rho_l V_{l,i} e_l}{\partial x_i} \\ &= -\alpha_l P_l \frac{\partial V_{l,i}}{\partial x_i} - \frac{\partial \alpha_l q_{l,i}^{L,T}}{\partial x_i} + \alpha_l \tau_{l,ij}^{L,T} \frac{\partial V_{l,i}}{\partial x_j} - V_I F_d - P_I \dot{\alpha}_P - \kappa \dot{\alpha_T} - e_I \dot{m} \end{aligned} \tag{3.7}$$

Finally, the relaxation terms are defined as follows with g and l representing gas phase and liquid phase respectively.

$$\dot{\alpha}_P = \omega\left(P_g - P_l\right) \tag{3.8}$$

$$\dot{\alpha_T} = \frac{\theta}{\kappa}\left(T_g - T_l\right) \tag{3.9}$$

$$F_d = \lambda(V_{g,i} - V_{l,i}) \tag{3.10}$$

$$\dot{m} = \phi\left(\mu_g - \mu_l\right) \tag{3.11}$$

In IFP-C3D [51], stiff relaxation procedures have been used for the pressure ($\omega \rightarrow \infty$), velocity ($\lambda \rightarrow \infty$), temperature ($\theta \rightarrow \infty$), and Gibbs free energy ($\phi \rightarrow \infty$) terms.

3.2 From 7-Equation to 6-Equation model

Considering the main aim of this thesis is to model the injection process at high temperature and high pressure (HTHP) and to investigate the transition from subcritical to supercritical flow conditions where the variation of physical properties may be nonlinear, as shown in Figure 1.5, thus an accurate real fluid EoS needs to be considered. As a trade-off of computational efficiency and accuracy, Peng-Robinson (PR-EoS) is selected in this work. Due to the non-linear nature of such cubic PR-EoS, the above stiff relaxation procedures for solving Equations (3.8)-(3.11) cannot be applied and the computation of the thermodynamics variables and derivatives need to be completely rewritten and implemented in IFP-C3D. This is the reason why, a transient thermodynamic phase equilibrium solver has been constructed based on PR-EoS. The efficiency of such solver has been proved by recent researchers. For instance, Qiu [88] has succeeded in implementing the phase equilibrium solver based on the entropy maximization theory into a multiphase flow solver (KIVA-3V) and applied it to the modeling of HTHP injection process in ICE. The Engine Combustion Network (ECN) Spray A [44] has also been simulated with the assumption of no phase change in the transcritical conditions [48] as well as considering the phase change based on PR EoS [32]. Using such phase equilibrium solver, the non-conservative equation of liquid volume fraction (Equation (3.1)) vanishes and the 7-Equation system is simplified to a 6-Equation system, as shown by the following Equations (3.12)-(3.17).

$$\frac{\partial \alpha_g \rho_{g,k}}{\partial t} + \frac{\partial \alpha_g \rho_{g,k} V_{g,i}}{\partial x_i} = \dot{m}_{g,k} \tag{3.12}$$

$$\frac{\partial \alpha_g \rho_g V_{g,i}}{\partial t} + \frac{\partial \alpha_g \rho_g V_{g,i} V_{g,j}}{\partial x_i} = \frac{\partial a_g P_g}{\partial x_i} + \mathrm{P}_I \frac{\partial \alpha_g}{\partial x_i} + \frac{\partial \alpha_g \tau_{g,ij}^{L,T}}{\partial x_i} + F_d \tag{3.13}$$

$$\frac{\partial \alpha_g \rho_g e_g}{\partial t} + \frac{\partial \alpha_g \rho_g V_{g,i} e_g}{\partial x_i} = -\alpha_g P_g \frac{\partial V_{g,i}}{\partial x_i} - \frac{\partial \alpha_g q_{g,i}^{L,T}}{\partial x_i} + \alpha_g \tau_{g,ij}^{L,T} \frac{\partial V_{g,i}}{\partial x_j} + V_I F_d \tag{3.14}$$

$$\frac{\partial \alpha_l \rho_{l,k}}{\partial t} + \frac{\partial \alpha_l \rho_{l,k} V_{l,i}}{\partial x_i} = \dot{m}_{l,k} \tag{3.15}$$

$$\frac{\partial \alpha_l \rho_l V_{l,i}}{\partial t} + \frac{\partial \alpha_l \rho_l V_{l,i} V_{l,j}}{\partial x_i} = \frac{\partial a_l P_l}{\partial x_i} + \mathrm{P}_I \frac{\partial \alpha_l}{\partial x_i} + \frac{\partial \alpha_l \tau_{l,ij}^{L,T}}{\partial x_i} - F_d \tag{3.16}$$

$$\frac{\partial \alpha_l \rho_l e_l}{\partial t} + \frac{\partial \alpha_l \rho_l V_{l,i} e_l}{\partial x_i} = -\alpha_l P_l \frac{\partial V_{l,i}}{\partial x_i} - \frac{\partial \alpha_l q_{l,i}^{L,T}}{\partial x_i} + \alpha_l \tau_{l,ij}^{L,T} \frac{\partial V_{l,i}}{\partial x_j} - V_I F_d \tag{3.17}$$

$$\alpha_g = \psi_v * \frac{v_g}{\psi_v * v_g + (1 - \psi_v) * v_l} \tag{3.18}$$

$$\alpha_l = 1 - \alpha_g \tag{3.19}$$

$$\dot{m}_{l,k} + \dot{m}_{g,k} = 0 \tag{3.20}$$

As a matter of fact, by solving the UV flash (see Section 2.4), the α_l can be updated readily by Equations ((3.18)-(3.19)), where ψ_v is the multicomponent vapour molar fraction and $v_{g,}\, v_{l,}$ are the specific volume of gas phase and liquid phase, respectively. In mass balance Equations ((3.12), (3.13)), $\dot{m}_{p,k}$ represents the mass transfer between different phases obtained also by the UV flash procedure. Different with Equations ((3.1)-(3.7)), the molecular viscosity and the thermal conduction coefficient in current system are computed with Chung's correlations for multicomponent fluids [89]. It is worth noting that the new developed phase equilibrium solver has replaced the original stiff relaxation procedures for pressure, temperature and Gibbs energy. Nevertheless, the velocity relaxation term F_d is still needed and in this work, a stiff relaxation procedure have been used ($\lambda \rightarrow \infty$).

3.3 From 6-Equation to 4-Equation systems

As further reducing the equation system by assuming liquid and gas flow owning the same velocity, pressure and temperature, the aforementioned 6-Equation system has been simplified to the 4-Equation system formulated as Equations (3.21)-(3.24). In fact, the above assumption implies the flow system is subjected to mechanical and thermal equilibrium. But mass balance Equations (3.21)-(3.22) are kept the same as the aforementioned 6-Equation and 7-Equation systems. Basically, these mass conservation equations can also be formulated using the mass fraction of species [32] [90] instead of partial density in each phase. The RHS terms $\dot{m}_{l,k}, \dot{m}_{g,k}$ are the transfered mass during phase transition process. Equations ((3.23)-(3.24)) are the mixture momentum and energy equations, respectively. Compared with 6-Equation or 7-Equation model, the non-equilibrium term $P_I \frac{\partial \alpha_p}{\partial x_i}$ (Equations (3.3), (3.6), (3.13), (3.16)) has disappeared in mixture momentum Equation (3.23). Another main difference is that there is no velocity relaxation in the 4-Equation model, which explains the disappearance of the F_d term from Equations ((3.3)-(3.4), (3.6)-(3.7), (3.13)-(3.14), (3.16)-(3.17)). The thermal closure equation is also the Peng-Robinson EoS. Different with the 6-Equation system, volume fraction terms α_g, α_l only appear in the mass conservation Equations (3.21)-(3.22). The method of computing heat and viscous fluxes are exactly as for the aforementioned 6-Equation system.

$$\frac{\partial \alpha_l \rho_{l,k}}{\partial t} + \frac{\partial \alpha_l \rho_{l,k} V_i}{\partial x_i} = \dot{m}_{l,k} \tag{3.21}$$

$$\frac{\partial \alpha_g \rho_{g,k}}{\partial t} + \frac{\partial \alpha_g \rho_{g,k} V_i}{\partial x_i} = \dot{m}_{g,k} \tag{3.22}$$

$$\frac{\partial \rho V_i}{\partial t} + \frac{\partial \rho V_i V_j}{\partial x_i} = \frac{\partial P}{\partial x_i} + \frac{\partial \tau_{ij}^{L,T}}{\partial x_i} \tag{3.23}$$

$$\frac{\partial \rho e}{\partial t} + \frac{\partial \rho V_i e}{\partial x_i} = -P\frac{\partial V_i}{\partial x_i} - \frac{\partial q_i^{L,T}}{\partial x_i} + \tau_{ij}^{L,T}\frac{\partial V_i}{\partial x_j} \tag{3.24}$$

This 4-Equation model is the simplest flow model for the relaxation solver [11]. Compared with previous researches [11], [91], the novelty of current research lies in the utilization of a real fluid phase equilibrium model for the full multicomponent system, especially in the liquid phase in addition to gas phase. The work from Allaire [92] has extended the current 4-Equation system with one extra volume fraction transport equation to 5-Equation system for better modelling the interfaces only at mechanical equilibrium. The latest research from Chiapolino [11] has used vapor-liquid-equilibrium (VLE) model for single component liquid. Moreover, the current 4-Equation model with phase equilibrium model has proved to share high similarity with the very recent research from Matheis and Hickel [32]. The main difference resides in their fully conservative formulation using the total energy for the energy transport equation; while a non-conservative internal energy equation is used in the present work, as expressed in Equation (3.24). The second difference lies in the mass transport equations. In the present work, the mass conservation is carried out by considering each phase and component separately instead of a homogenous fluid as in Matheis' s study [32].

3.4 Numerical methods

3.4.1 Coupling flow solver with Phase Equilibrium solver

The phase equilibrium solver (also referred as thermo-solver) have been coupled with both 6-Equation and 4-Equation flow solvers described in previous sections. This chapter will have a concise description of the coupling of thermo-solver and flow solvers. A detailed description of the IFP-C3D flow solver can be found in [55]. In this original in-house code, the transport equations (mass, momentum, energy balance equations) are solved based on a time-splitting numerical scheme including four stages sequentially referred as Phase A, B, C and D, as depicted in Figure 3.1. Phase A computes the effect of spray and combustion as source terms. In Phase B or Lagrangian phase, the cell is moved with the fluid and all the physical properties such as pressure, temperature and velocity except convection terms are calculated implicitly by a Lagrangian manner using the SIMPLE numerical scheme, including a BICGSTAB and SOR preconditioners [55]. Then, in Phase C (Eulerian stage), the grid cell boundaries are mapped back to their original position (in the absence of wall movement). The obtained solutions from Phase B are updated in the Phase C using a quasi-second-order-upwind (QSOU) explicit numerical scheme. The Minmod slope limiter is used for scalar fluxes, and Van Leer slope limiter is used for momentum fluxes (see [55]). The final stage phase D contains the stiff relaxation algorithms for the interfacial velocity (7- and 6-Equation systems only), pressure, temperature and chemical potentials (if with phase change) [33]. Inside the original IFP-C3D code, the inherent EoS is the ideal gas EoS for gas phase and the stiffened gas EoS for liquid phase. In the present work, all the subroutines in the code involving EoS have to be replaced by PR-EoS (see the subroutines written in red, in Figure 3.1). Another significant difference is that liquid and gas phases are both aimed for solving multicomponent system. Thereby, dissolved gas part is considered in liquid phase which makes it totally distinct from previous research using SG-EoS [11], [33], [86].

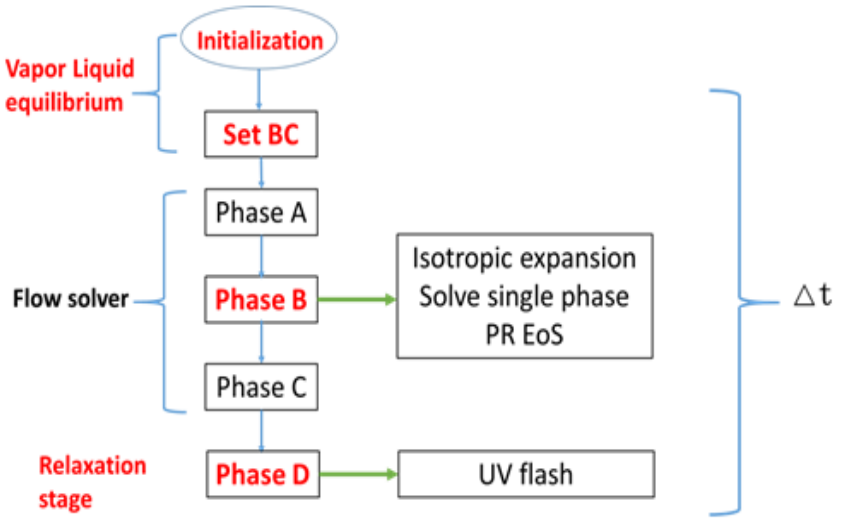

Figure 3.1 Schematic of coupling of thermo-solver with flow solver in IFP-C3D

First, as for the initialization of the simulation and to obtain the phases composition at given temperature and pressure, a phase equilibrium computation or vapor-liquid equilibrium (VLE) calculation is carried out. This initial VLE computation has obviously assumed the fluid at the beginning is in saturated state. Next, if the simulated configuration includes flow inlets or outlets, VLE computation is performed again to keep the boundary conditions in saturated state. Then, transport equations are solved as described above from Phase A to Phase D. Within the Lagrangian phase B, with the update of pressure and temperature during SIMPLE algorithm, a series of thermal properties need to be updated correspondingly with PR EoS. The resolving of PR EoS at phase B is for each single liquid phase or vapor phase (in the 6-Equation model case) or a homogeneous mixture (in the 4-Equation model case). With the known internal energy, specific volume and component composition from the advection Phase C stage, a new temperature, pressure and phase compositions need to be calculated for a new time-step (or cycle). This is the role attributed to the UV flash model carried out in Phase D. Actually, the UV flash process with PR EoS has replaced the relaxation procedures for the pressure, the temperature and the Gibbs energy in original 7-Equation model. The coupled models

with PR EoS for 6-Equation and 4-Equation are referred as 6EQ-PR and 4EQ-PR, respectively.

3.4.2 Detailed descriptions of the new Phase D stage

The highlights of the overall thermal model is concentrated on the Phase D stage. The descriptions below are mainly based on 6EQ-PR system, but 4EQ-PR follows very similar procedure. The thermal solver is based on the following three assumptions:

1) Instantaneous thermodynamics equilibrium is assumed and VLE computation is applied which is similar to previous stiff relaxation of pressure, temperature and Gibbs energy of the 7-Equation model. The final pressure and temperature for the two-phase mixture are the same (Equation (3.25): condition (a, b)) and at mechanical and thermal equilibrium. At the same time, the fugacity of liquid and gas phases are relaxed to be equal too (Equation (3.25): condition (c)), thus relaxing the two-phase mixture at thermodynamic equilibrium. However, if the fluid is in thermodynamics single phase state in which the fluid is defined mostly as liquid or gas, the temperature and pressure are directly computed using the density and internal energy given by Phase C flow solver.

$$
\begin{aligned}
&\text{(a) } P = P_{liquid} = P_{gas} \\
&\text{(b) } T = T_{liquid} = T_{gas} \\
&\text{(c) } f_{liquid} = f_{gas} \\
&\text{(d) } \mathrm{e} = \frac{\alpha_l \rho_l}{\rho}\mathrm{e}_l + \frac{\alpha_g \rho_g}{\rho}\mathrm{e}_g \quad (\alpha_g, \alpha_l\text{: phase volume fraction}) \\
&\text{(e) } \rho = \alpha_g \rho_g + \alpha_l \rho_l \ (\alpha_g, \alpha_l\text{: phase volume fraction})
\end{aligned}
\tag{3.25}
$$

2) A virtual amount of the second phase is assumed to exist as the flow is situated in thermodynamics single phase state. This is not only to keep the

characteristics of two-phase flow for 6-Equation system, but also to make the simulation more approaching reality in conditions where numerous bubble nucleus exist in the liquid bulk, for instance. However, one advantage of the 4-Equation system compared to 6-Equation is to be capable of simulating pure single liquid phase or gas phase without adding any trifle impurities.

3) The mixing of different components in each phase are realized with van der Walls mixing rule as stated in Section 2.1 which differs significantly with the widely applied ideal gas mixing rule [19], [91]. In addition, the molecular mutual effect between different components is controlled by binary interaction parameter (BIP).However, the mixing principles for internal energy and density are different formulated as Equation (3.25), conditions (d, e). These two equations can also be written with vapor molar fraction (Equations (3.30)-(3.31)).

The detailed procedures about the implementation of the new relaxation Phase D are shown in the flowchart (Figure 3.2).

1) After solving the flow equations (Equations (3.12)-(3.17) for the 6EQ-PR), the molar fraction of each component z_k and non-equlibrium phase composition $x_k^{'}$, $y_k^{'}$ are calculated with Equations ((3.26)-(3.27) using the updated non-equilibrium specific density $(\alpha_p \rho_{p,k})^{'}$ .The initial equilibrium constant $K_i^{'}$ and non-equlibrium vapor fraction $\psi_v^{'}$ are estimated by Equations (2.37) ($K_i = \frac{y_i}{x_i} = \frac{\varphi_i^l}{\varphi_i^v}$) and (3.29). Then, overall molar internal energy u_0 and specific volume v_{mix} are computed with Equations (3.30) and (3.31), respectively. Initial pressure, $P^{'}$ and temperature, $T^{'}$ from last time step are taken as the initial values for the UV flash iteration procedure.
2) Then to verify the actual state of the fluid, a TPD analysis is performed with the method described in Section 2.3.1. If the result from TPD analysis proves the fluid to be stable, the phase composition and vapor fraction will be kept

the same as the initial values ($x_k^{'}$, $y_k^{'}$) and $\psi_v^{'}$, respectively. Otherwise, a phase spilt computation (TP flash) with the method described in Section 2.3.2 will be conducted to obtain the new real phase composition (x_k, y_k).

3) Correspondingly, the new molar internal energy $u_g^{'}$ and $u_l^{'}$ for gas and liquid phases are recomputed with Equation (2.7) ($u_d = \int_{\infty}^{v}\left[T\left(\frac{\partial P}{\partial T}\right) - P\right]dv$). The specific volume $v_g^{'}$ and $v_l^{'}$ for each phase are computed through solving PR-EoS directly. The strategy to search the roots can be found in Appendix A. Then mixing specific energy $u_0^{'}$ and speficific volume $v_{mix}^{'}$ are recalculated with Equations (3.30)-(3.31).

4) The residuals for molar energy ε_u and specific volume ε_v are evaluated with Equations (3.34). If both tolerances are satisfied, the iterating process is completed and exit the loop. Otherwise, the pressure $P^{'}{}^{'}$ and temperature, $T^{'}{}^{'}$ are updated with the Newton algorithm that can be found in the work of Saha and Carroll [76]. With these new $P^{'}{}^{'}$,$T^{'}{}^{'}$, the previous three steps are repeated, as depicted in the flowchart (Figure 3.2) until the convergence is reached.

5) Finally, the thermal and transport properties are updated with the equilibrium P, T, and phase compositions x_k , y_k.

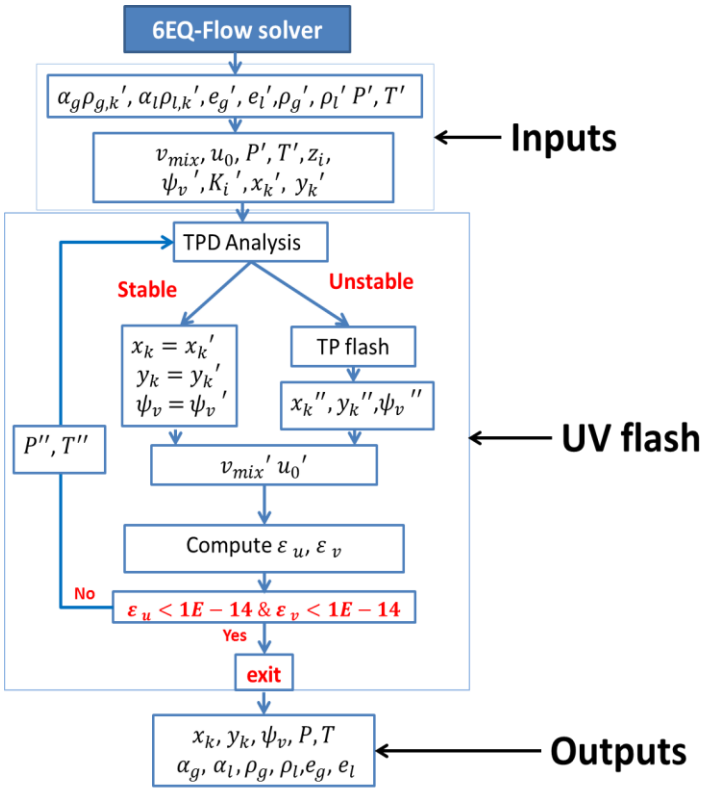

Figure 3.2 Schematic procedures of Phase D stage

One intriguing point, different from previous work from Matheis et al. [32] is that the fluid is always in two-phase state while using the 6EQ-PR model. Fundamentally, like the 7-Equation, the 6-Equation system requires that there are always two phases existing in the flow. In other words, even if the initial state is pure gas, a virtual amount of liquid (Y~1E-6) is existed in the fluid (see assumption 2 above). However, this assumption is not necessary for the 4-Equation system, which means initial fluid can be pure liquid ($\alpha_g = 0$) or pure gas ($\alpha_g = 1$) state as using the 4EQ-PR model. As for 4-Equation system, the whole phase D stage is exactly the same as 6-Equation system, except few differences related to the inputs and outputs calculations. For example, since the 4-Equation system is for a homogeneous fluid, the initial v_{mix} and u_0 can be computed directly using Equation (3.32) instead of using Equations (3.30)-(3.31). Other thermal properties like the liquid and gas speed of sounds (Cs_{gas}, Cs_{liq}) are calculated indepedently for each phase with Equation (2.13).

Whereas for 4-Equation system, the mixture speed of sound Cs_{mix} is also used and computed using the Wood formula as Equation (3.35) [93].

$$z_k = \frac{(\sum_p \alpha_p \rho_{p,k})\, \mathrm{M_{w}}_{mix}}{(\sum_{p,k} \alpha_p \rho_{p,j})\, \mathrm{M_{w_k}}} \tag{3.26}$$

$$x_k = \frac{\alpha_l \rho_{l,k} M_{w_j}}{(\sum_k \alpha_l \rho_{l,k}) \mathrm{M_{w_k}}},$$

$$y_k = \frac{\alpha_g \rho_{g,k} M_{w_j}}{(\sum_k \alpha_g \rho_{g,k})\, \mathrm{M_{w_k}}} \tag{3.27}$$

$$M_{w_{mix}} = \sum_k^{N_c} z_k M_{w_k},\ M_{w_g} = \sum_k^{N_c} y_k M_{w_k}\ , M_{w_l} = \sum_k^{N_c} x_k M_{w_k} \tag{3.28}$$

$$\psi_v = \frac{(\sum_k \alpha_g \rho_{g,k}) M_{w_{mix}}}{\rho M_{w_g}} \tag{3.29}$$

$$u_0 = \psi_v * u_g + (1 - \psi_v) * u_l \tag{3.30}$$

$$v_{mix} = \psi_v * v_g + (1 - \psi_v) * v_l \tag{3.31}$$

$$e = \frac{u_0}{M_{w_{mix}}}, \rho\ = \frac{M_{w_{mix}}}{v_{mix}} \tag{3.32}$$

$$\rho\ = \alpha_g \rho_g + \alpha_l \rho_l\ , \rho_g\ = \frac{M_{w_g}}{v_g},\quad \rho_l = \frac{M_{w_l}}{v_l} \tag{3.33}$$

$$\varepsilon_{\,u} = \left(\frac{u_0 - u_0{}'}{u_0}\right)^2,\ \varepsilon_{\,v} = \left(\frac{v_{mix} - v_{mix}{}'}{v_{mix}}\right)^2 \tag{3.34}$$

$$1/\left(\rho \mathrm{C}^2_{\mathrm{s,mix,W}}\right) = \sum_{\mathrm{p}} \left(\alpha_{\mathrm{p}} / \rho_{\mathrm{p}} \mathrm{C}^2_{\mathrm{p}}\right) \tag{3.35}$$

Where, z_k and x_k, y_k are overall molar fraction (Feed) and phase composition (molar fraction) of each component. ψ_v is the vapor molar fraction. M_{w_k} denotes the molar weight of each component. $M_{w_{mix}}$ represents average molar weight of the mixture. M_{w_g}, M_{w_l} represent molar weight of gas phase and liquid phase, respectively. ρ_g , ρ_l are the density of gas phase and liquid phase,

respectively. u_g and u_l symbols the specific energy for the gas and liquid phase respectively. v_g and v_l denote the specific volume of the gas and liquid phase. ε_u and ε_v are the residul formulars of specific internal energy and specific volume.

3.4.3 Discussion of Hyperbolicity of Euler system

The hyperbolicity of original 7-Equation system and the similar 4-Equation systems have been proved in previous studies [50], [90], [91], [94]. Without considering the relaxation, viscous and heat diffusion terms, the 1D version of 6-Equation and 4-Equation model are therefore hyperbolic with 2N+4 ($u_g\,(N)$, $u_l\,(N)$, $u_g + Cs_{gas}$, $u_g - Cs_{gas,}\, u_l + Cs_{liq}$, $u_l - Cs_{liq}$) and 2N+2 ($u\,(2N)$, $u + Cs_{mix}$, $u - Cs_{mix}$) distinct eigenvalues, respectively. As mentioned before, the sound speed in 6-Equation system is described with distinct Cs_{gas} and Cs_{liq}.While only the mixture sound speed Cs_{mix} is accounted for in the 4-Equation system. However, due to the thermal closure equation is the PR-EoS, there exists an unstable region in the vapor dome where $Cs^2 = -v^2(\frac{\partial P}{\partial v})_s$ (as seen in Figure 3.3) is negative as also discussed by many researchers [90], [95], [96]. In this situation, the value of Cs is not real any more and the hyperbolicity of the flow system therefore lost. However, to fix this problem, some researchers have proposed the composite EoS method [90], [96]. For example, in the work of Wareing [96], the two fluids are resolved with distinct EoS in which the gas phase is computed with PR EoS, while liquid phase is evaluated with tabulated data from Span & Wagner EoS. In this manner, they successfully avoided the negative square sound speed problem. Enlightened by previous studies, the current work also adopt similar composite EoS formulation to circumvent this deficiency [97]. Each phase always owns its PR EoS, and the two-phase mixture state is obtained by a "composite EoS" formulation. During the resolving of PR EoS for each phase, the middle root appearing in the unstable region is omitted (see Appendix A) which furtherly ensure a well-defined speed of sound. In this case, the mixture speed of

sound (Equation (3.35)) used in the 4EQ-PR model is also always defined. Thereby, the hyperbolicity is well preserved in our 4EQ-PR model.

Nevertheless, potential risk of losing hyperbolicity still exists in the flow solver. As illustrated in Section 3.4.1, thermal properties of each phase are updated with PR EoS in Phase B (Lagrangian phase). When subjected to strong expansion or compression wave, the single phase fluid at this stage may enter the unstable region. Once encounter this situation, one remedy is to restart current cycle with smaller time-step (Δt) to ensure the stability of the flow solver. However, more robust numerical schemes are needed in order to be able to deal with metastable fluid properly. More details about this issue can found in [97].

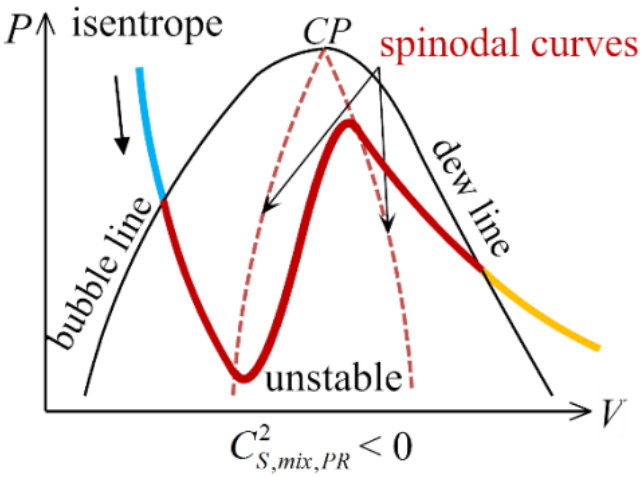

Figure 3.3 Thermodynamic path along an isentropic for multicomponent flow. The two-phase region enclosed by the bubble line and dew line includes the metastable liquid ($Cs^2 > 0$) in the left side, unstable fluid ($Cs^2 < 0$) in the middle zone and the metastable gas ($Cs^2 > 0$) in the right side. The unstable region is limited by the spinodal curves (red dashed line).

3.5 Chapter Conclusion

This chapter firstly describes the mathematical model of the original 7-Equation two fluids system. Based on it, a modified 6-Equation model is introduced which has inherited the original two fluids assumption and replaces the relaxation procedures for the pressure, temperature and Gibbs energy with a phase equilibrium solver (thermo-solver) based on the PR-EOS. However, velocity relaxation term has been kept to ensure the mechanical equilibrium at the interface. Secondly, a more reduced single fluid 4-Equation model with the assumption of full mechanical and thermal equilibrium is described. Compared with 7-Equation and 6-Equation systems, the two fluids characteristics are still present in the mass conservative equations, whereas energy equation and momentum equation are only solved for the mixture flow. Then the numerical method and particularly the coupling method between flow solver and thermo-solver are explained along with a detailed description about phase D (the UV flash in the new Relaxation stage). Finally, one of the main concerns related the hyperbolicity of Euler system with PR-EoS is discussed in the context of the suggested 4EQ-PR and 6EQ-PR models. It has been confirmed in the following chapters that the suggested composite PR-EoS formulation can be helpful to circumvent this issue.

4 1D academic tests with 6EQ-PR and 4EQ-PR

To verify the correct implementation of the thermal solver within the flow system, a series of subcritical, transcritical and supercritical test cases involving cavitation, evaporation and condensation phenomena are conducted with 6EQ-PR and 4EQ-PR models. The discussions regarding the comparison with available numerical results from literature references are presented accordingly.

4.1 1D modelling considering phase change

In this section, all the test cases are simulated using the 4EQ-PR and the 6EQ-PR models with the consideration of evaporation and condensation. Due to the fact that 1D test cases using real fluid phase transition model are very limited in available literature, some of the following test results are compared with similar flow conditions with different equation of state. Since the involved physics are quite the same fundamentally, a qualitative comparison is considered to be useful as a first step of the implementation validation. As explained in section 3.4.1, the 4EQ-PR and the 6EQ-PR models are using the same phase equilibrium solver. Thus, the differences will mainly come from the flow solver. Four cases are conducted in this section, in which the first three cases are to model the phase change phenomenon in a shock tube, the involved fluid state inside the tube has transited from the almost pure gaseous N_2 (Section 4.1.1) to pure liquid water (Section 4.1.3). The fourth case is to simulate the strong shock appeared in typical high pressure diesel injection process. The operating condition corresponds to ECN spray A injector. While the last case is dedicated for the investigation of the cavitation phenomenon inside an expansion tube, all the performing conditions are depicted as in Table 4.1.

Table 4.1 1D test cases initial condition.

Section No.		P_L /M Pa	P_R /M Pa	T_L/K	T_R/K	$Y_{L\_N_2}$	$Y_{R\_N_2}$	ψ_L	ψ_R
4.1.1	Shock tube (1)	0.2	0.1	293	293	0.98	0.98	0.9789	0.9885
4.1.2	Shock tube (2)	0.2	0.1	353.8	337.4	0.7	0.7	0.778	0.7711
4.1.3	Shock tube (3)	0.2	0.1	293	293	5e-5	5e-5	1.3e-4	3.2e-5
4.1.4	Shock tube (4)	150	6	363	900	1e-7	0.9999999	1e-7	0.9999999
4.1.5	Expansion Tube	0.1	0.1	293	293	5e-5	5e-5	3.2e-5	3.2e-5

4.1.1 1D Subcritical Shock Tube I (H_2O-N_2)

The shock tube is 1 meter long with the initial discontinuity at 0.5m. The pressure ratio is 2 (2 bar in the left side and 1 bar in the right side) with a temperature of 293K throughout the tube. The mass fraction of N_2 and H_2O is 0.98 and 0.02 respectively. The results shown in Figure 4.1 are at the time of 1 ms. Firstly, through comparing the results of 4EQ-PR and 6EQ-PR models, no significant differences are detected between them. Particularly, the results from 6EQ-PR have shown some spurious oscillations at the interface which may be caused by the numerical instability. After refining the mesh, the spike appeared in the interface for 6EQ-PR has disappeared as shown in Figure 4.2 (e, f). It seems that 4EQ-PR has shown higher stability than 6EQ-PR in the interface. In addition, the numerical results have also been compared with the results from Chiapolino et al. [91] model in which Stiffened Gas EoS combined with a 4-Equation model has been adopted. In addition, the dissolved gas in the liquid is neglected in their model, which is referred as 4EQ-SG. One can observe in Figure 4.1 that the overall wave evolution trend has reached a qualitative agreement between the 4EQ-PR/6EQ-PR models and the 4EQ-SG model. Nevertheless, there still exists some deviations in shock front which may be caused by the distinct speed of sound predicted by SG and PR EoS. Since the phase equilibrium computation is performed in the initialization stage for the 6EQ-PR and 4EQ-PR models, this has

rendered different initial mass fraction of vaporous water with 4EQ-SG model as shown in Figure 4.1(d). Overall, the phase change behaviors induced by the expansion and compression wave are the same for the 4EQ-SG and 4EQ-PR/6EQ-PR models, thus proving the efficacy of the suggested phase equilibrium solver (Figure 4.1 (d)).

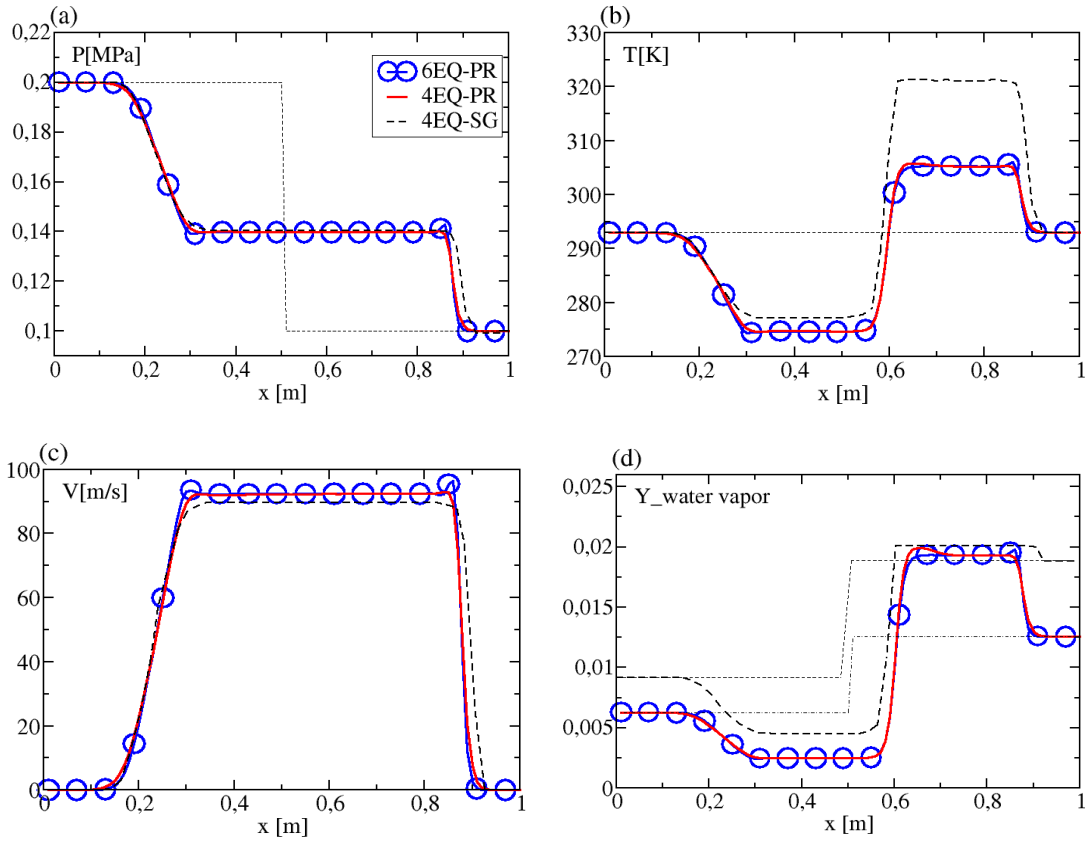

Figure 4.1 1D shock tube at time 1 ms. The computational results in Figures (a, b, c, d) (blue line: 6EQ-PR, red line: 4EQ-PR) are compared with results (bold black dashed line: 4EQ-SG) from Chiapolino et al. [91]. The computations were conducted with 100 cells. The thin dashed lines are the initial conditions.

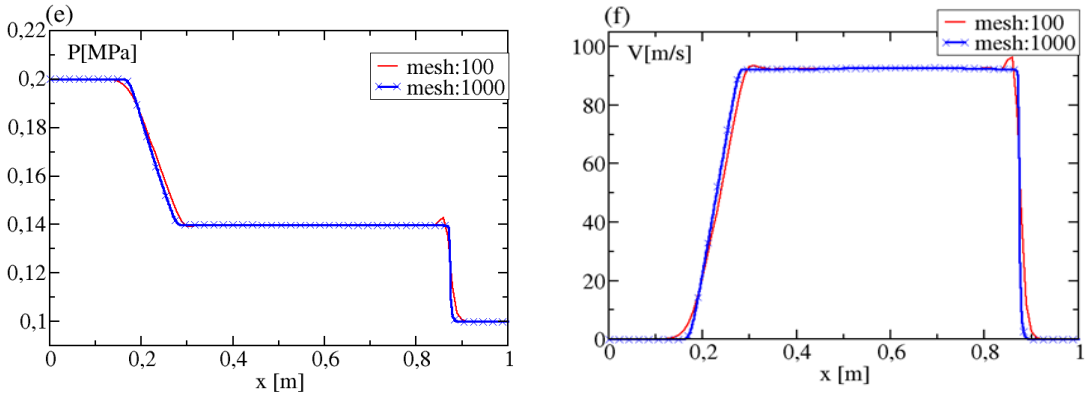

Figure 4.2 1D shock tube at time 1 ms. Figures (e, f) illustrate the results of 6EQ-PR with different mesh resolution (100 cells and 1000 cells).

4.1.2 1D Subcritical Shock Tube II (H_2O-N_2)

This test case is similar with the one in previous Section 4.1.1. The initial discontinuity is also set in the middle with a pressure ratio of 2. Moreover, the involved boundary condition and mesh have been kept the same as previous shock tube test case. But the initial mass fraction of air has been reduced from 0.98 to 0.7. Other thermal conditions like temperature and pressure are identical as the case in ref. [91]. Firstly, the results of the 4EQ-PR and 6EQ-PR models are almost coincident. No numerical oscillations and spike are detected in the interface. In terms of the comparison between different equation of state, as aforementioned, the system closed by PR-EoS, the initial vapor amount is decided by the stability test and a phase equilibrium calculation (see Section 2.3). This has explained the difference existed in the initial mass fraction of vaporous water predicted by different EoS, as depicted by the thin dashed lines in Figure 4.3 (d). Accordingly, the final amount of vaporous water also shows obvious deviations. In addition, some deviations have appeared in predicting the shock front between the 4EQ-PR and 4EQ-SG models, as illustrated in the pressure profile (Figure 4.3 (a)). This may be caused by different thermal properties predicted by the two EoS or the effect of dissolved gas part considered in

4EQ-PR/6EQ-PR models. Nevertheless, a qualitative agreement is achieved even with different EoS.

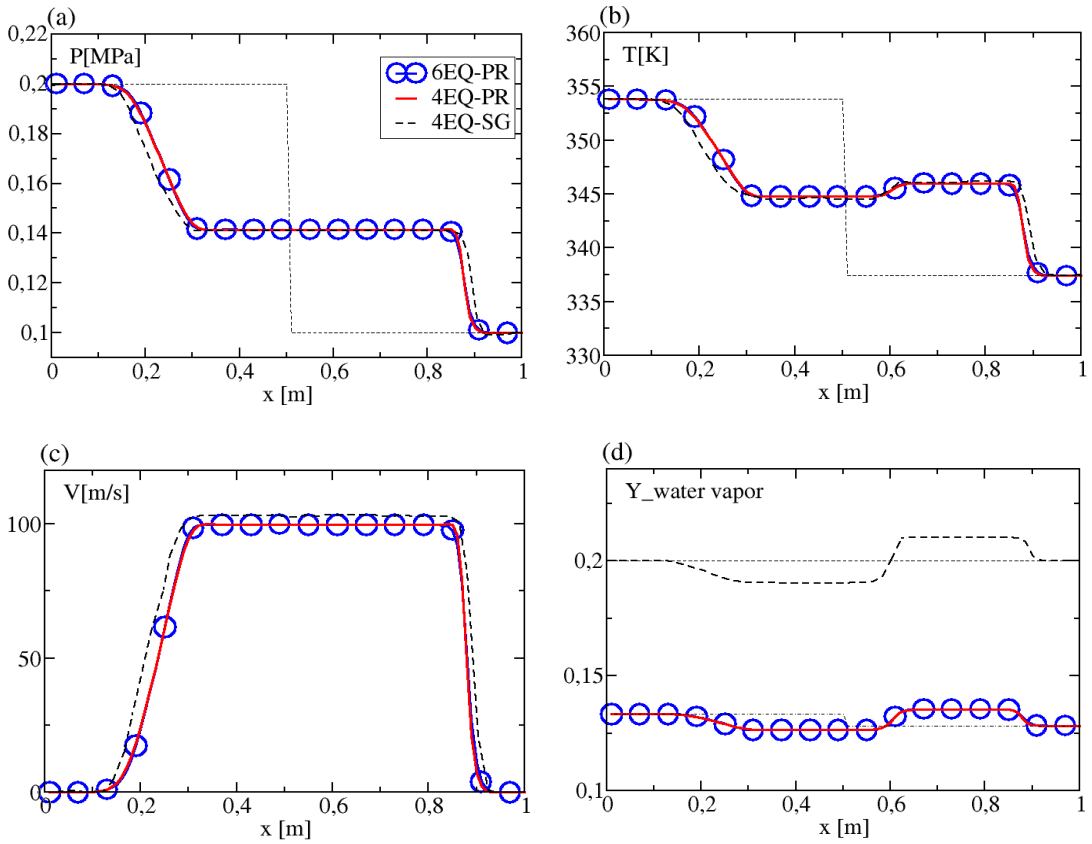

Figure 4.3 1D shock tube at an instant of 1 ms. The computational results (blue line: 6EQ-PR, red line: 4EQ-PR) are compared with results (bold black dashed line: 4EQ-SG) from Chiapolino et al. [91]. The thin dashed lines are the initial conditions. The computations were conducted with 100 cells and a CFL equalling 0.2.

4.1.3 1D Subcritical Shock Tube III (H_2O-N_2)

This test case, in contrast with previous two shock tube cases, uses an almost pure liquid phase water with an initial gas mass fraction equalling to 5E-5. The computational mesh and boundary conditions are kept the same with previous shock tube cases. After the vapor-liquid equilibrium computation, the mole fraction of vapor is around 1E-4 (in the Left side) and 3E-5 (in the Right side) (see Table 4.1). The numerical results are presented in Figure 4.4 at time 1.5 ms. Similar to the above shock tubes cases, the results from the suggested models are approximately the same.

However, more numerical diffusion is shown for 6EQ-PR model than 4EQ-PR model. The possible reason of this additional numerical diffusion may come from the additional momentum and energy equations that are computed in the case of the 6EQ-PR model. With less numerical diffusion, obvious numerical oscillations can be observed at the interface with 4EQ-PR model. Due to the relatively large liquid heat capacity, minor variations are seen from the temperature profile compared to the initial value (293K). The amount of generated vaporous water is also the same for the two flow systems.

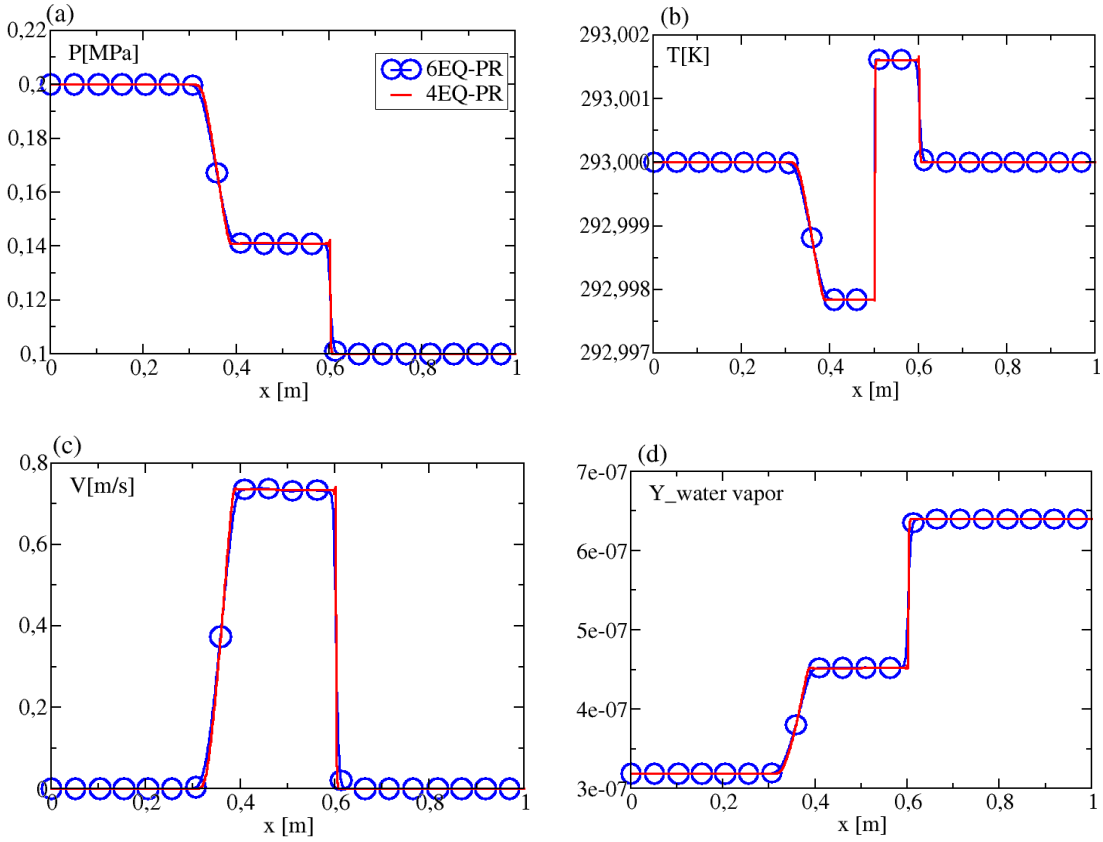

Figure 4.4 1D shock tube at the time of 1 ms. The computational results of 6EQ-PR (blue line) are compared with results from 4EQ-PR (red lines). Both computations were conducted with 100 cells and a CFL number equals to 0.2.

4.1.4 1D Transcritical Shock Tube (n-$C_{12}H_{26}$-N_2)

To further verify the capability of current model in dealing with two-phase strong shocks, the 4EQ-PR model is used to solve the 1D shock tube problem with spray A conditions. The initial discontinuity is set in the middle of the tube. In particular, the left side is filled with pure liquid n-dodecane with the initial conditions of 150 MPa, 363 K and the right side is full of high temperature nitrogen with the initial conditions of 6 MPa, 900 K. The simulation has been conducted with various mesh resolutions ranging from 1mm to 0.02 mm. The evolution of pressure, density, speed of sound and mass fraction of vaporous dodecane are presented below in Figure 4.5 (a, b, c, d). Firstly, obvious spurious oscillations are detected in the pressure profile with the mesh size of 1 mm. Whereas the oscillations are dumped significantly as the mesh is refined to 0.2 mm and further to 0.02 mm. Affected by the strong expansion wave, a prominent decrease of pressure can be found in the left part, which leads to the reduction of density and the speed of sound correspondingly, as shown in Figure 4.5 (b, c). One noting point is that no volume shift formula is adopted to adjust the density and speed of sound which may explain the relatively low-density value (~693 kg/m^3) and relatively high speed of sound (~2768 m/s) at the initial pressure of 150 MPa. The contact discontinuity is also well shaped, as depicted in the zoom of density profile Figure 4.5 (b). Since the model used here is with phase change, the evaporation wave appears between this contact discontinuity and the expansion wave, as proved by the generated vaporous dodecane in Figure 4.5 (d). In addition, due to the evaporation, a local two-phase zone is formed which indicates the decrease of speed of sound from 612 m/s at the compressed gas state to a minimum value of 253 m/s following the wood formula (Equation (3.35)), as seen in Figure 4.5 (c). At last, the effect of compression wave is displayed in the slightly elevated density and speed of sound behind the evaporation front. One noting point is that the increasing mesh resolution is not only helpful to reduce the spurious oscillations, but also favorable to improve

the accuracy of results especially in the wave front Figure 4.5 (a, b). Hence it is concluded that keeping a high mesh resolution is a crucial factor to achieve a reliable result, especially in real fluid simulation. This recommendation is generally largely respected when simulating in-nozzle and near-nozzle two-phase flow, as described in the next Section for Spray A simulations.

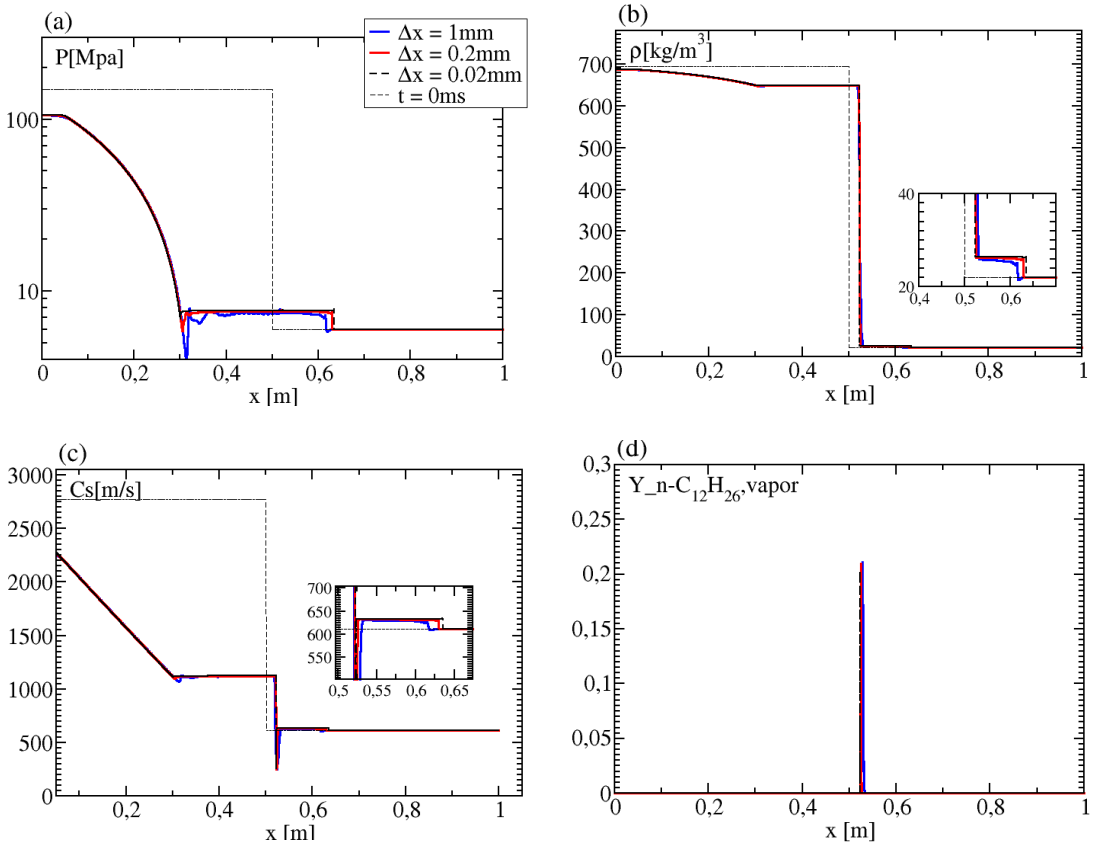

Figure 4.5 1D two-phase shock tube operated with spray A conditions ($P_{inject} = 150\ MPa,\ T_{fuel} = 363\ K,\ P_{ambient} = 6\ MPa,\ T_{ambient} = 900\ K$) using the 4EQ-PR model. (a, b, c, d) denotes the evolution of pressure, density, speed of sound and mass fraction of vaporous dodecane at an instant of 0.2 ms with a varied mesh resolution from 1 mm, 0.2 mm to 0.02 mm.

4.1.5 1D Double Expansion Tube

This test case consists of 1 m long tube filled with liquid water (H_2O) at atmospheric pressure and with the temperature 293 K. The initial mass fraction of gaseous nitrogen

(N_2) is 5e-5, and for water is 0.99995. After applying phase equilibrium computation, the initial mass fraction of vapor is around 3.2e-5. The contact discontinuity is set at the position of 0.5 m. Divided by this location, the velocity (1 m/s) in the left side is specified the same but opposite to the right side. The computational time is 3.5 ms. As shown in Figure 4.6, the profiles of pressure, temperature and velocity reach a good agreement for the proposed two models (4EQ-PR and 6EQ-PR). Similar as previous predictions in the shock tube case III, more numerical diffusion is observed for the 6EQ-PR system. The expanding width for the 6EQ-PR system is slightly wider than the one obtained using the 4EQ-PR. The possible reason may come from the different speed of sound of the 4EQ-PR and 6EQ-PR models. It is interesting to note that a small spike is detected in the temperature profile of 6EQ-PR. Affected by the temperature difference, the generated final amount of vapor has also shown obvious deviations in the middle.

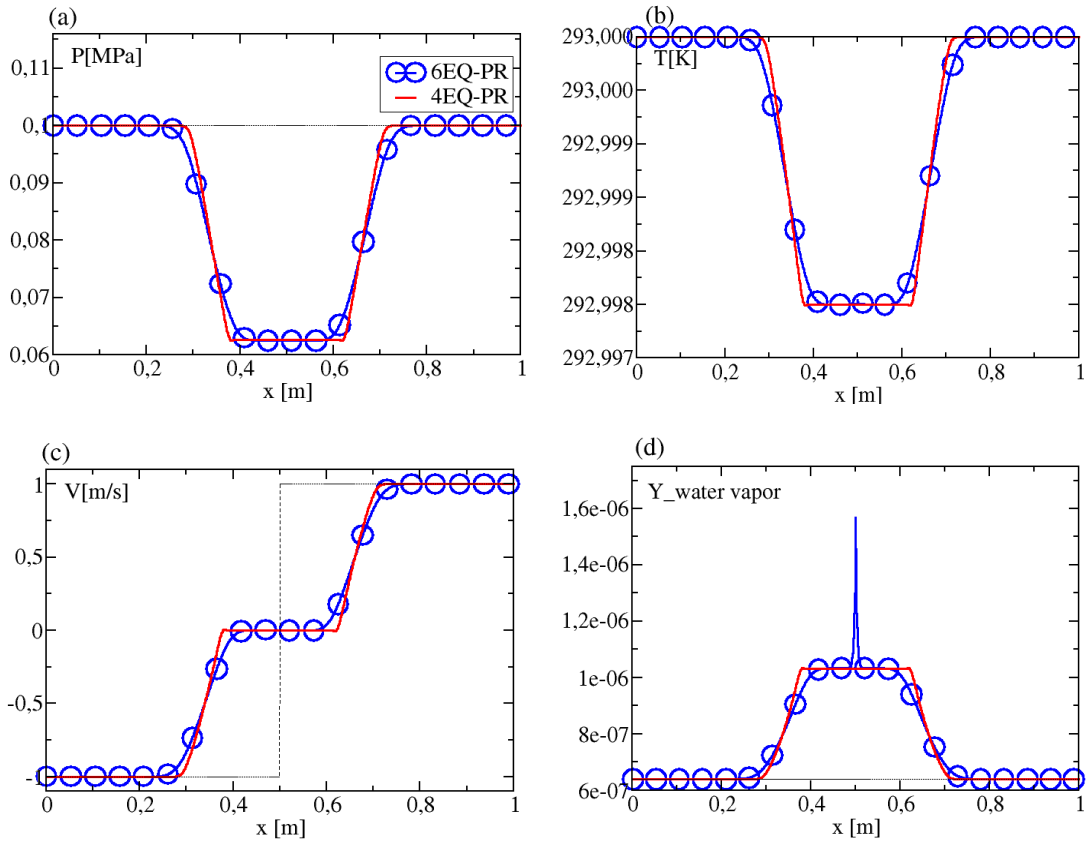

Figure 4.6 1D Double expansion tube at an instant of 3.5 ms. The computational results of 6EQ-PR (blue line) are compared with the results from 4EQ-PR (red lines). Both computations were conducted with 100 cells and a CFL number equals to 0.2.

4.2 1D modelling without phase change

In this section, the classical spurious oscillations problem will be investigated with the 4EQ-PR model. The spurious oscillations usually appear at the locations with strong contact discontinuity. Many researchers have devoted to resolving this issue [51], [98], [99]. However, this problem may deteriorate as the flow system is closed by the non-liner real-fluid EoS, such as the PR EoS. To verify this problem in current model, a series of test cases involved with large contact discontinuity have been conducted and compared with available literatures in the following sections. The binary interaction parameter between n-dodecane and nitrogen has used 0.19 based on ref. [81].

Table 4.2 Initial condition of 1D shock tube at transicritical condition

Section No.		P_l/MPa	P_r/MPa	T_l/K	T_r/K	Y_{l,N_2}	Y_{r,N_2}	$\psi_{l,v}$	$\psi_{r,v}$
4.2.1	Shock tube Transcritical (N_2)	60	6	158	222	0.999999	0.999999	1E-7	0.999999

4.2.1 1D Transcritical Shock Tube (Pure N_2)

In this test case, a transcritical shock tube problem is simulated. The numerical results from the 4EQ-PR are compared with the reference results from Ma et al. [51], in which a fully conservative solver combined with PR EoS has been developed without considering phase change. The computational domain and boundary condition are the same as previous subcritical shock tube cases. The initial discontinuity lies in the middle of the tube. Initial physical conditions can be found in Table 4.2. This is a single component case (an almost pure nitrogen case, $Y_{N_2} = 1 - 1E - 6$). In addition, since the pressure and temperature are above the critical point of nitrogen for both sides, the fluid is therefore in supercritical state. For the sake of stability and accuracy, the CFL number is set to 0.1. As depicted in Figure 4.7, the 4EQ-PR model has obtained exactly the same results as Ma et al. [51]. The excellent agreement prove that the current 4EQ-PR model can predict the shock wave evolution correctly even with a quasi-conservative formulation for the energy balance (Section 3.3). Last but most importantly, there are no spurious oscillations neither serious numerical diffusion at the interface (i.e. contact discontinuity). Actually, in the work of Ma et al. [51], an entropy-stable model has been added in the simulation to dump the spurious oscillations. However, in current work, no such model is needed to obtain accurate results. Indeed, since no serious convergence problem is met while dealing with

transcritical problem, developing of such entropy-stable model will not be considered in this thesis.

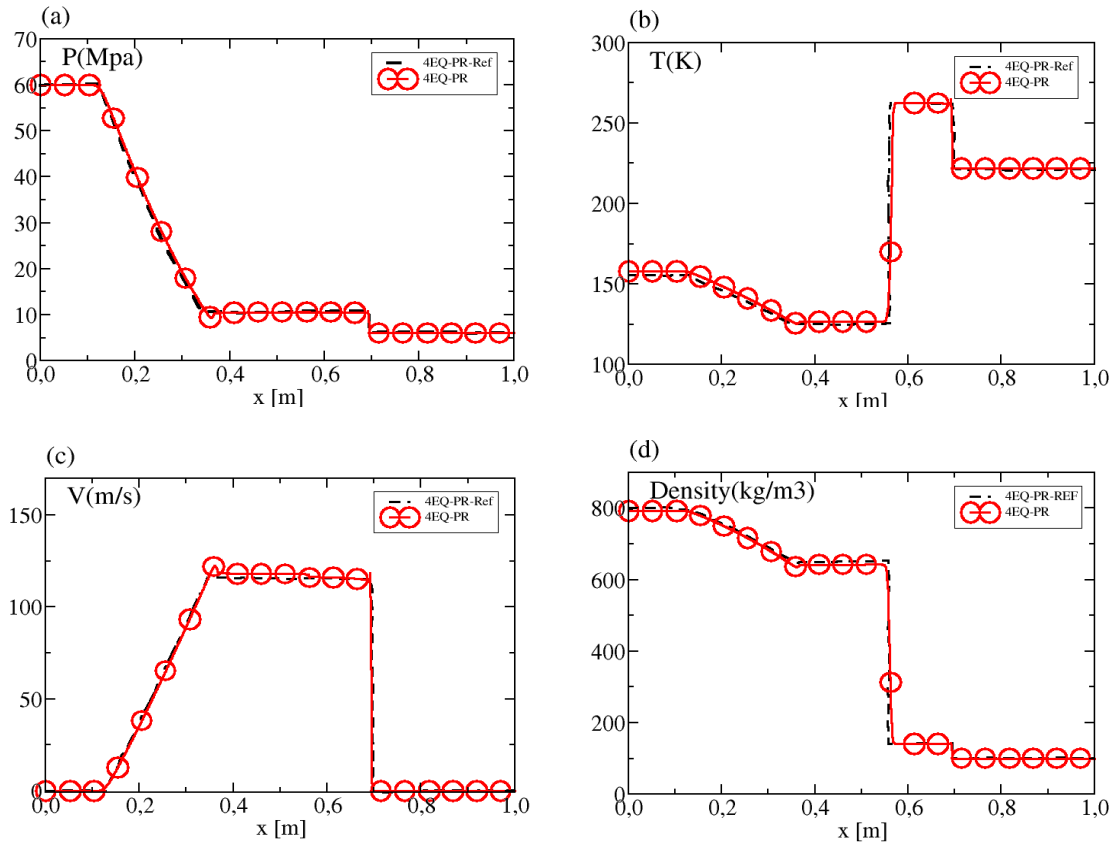

Figure 4.7 1D transcritical shock tube at an instant of 0.05 ms. The computational results (solid line with symbols) are compared with results from Ma. [51] (dashed bold line). The present work computations were conducted with 1000 cells and a CFL number equaling 0.1. The reference results are done with 50000 grid points.

4.2.2 1D Advection Tube

In this section, the classical 1D advection tube is tested using different thermodynamic conditions varying from subcritical to supercritical states including the transcritical flow regime. The initial liquid zone is located between 0.25 m and 0.75 m. Different mesh resolutions have been used for each condition. The working fluid is a mixture of n-dodecane ($C_{12}H_{26}$) and nitrogen (N_2) for case 1 and pure dodecane for the rest of the last three cases, as depicted in Table 4.3. The first case is

conducted at low temperature and pressure with subcritical state and the whole system is initially at two-phase state. The other three cases are performed with high temperature and a constant pressure of 60 bar which is above the critical value of $C_{12}H_{26}$ (18.1bar), the initial fluid state is varied based on different thermal conditions. As the temperature has changed from subcritical values (300 K and 500 K) to supercritical values (900 K and 1200 K) (see Table 4.3), the fluid has transformed from a pure liquid-like state to a dense gas-like state. Detailed descriptions will be addressed later.

Table 4.3 Initial conditions for 1D advection tube.

Case No.	Advection tube	P_{liqzon} /MPa	P_{gaszon} /MPa	T_{liqzon} /K	T_{gaszon} /K	$Y_{liqzone\_c_{12}}$	$Y_{gaszone\_c}$	V/(m/s)
1	Subcritical	0.1	0.1	300	300	0.99	0.01	100
2	Subcritical	6	6	300	500	1	1	100
3	Transcritical	6	6	500	900	1	1	100
4	Supercritical	6	6	900	1200	1	1	100

I. Results of case1

In this test case, the initial contact discontinuity separates the different material in the two sides. Since liquid zone is filled with $C_{12}H_{26}$ and gas zone is filled with N_2, this has resulted in an obvious gradient in the density (Figure 4.8 (d)). Two different mesh resolutions are used (1000 and 2000 cells). The results presented in Figure 4.8 are at time 10 ms and a full cycle is realized using periodic boundary conditions. The oscillations amplitude has been quantified through computing the error variation relatively to the exact solution depicted by the dashed line in Figure 4.8 (d). The relative errors of pressure, temperature and velocity are shown in Figure 4.8 (a, b, c). To be more specific, much evident oscillations are detected for the results computed with 1000 cells. Whereas, the oscillation amplitude for all plotted variables are less

than 0.3%, they can be reduced significantly as the mesh is refined. As for the numerical diffusion, refined mesh can relatively sustain sharper interface than the rough one. Overall, no serious numerical diffusion and oscillations are detected in the current subcritical and low thermal condition (case 1). To furtherly verify this problem, more test cases with harsher thermal conditions are conducted in the following section.

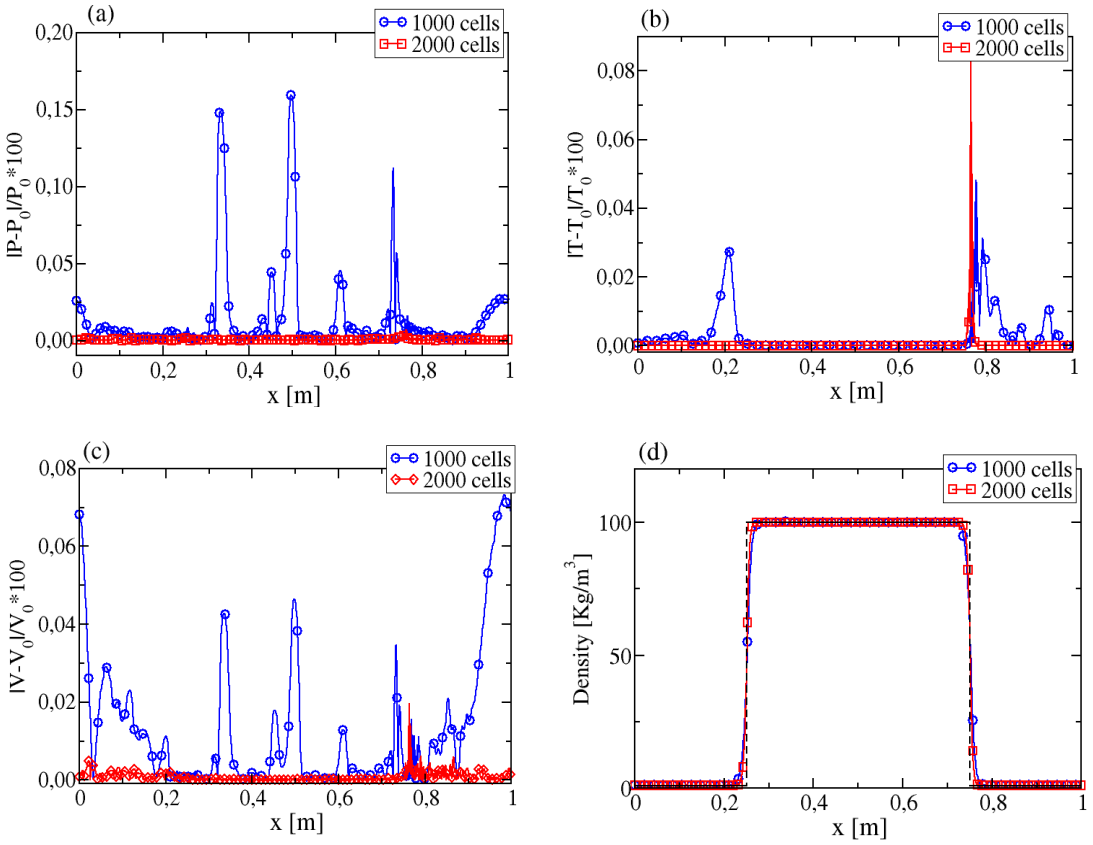

Figure 4.8 1D advection tube at time 10 ms. The relative errors of pressure, temperature and velocity compared with initial value are illustrated at (a, b, c) respectively. The comparison of density at an instant of 10 ms and 0 ms is plotted in figure (d). The computations were conducted with 1000 cells and 2000 cells and a CFL number equaling 0.1.

Since the energy is not fully conserved in the 4EQ-PR model, it necessities to check the loss of energy during simulations. The relative error of total energy and mass are shown in Figure 4.9 at time 10 ms. It is shown that the percentage of energy and mass

loss is less than 0.001% even for the rough mesh. With refined mesh, the energy loss is close to zero. Hence it is concluded the non-conservative energy equation will not seriously affect the overall flow development especially when the mesh is sufficiently refined.

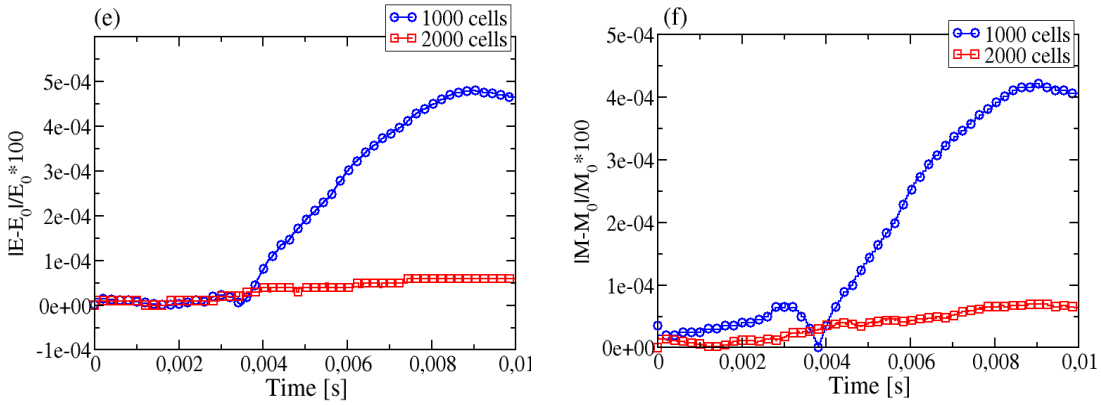

Figure 4.9 The percentage of energy and mass variation related with initial time in the 10 ms. The computations were conducted with 1000 cells and 2000 cells and a CFL number equaling 0.1.

II. Results of cases 2, 3 and 4

To furtherly clarify the related thermodynamics schemes for the last three single-component cases in Table 4.3, Figure 4.10 has illustrated the evolution of the n-dodecane density and specific heat capacity compared with NIST data [100]. It is well known that using PR-EoS, heat capacity at constant pressure can gain a better agreement with NIST data than the density. As the temperature evolves below the n-dodecane critical point (658K), such as in case 2, the thermodynamics path belongs to the subcritical state. In these conditions, thermal properties have went through a smooth and monotone variation as shown in Figure 4.10. However, while the temperature varies from a subcritical temperature 500K to a supercritical temperature 900K (such as in case 3, usually called as a transcritical flow), a non-linear variation near the critical point can be detected in the profile of heat capacity. For such transcritical path, a much steeper decrease of density is also observed compared with

purely subcritical conditions. In addition, as temperature is climbing to the critical point, the thermodynamics state evolves to supercritical through a pseudo-boiling region where liquid and vapor are difficult to be distinguished. Thus, the case 4 belongs to the purely supercritical regime in which the thermal properties are evolving with smaller gradients, as shown in Figure 4.10 when the temperature is greater than 900K.

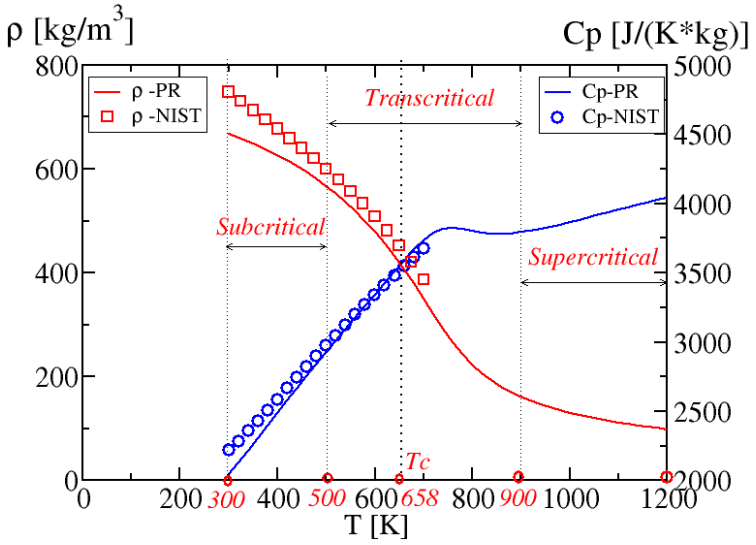

Figure 4.10 Comparisons of heat capacity at constant pressure and density between PR EoS and NIST in a temperature range of 300-1200K and at constant pressure of 60 bar. Illustration of different thermodynamics schemes for the three cases in Table 4.3.

All three test cases 2, 3 and 4 were run for 5 ms and two different mesh resolutions are tested. Similar to previous advection test case, only the percentage of relative deviations of pressure, velocity and total energy are illustrated in Figure 4.11, Figure 4.12 and Figure 4.13.

Firstly, in the subcritical case 2 condition (Figure 4.11), the maximum value of pressure oscillations can reach 10% which is much higher than in case 1 (~0.3%). This implies the discontinuity caused by the temperature gradient has more effect on the oscillation problems than the material gradient. However, the magnitude of the velocity error is much smaller. After refining the mesh from 1000 to 10000 cells, the

error of pressure can reduce significantly and is smaller than 5%. No serious numerical diffusion and oscillations are detected in the density profile. The energy loss is also negligible in the whole computation time scale (Figure 4.11(d)). In contrast, in the transcritical case 3 condition (Figure 4.12), the oscillation errors of pressure can reach 15%, slightly higher than the subcritical case 2 which can be explained by the nonlinear and much steeper variation of the thermal properties in the transcritical path, as explain above based on Figure 4.10. Correspondingly, the velocity variation range (~10%) is also much larger than previous case 2 (<5%). Energy loss percentage are approaching 0.03% with the rough mesh resolution and 0.005% with refined mesh. These results again confirm the conclusion that enhancing mesh refinement can not only control the spurious oscillations, but also, improve mass and energy conservation. Finally, much smaller oscillation errors are found in supercritical condition (case 4), as shown in Figure 4.13. The error amplitudes for pressure and velocity are both less than 0.5% which are attributed to the moderate gradients of the thermal properties compared with subcritical (case 2) and transcritical (case3) paths (Figure 4.10). In addition, the energy loss is smaller than 0.0001% for the pure supercritical path. A remarkable point related with current 4EQ-PR model is that no serious numerical diffusion is detected at the interface, as shown in the profiles of density (Figure 4.11 (c), Figure 4.12 (c), Figure 4.13 (c)).

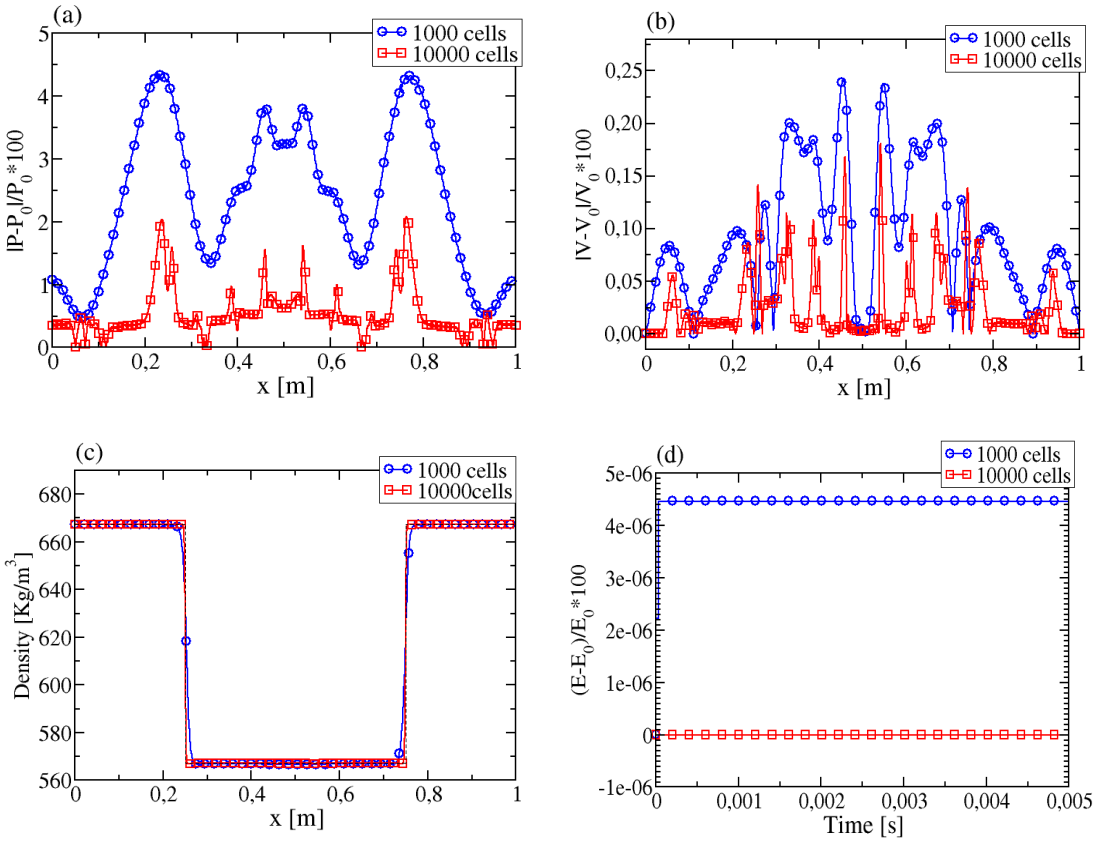

Figure 4.11 Case 2 results: Results of 1D advection tube with subcritical condition at an instant of 5 ms. The relative error of pressure and velocity compared with initial value are illustrated at (a, b) respectively. The comparison of density at an instant of 5 ms and the initial time is plotted in Figure (c). The percentage of energy variation during the 5 ms is plotted in Figure (d). The computations were conducted with 1000 cells and 10000 cells and a CFL number equaling 0.1.

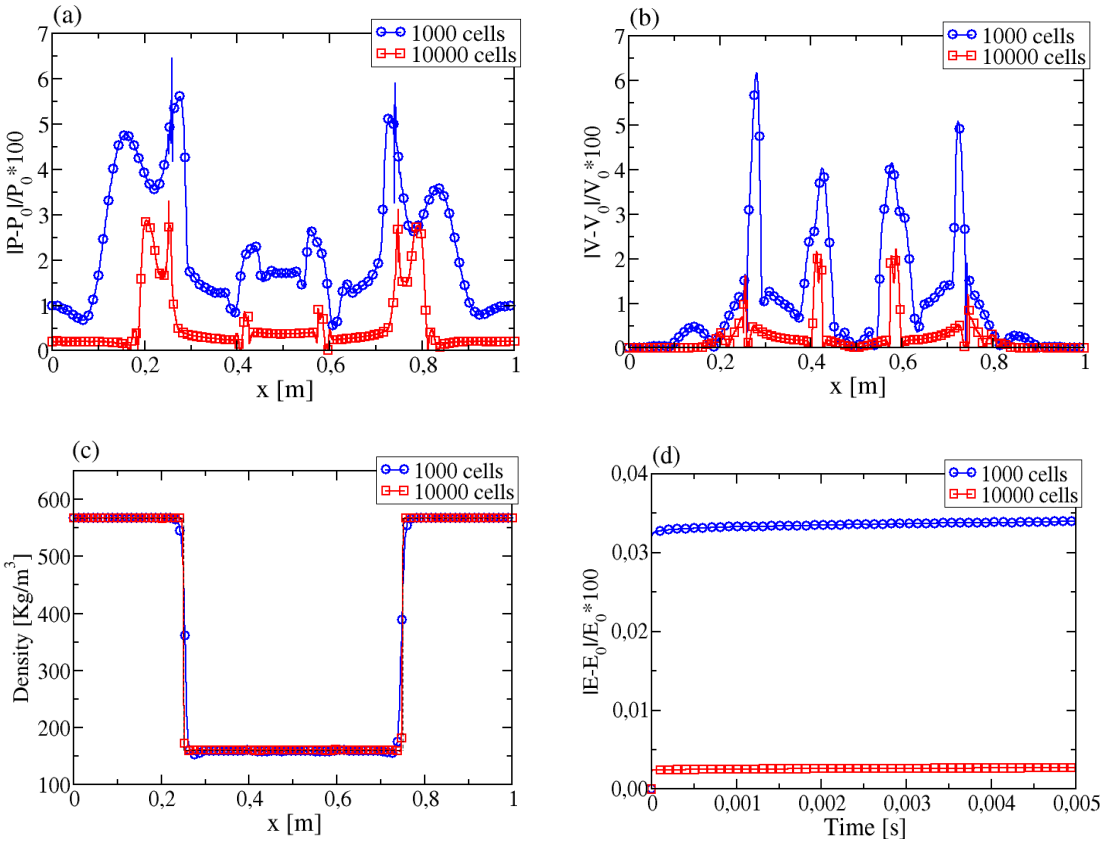

Figure 4.12 Case 3 results: Results of 1D advection tube with transcritical condition at an instant of 5 ms. The relative error of pressure and velocity compared with initial value are illustrated at (a, b) respectively. The comparison of density at an instant of 5 ms and the initial time is plotted in Figure (c). The percentage of energy variation during the 5 ms is plotted in Figure (d). The computations were conducted with 1000 cells and 10000 cells and a CFL number equaling 0.1.

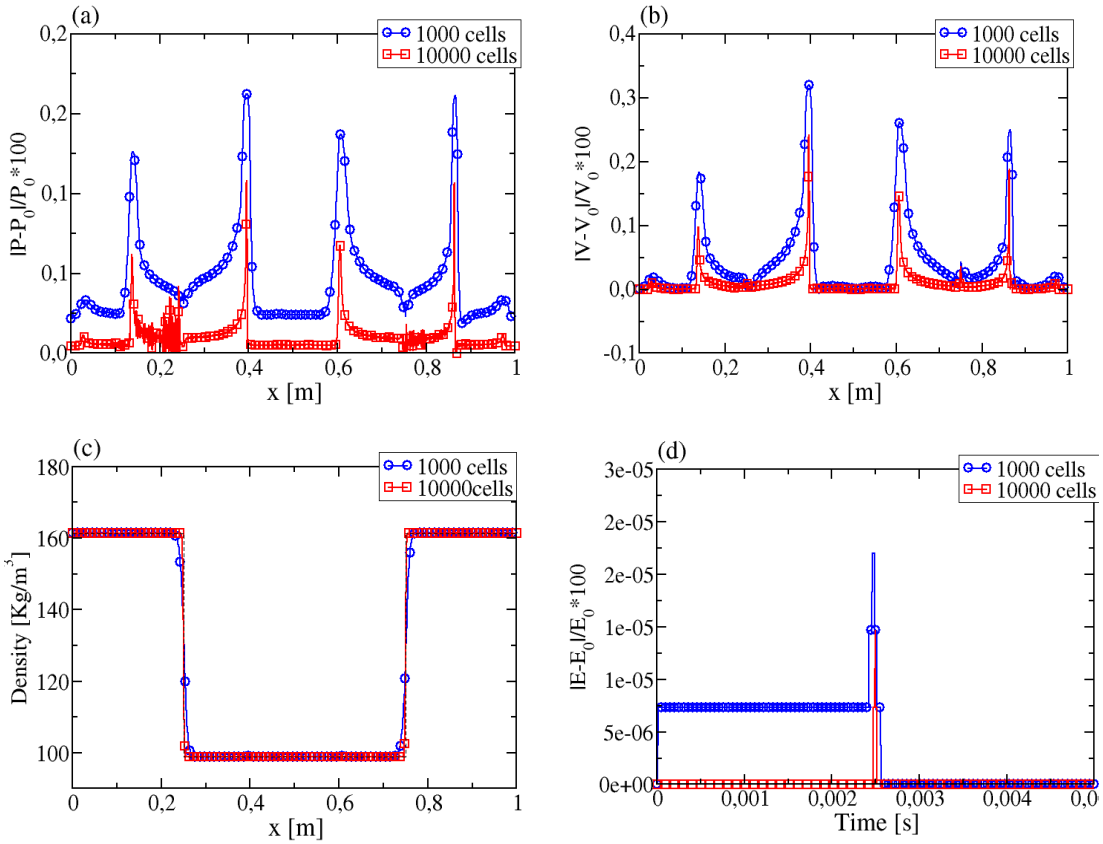

Figure 4.13 Case 4 results: Results of 1D advection tube with supercritical condition at an instant of 5 ms. The relative error of pressure and velocity compared with initial value are illustrated at (a, b) respectively. The comparison of density at an instant of 5 ms and the initial time is plotted in Figure (c). The percentage of energy deviations during the 5 ms is plotted in Figure (d). The computations were conducted with 1000 cells and 10000 cells and a CFL number equaling 0.1.

4.3 Chapter Conclusion

In this Chapter, a series of 1D test cases involving shock tube, cavitation, advection problems have been simulated and the results have been compared with numerical results available in the literatures. Several conclusions can be drawn from these academic comparisons:

1) Since 4EQ-PR and 6EQ-PR have employed the same phase equilibrium model, minor deviations have been presented between these two models.
2) A qualitative agreement has been obtained through the comparisons with the 4EQ-SG model, from ref. [91] in the results of the shock tube.
3) The modeling results of transcritical shock tube (section 4.2.1) have gained a perfect agreement with academic results from a fully conservative model [51]. The non-conservative energy in current flow system has not affected the results.
4) The spurious oscillations problem and conservative characteristic have been also discussed. The spurious oscillations can be reduced significantly by mesh refinement. No extra numerical scheme is added in the solver to dump the oscillations and the current flow system can compute the above cases smoothly. It seems that the non-conservative characteristics of energy equation can dump the osillations compared to fully conservative scheme. Moreover, refining the mesh can enhance the accuracy of simulation results.
5) Though current 4EQ-PR model has not guaranteed the fully conservative energy, the total energy loss in the computation time span is negligible (see 4.2.2) which will not affect the accuracy of the flow significantly.
6) In the simulations of 1D advection tube (section 4.2.2), current model (4EQ-PR) has presented some advantages in sustaining the sharpness of interface. In other words, no serious numerical diffusion problem shows up even after long advection time.

7) Lastly, higher computational efficiency and stability has been found for 4EQ-PR model than 6EQ-PR model. In the following 3D test cases validations, 4EQ-PR will be utilized instead of 6RQ-PR.

5 Cavitation Modelling

In this section, the developed phase equilibrium model has been applied to a real cavitating nozzle. Firstly, a comprehensive thermodynamics analysis about the effect of dissolved N_2 on phase change and saturation pressure is conducted. Then the cavitation phenomenon in a real size 2D nozzle is simulated with 6EQ-PR model. Finally, the 4EQ-PR model is utilized to model the 3D nozzle configuration and the results obtained with different initial amounts of dissolved Nitrogen have been compared to available experimental results.

5.1 Effect of N_2 on phase change and saturation pressure

The fuel used for all the cavitation modelling in this chapter is gasoline calibrated fluid (Viscor 16BR) with the properties similar to decane [101]. Since the real fluid EoS is employed, the involved input parameters like critical points and acentric factor have referred to the properties of decane. The involved non-condensable gas is N_2. Firstly, the phase equilibrium analysis about Viscor and N_2 system is presented. Then the effect of N_2 on fluid saturation pressure is discussed. To investigate the thermodynamic equilibrium behaviour of Viscor and N_2 system, the main method utilized at given temperature and pressure is isothermal flash computation (TP flash), as stated in Section 2.3. An important variable in thermodynamics to represent generated vapor at phase equilibrium calculation is the vapor mole fraction, psi (Ψ_v). This parameter represents the overall amount of vapor which contains the vaporized fuel and gaseous N_2. Figure 5.1 (a) illustrates the evolution of vapor molar fraction with the amount of N_2 at the pressure range from 1bar to 10 bar. It is obvious to find that the Ψ_v has increased as more gaseous N_2 is added in the feed. This means that compressed fuels originally containing a high amount of N_2 will promote (gaseous) cavitation appearance (or homogeneous nucleation) in low pressure regions. Some researcher has validated this phenomenon with experiments [102], in which they have

attributed the strengthening of cavitation to the intensifying of cavitating nuclei coming from the dissolved gas, and the dissolved gas nuclei can help decrease the energy needed to form a bubble or say reduce the tensile strength of fluid. One noting point is that at each pressure, there exists a transition point where the Ψ_v changing from the negative value to positive one which actually denotes the gas has transformed from the dissolved state to free gas bubble. To some extent, this may imply the initial formation of a nuclei. The negative vapor fraction implies no vapor is generated in the flow and the trifle amount of nitrogen has fully dissolved inside the liquid phase. In other words, the fluid is in single liquid phase until a certain mole fraction of N_2 is reached depending on the pressure and temperature conditions. Meanwhile, the phase state has been through the transition from pure liquid to two-phase. In addition, with higher pressure, the N_2 concentration needed for phase transition (or nucleation) also increases notably which proves that high pressure can dissolve more N_2. The exponential growth trend of molar fraction in the liquid phase (dissolved N_2) with pressure is shown in Figure 5.1 (b).

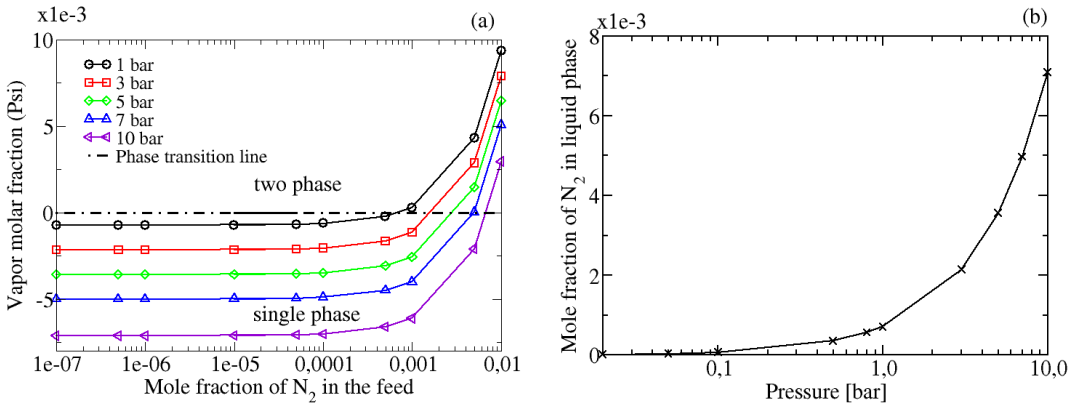

Figure 5.1 (a) The variation of vapor mole fraction with the feed of N_2 at T = 293 K; P = 1-10 bar. (b) denotes the amount of dissolved N_2 at the pressure range of 0.01-10 bar

It is well-known that cavitation appears as the pressure drops to the saturation value. Thus, saturation pressure is an important index to indicate the inception of cavitation. Figure 5.2 has illustrated the evolution of saturation pressure with temperature for

n-dodecane and Viscor fuels at different N_2 concentrations. The saturation pressure of pure n-dodecane computed with PR EoS has been compared to the reference data from NIST (Figure 5.2 (Left)). As can be seen in this Figure, a good agreement has been achieved at the temperature range of 293K-670K. The saturated pressure of the mixture system is very close to the pure component value as the N_2 concentration is close to 2E-7. However, obvious deviations can be detected as the mass fraction of N_2 is increased to 2E-6. These deviations are much larger at low temperature (~300K) compared to the high temperature (>500K). The saturation pressure has increased significantly as the N_2 concentration keeps increasing from 2E-7 to 2E-3. This trend has also been found in the gasoline surrogate Viscor (Figure 5.2 (Right)). Minor differences are found for the saturation pressure as the N_2 concentration is between 2E-6 and 2E-7 for Viscor. Since the higher saturation pressure corresponds to larger N_2 concentration, this will facilitate the inception of cavitation as testified in the following 3D simulation.

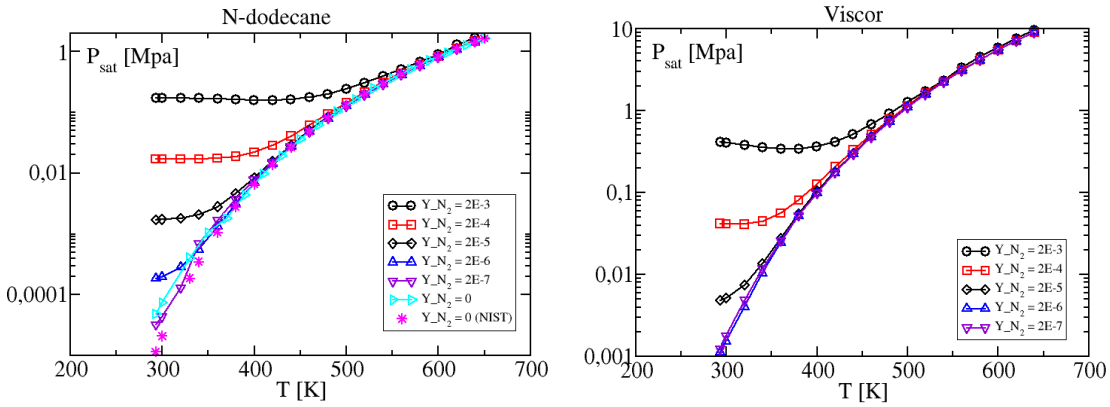

Figure 5.2 Evolution of saturation pressure(bubble pressure) with varying N_2 concentration Y_{N_2}={0, 2E-3, 2E-4, 2E-5, 2E-6, 2E-7} for n-$C_{12}H_{26}$-N_2 (Left) and Viscor-N_2 (Right) systems at a temperature range of 293 K-670 K.

5.2 Numerical setup

In this section, the developed two-phase flow models (4EQ-PR and 6EQ-PR) have been employed to investigate the cavitation phenomenon in a real-size nozzle. The detailed numerical parameters are summarized in Table 5.1.

Table 5.1 Numerical parameters for the cavitation simulations.

Fluid models	6EQ-PR (two fluids model) 4EQ-PR (homogeneous fluid model)
Cavitation model	Real fluid multicomponent phase equilibrium model
Initial N_2 feed	2E-3 (6EQ-PR); 2E-5, 2E-6 (4EQ-PR)
Compressibility	Fully compressible for both phases
Turbulence model	Large Eddy Simulation, sub-grid scale model: Smagorinsky
Grid type	Hexahedral
Time integration precision	First order
Spatial discretization	Second order
Time step	2E-10 - 4E-10
Initial conditions	Liquid at T = 293K, P = 0.1MPa

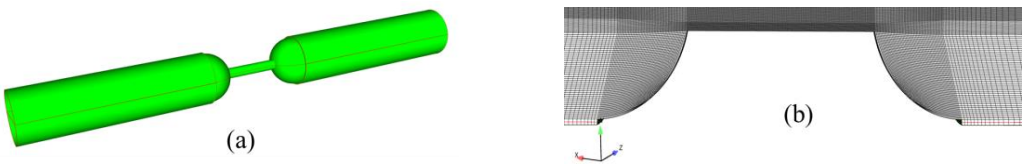

Figure 5.3 (a) Configuration of 3D geometry. (b) Illustration of mesh distribution in one clip plane.

The configuration of the nozzle is shown in Figure 5.3 (a). The cavitating nozzle used here is axisymmetric with sharp inlet edge and a diameter of 500 μm and a length of 2.5 mm. More descriptions can be found in [101], [103]. Due to the computational

efficiency issue, $1/8$ of the original geometry configuration is simulated using the 6EQ-PR model, as shown in Figure 5.4. The mesh is refined around the orifice zone and the minimum resolution of grid reaches 6 μm and the total cell number counts 25982. However, half geometry is simulated with 4EQ-PR model, as depicted in Figure 5.5 in order to be able to compare the numerical results with the radiography experiments [101], [104]. There are around 64 cells across the orifice diameter which corresponds to the average size of 7.84 μm for each cell. The total cell number counts 25982. Similar to the 2D-sector configuration, the more refined region is distributed inside the orifice and the inlet, outlet regions as shown in Figure 5.5.

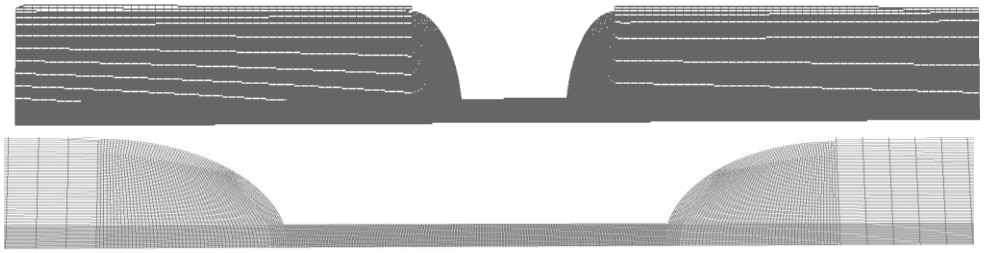

Figure 5.4 Configuration of $1/8$ geometry and mesh refining zone with total 25982 cells and minimum grid resolution of 6.06 μm.

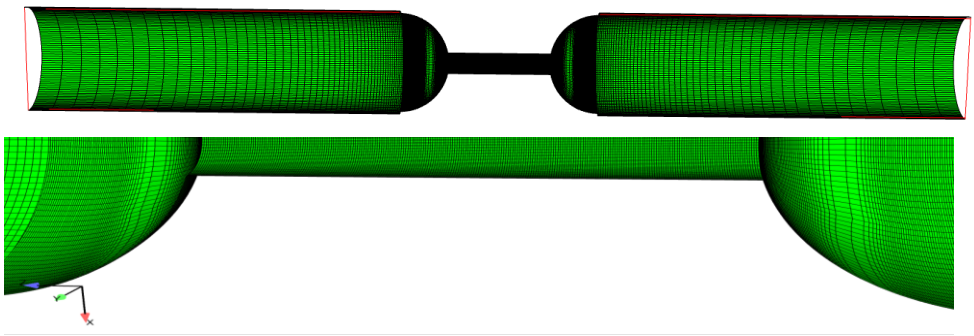

Figure 5.5 Configuration of $1/2$ geometry and mesh refining zone with 560425 total cells number and minimum grid resolution of 5 μm.

Since the original experiments are performed in the submerged conditions [101], [104] the modelling process also assumes the nozzle to be full of liquid at the beginning. The inlet and outlet are set with pressure boundary conditions with the 10 bar and 1

bar, respectively, the same as the experiments [101], [104]. All the modellings of cavitation are conducted with the finite volume strategy within the large eddy simulation framework. The adopted sub-grid scale model is the Smagorinsky model. As mentioned in Section 3.4.1, the time-splitting method is adopted to resolve the parabolic and hyperbolic parts in IFP-C3D [55]. The time-splitting begins with an implicit Lagrangian stage, then followed by a sub-cycled explicit Eulerian stage. In the Lagrangian stage, a second order implicit differencing is used for parabolic terms. The coupled implicit equations (velocity, pressure and temperature) are solved by SIMPLE algorithm. Then, the obtained solutions are updated by solving the hyperbolic part in the Eulerian stage using a quasi-second-order-upwind (QSOU) explicit numerical scheme. The time step is controlled by the Courant-Friedrichs-Lewy (CFL) number of 0.1 for the consideration of numerical stability.

In addition, in the original experiments, the tested conditions have contained the degassed and non-degassed conditions. Since no exact quantified amount of N_2 is identified in the fluid during experiments, it is essential to determine a critical value to differentiate the non-degassed situation from degassed state, for the convenience of modeling. As shown in Figure 5.1(a), the fluid state has transformed from single liquid state to two-phase saturation state with the increase of N_2 in the fluid mixture. As the fluid is still in pure liquid state, the trifle N_2 is fully dissolved in the fluid, in which the filling N_2 in the feed is exactly the same as the amount of dissolved N_2. Since the time scale to reach saturation state is very long, the study here has mainly focused on the non-saturated fluid mixture. Two initial values for N_2 concentrations Y_{N_2} = (2E-5, 2e-6) are selected to represent the non-degassed and degassed state respectively, as listed in Table 5.2. The amount of N_2 in the non-degassed state is the same as the work of Battistoni [30]. However, since the involved N_2 is situated in the dissolved state instead of free non-condensable gas, the N_2 concentration in the degassed state set with 2E-6 is slightly higher than in the work of Battistoni (2E-7)

[30]. As a contrast, a saturated initial state with higher initial mass fraction of 2E-3 is also simulated with 6EQ-PR.

Table 5.2 Initial conditions for the cavitation simulations

Feed(Y_{N_2})	Vapor fraction (Ψ_v)	Initial fluid state	Initial dissolved N_2 (Y_{N_2})	Gas volume fraction (α_g)	Adopted Model
1E-3	1 E-3	Two-phase	2 E-3	1 E-2	6EQ-PR
2 E-5	1 E-6	Liquid phase	2 E-5	1 E-6	4EQ-PR
2 E-6	1 E-6	Liquid phase	2 E-6	1 E-6	4EQ-PR

$*\ Y$ denotes mass fraction

5.3 2D Cavitation Modelling with 6EQ-PR

In this section, the suggested 6EQ-PR model has been used to simulate the cavitation phenomenon in a real size 2D-sector nozzle. During simulation, the initial pressure for the overall flow field has been set the same as the inlet pressure (10 bar). In addition, the fluid is assumed in two-phase equilibrium state with an initial volume fraction of gas 1E-2, corresponding to a mass fraction of N_2 around 2E-3 (Table 5.2). The aim of this study is to carry out a preliminary cavitation simulation in order to highlight and identify the effect of the initial non-dissolved nitrogen gas on the cavitation process and to check the consistency with previously known-physics.

The modelling results shown below in Figure 5.6 are at t = 1.4 ms. As seen from the void fraction distribution , the cavitation appeared in the corner sharp edge as expected. But, the amount of cavitation near the wall seems underestimated due to the relatively high value of initial nitrogen mass fraction (1E-3). It is well known that the occurrence of cavitation is closely related with the decrease of pressure. A parameter named $Delta\_P$ is defined here to express the variation ratio of pressure related to the initial inlet pressure 10bar ($Delta\_P = \frac{(10\ \text{bar} - \text{P})}{10\ \text{bar}}$). As shown in Figure 5.7 (a), the

highest Delta_P in the inlet corner has corresponded to the maximum value of gas volume fraction where evaporation appears most .However, the contribution of void is from the non-condensable N_2 in addition to vaporous fuel, as shown in Figure 5.6 (b). To clarify the mutual effect of gaseous cavitation and vaporous cavitation, Figure 5.7 (b) has demonstrated the evolution of molar fraction of fuel and nitrogen with $Delta\_P$ in the near wall axis. The rapid decrease of pressure has induced faster formation of fuel vapor than nitrogen (Figure 5.7 (b)). This process implies it is the vaporous cavitation that dominate during fast pressure decrease. And gaseous cavitation appears mostly in the liquid bulk near the hole axis due to a lower $Delta\_P$ gradient (i.e. slower pressure decrease), as shown in Figure 5.7 (a). In addition, these two kinds of cavitation are mutually restricted. To further confirm this phenomenon, the developing process of cavitation on the inlet corner has been remodeled with phase equilibrium solver. The molar fraction of nitrogen is set the same with the initial value 8.08 E-3 considering the relatively low velocity on the wall. As seen in Figure 5.7 (c), with the pressure decreasing down to 0.5 bar, the evaporation ratio of fuel becomes extremely faster which further proves the vaporous cavitation is sensitive to the fast pressure drop. In addition, dissolved nitrogen concentration also becomes higher with pressure increasing (Figure 5.7 (c)). However, this Figure also show that increasing dissolved gas has also seen the reduction of molar fraction of vaporous fuel . This may imply that the dissolved gas is favorable to the formation of gaseous cavitation instead of the vaporous cavitation. Finally, one can concludes that gaseous cavitation plays a dominant role in total cavitation if the fluid mixture contains a high initial molar fraction of non-condensable gas. The influence of dissolved gas on the density and heat capacity have also been shown in Figure 5.7 (e, f). Overall, the liquid density has not been through significant variation with the addition of dissolved gas, at current pressure and temperature. In contrast, heat capacity of the liquid has seen a clear change especially near the wall face.

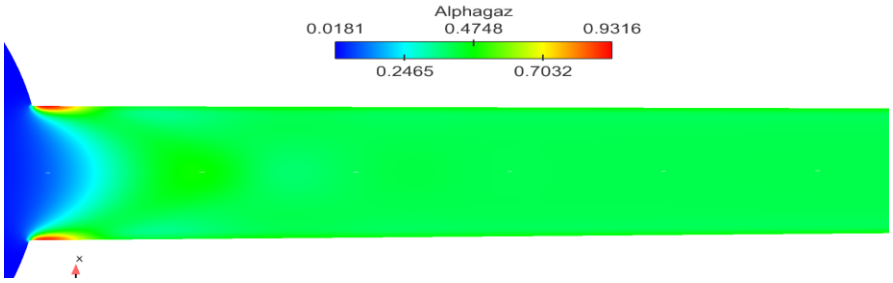

(a)

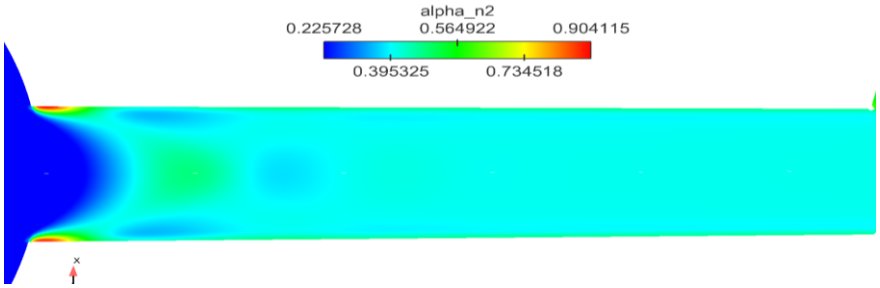

(b)

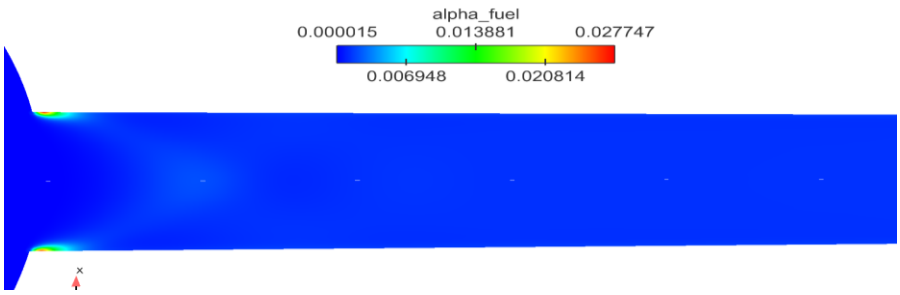

(c)

Figure 5.6 Results of the 2D cavitating nozzle. Alpha stand for volume fraction. Here fuel is Viscor and gas inludes Nitrogen in addition to Viscor vapor.

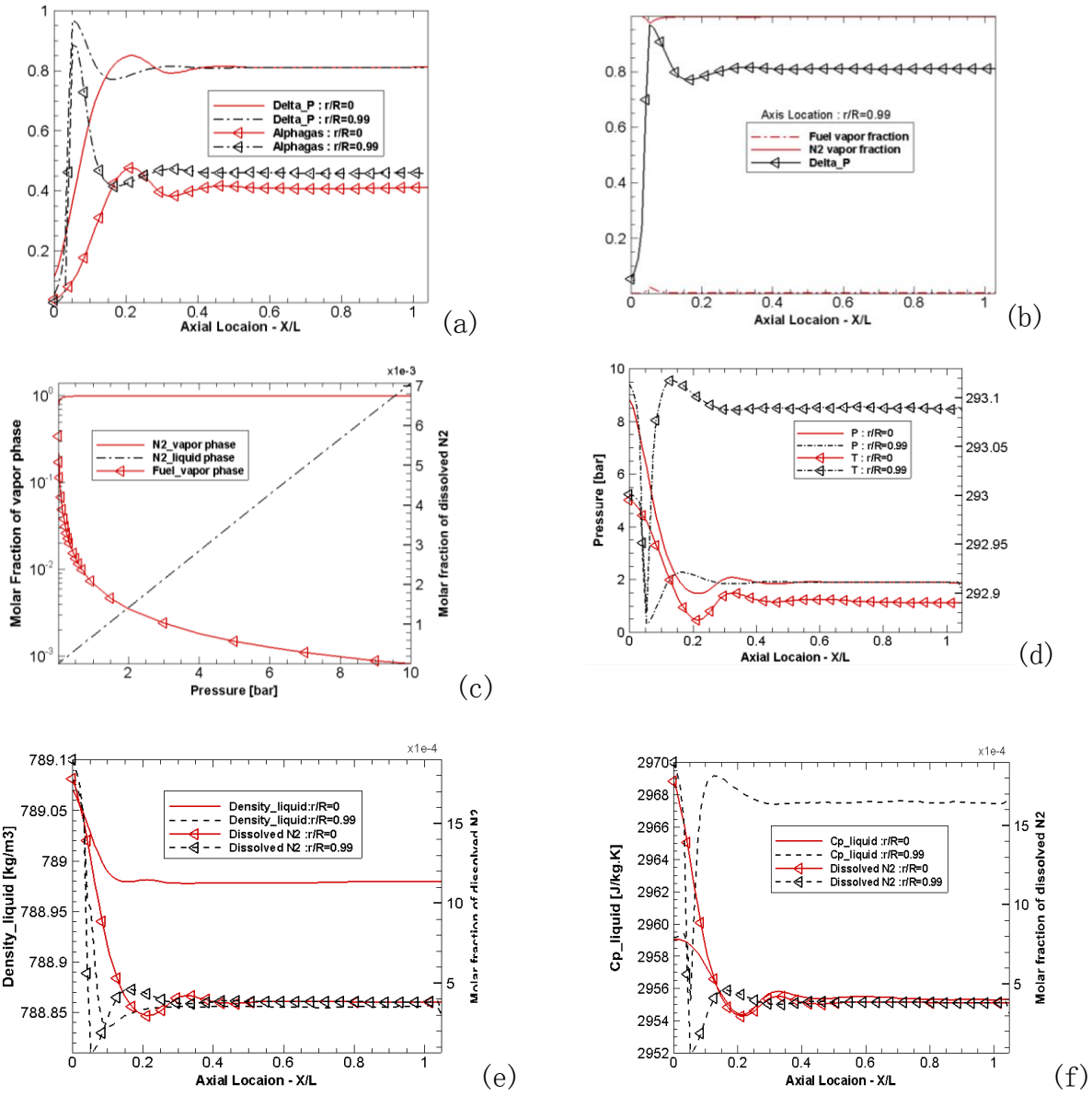

Figure 5.7 Thermodynamics analysis of properties variation in the nozzle. (a) denotes the variation of void fraction with $Delta\_P$ at central axis (r/R = 0) and near wall direction (r/R = 0.99), $Delta\_P = \frac{(10\ \text{bar} - \text{P})}{10\ \text{bar}}$; (b) denotes the variation of vapor molar fraction of fuel and nitrogen with $Delta\_P$ at near wall direction (r/R = 0.99); (c) denotes the variation of vapor molar fraction of fuel and nitrogen with the reduction of pressure at T = 293 K and Y_{N_2} = 1E-3; (d) denotes the variation of pressure and temperature at central axis (r/R = 0) and near wall direction (r/R = 0.99); (e, f) illustrate the variation of density and heat capacity with dissolved nitrogen at central axis (r/R = 0) and near wall direction (r/R = 0.99) respectively.

5.4 3D Cavitation Modelling with 4EQ-PR model

In this section, the 4EQ-PR model is used to simulate the cases with less N_2 dissolved in the liquid using more realistic mass fraction, Y_{N_2} = (2E-5, 2E-6), as listed in Table 5.2. The numerical results are compared to available experimental data from Duke et al. [104]. Although, the true nitrogen concentration is not known in the experimental conditions [23], [104], qualitative and quantitative comparisons will be carried out with selected experimental data. The effect of dissolved N_2 on the inception of cavitation and its development is also discussed. Finally, the analysis related with the nucleation process is presented.

5.4.1 Model validation against X-ray Radiography data

In the orginal experiments [23], [104], the nozzle using different materials (plastic, metal) have been tested under the non-degassed and degassed conditions. However, no quantitified data are known for the amount of N_2. Obvious differences are found for the results tested with different materials. An extra void cloud is detected with the plastic nozzle only under the non-degassed situation [23]. The effect of dissolved N_2 is much more minimized as tested with the metal nozzle [104]. According to Duke et al. [101], [104], they have attributed this to the effect of roughness in the plastic nozzle. In current simulation, a lot of void zones are found in the middle of the orifice for both cases as shown in Figure 5.8.Therefore, the current simulation presents more similarity as those in the latest experimental results tested with metal nozzle. This prediction can be confirmed by the following quantified validation.

The simulation is conducted under the large eddy simulation framework. For both initial mass fraction, Y_{N_2} = (2E-5, 2E-6) cases, the computational time is 0.36 ms and 0.44 ms, respectively. Since both cases have not reached the quasi-steady state, the presented comparison with the experiments are based on the latest time instant. Noteworthy that considering the compressibility of the liquid phase and the gas phase in our models has been shown to improve the accuracy of wave speed traveling in the

computational domain, but this accuracy has led to a longer time to reach steady state compared to previous studies [33]. The numerical results are calculated based on the integrated void fraction (α_g) along the cast ray for both cases. The line of sight integrations are performed in the $Y(0^\circ)$ direction as well as the rotated X (90°) direction, as illustrated in Figure 5.8. Although there exists possible difference for the actual N_2 concentration, the experimental x-ray images from ref. [104], both in non-degased and degassed cases are compared to the numerical results, in Figure 5.9 with initial mass fraction Y_{N_2} = (2E-5, 2E-6), respectively. The cavitation in the degassed case are much intensified than the non-degassed case. The cavitation cloud is more fragmented and dispersed for the degassed case. However, no significant differences are detected by Duke et al. [101] for the final averaged void distribution regardless of their (unknown) N_2 amount, as shown in Figure 5.9. The N_2 concentration in the degassed experimental case seem to be not small enough to make a difference. Indeed, the amount of N_2 seems to be closer to 2E-5 than to 2E-6, because of this very similar experimental images, displayed in Figure 5.9. Since only half geometry is simulated in this work, the radiography of the numerical results for the non-simulated half-nozzle have been obviously assumed the same as the simulated half-nozzle. Hence, the numerical radiography results shown in Figure 5.9 in the Y (0°) direction are computed (doubled) accordingly. Therefore, the radiography contour for the non-simulated half-nozzle in the X (90°) direction is the symmetry of simulated results. Besides, for the radiography in the X (90°) direction, the line of sight integration path can cover the whole nozzle diameter. In this case, the numerical radiography results depicted in Figure 5.10 are post-processed in a more straightforward manner. As shown in this Figure 5.10, the inlet sharp corner cavitation can be captured correctly with current LES simulations. Whereas, affected by the turbulence or non-fully convergence, the cavitation is not evenly distributed in the 0° and 90° directions, for both N_2 concentration cases. With limited computational time, the void distribution has not fully extended to the exit of the

orifice for the non-degassed case. However, the cavitating flow seems to be very close to its steady state, because the cavitation is still evolving, but very slowly as time is elapsed. This has justified our attempt for comparing the numerical and experimental profiles, as dissussed below based on Figure 5.10.

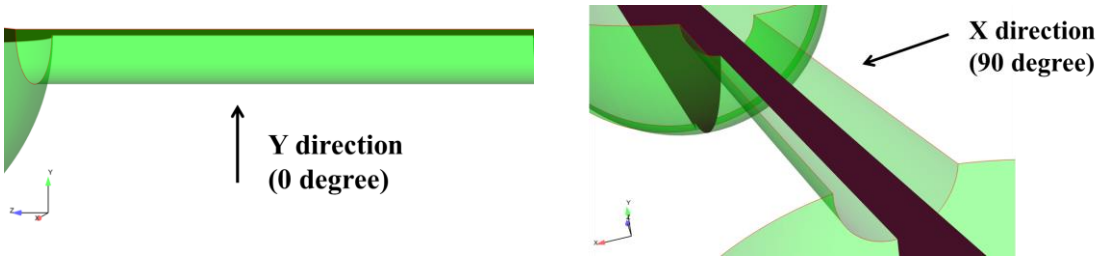

Figure 5.8 Demonstration of radiography direction for the post-processing of LES modelling results. X direction is the rotating view based on Y direction.

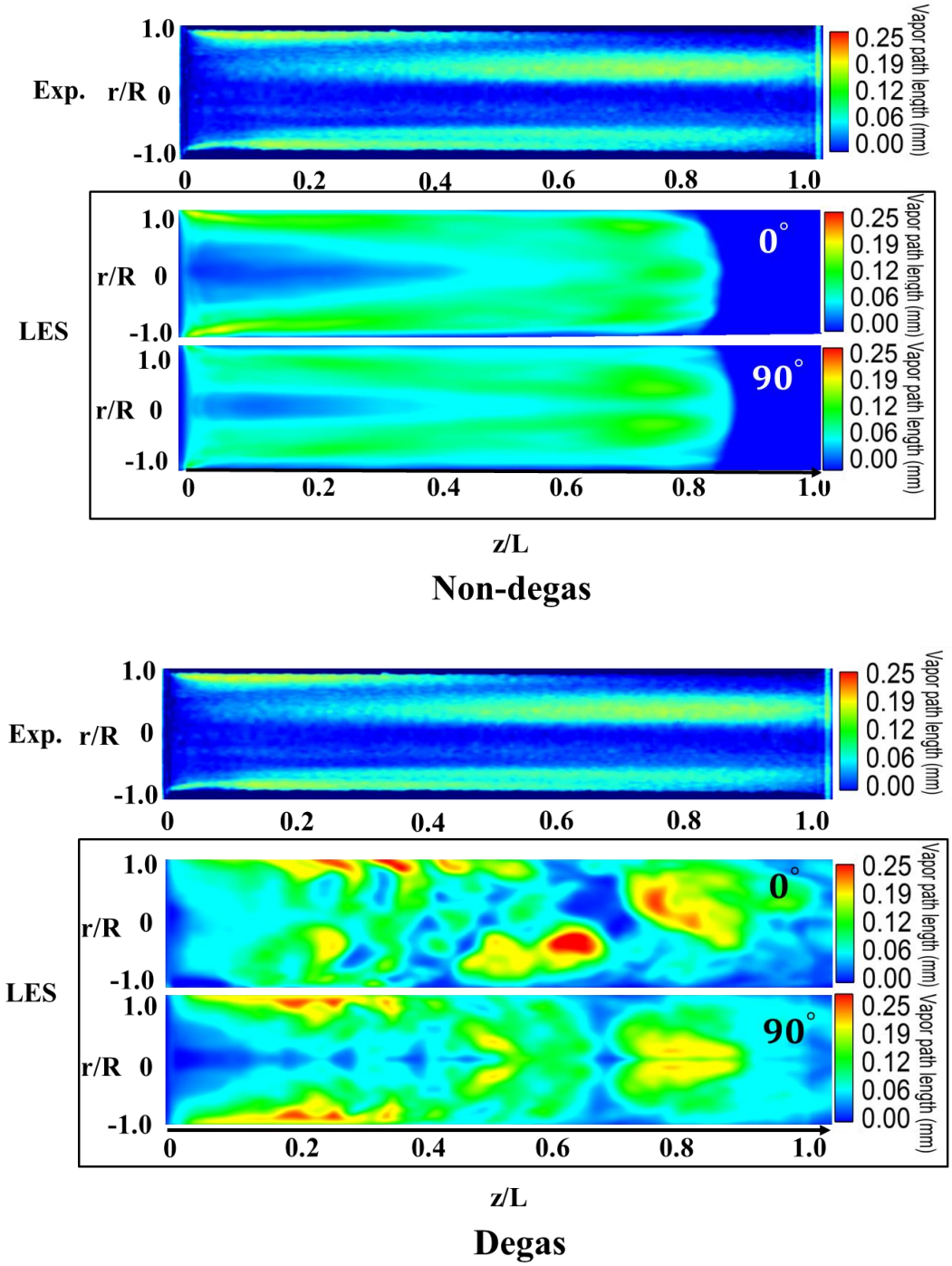

Figure 5.9 Comparison of radiography contour for integrated void fraction between X-ray experimental data and LES simulation results in which the experimental data are adapted from the ref. [104] and the modelling results are computed based on the line integration of volume fraction of gas (α_g) for the non-degassed case ($Y_{N2} = 2E-5$, t = 0.36 ms) and degassed gas case ($Y_{N2} = 2E-6$, t = 0.44 ms). The 0° view and 90° view denote the radiography are performed along X and Y direction respectively.

The comparisons with radiography X-ray experimental data are reported in Figure 5.10. The radial profile is plotted at the axial position through the detected maximum void fraction at the wall. For the non-degassed case (Y_{N_2}= 2E-5), this location is at the axial distance of $^{z}/_{L}$ = 0.1 (z is the axial distance from hole inlet and L is the length of the hole). However, the void fraction peak appears slightly farther from the inlet corner for the degassed gas ($^{z}/_{L}$ = 0.23). In contrast, the axial profiles for both cases are plotted along the wall of the orifice at ($^{r}/_{R}$ = 0.99) (r is the radial distance and R is the radius of the hole). The different modelling results at the same position depicted in Figure 5.10 are collected around the targeted position within a deviation of 0.05 mm. Firstly, for the non-degassed case (Y_{N_2}= 2E-5), the numerical axial and radial profile shapes follows the experimental results, but they are somewhat overestimated in the near wall for the $0°$ direction integration and underestimated for the $90°$ direction. Therefore, the averaged value of the two directions corresponds better to the averaged experimental profiles. Besides, the cavitation cloud appeared in the middle can generally agree well with experimental data for the non-degassed case. The uneven distribution of void fraction as aforementioned can be clarified both in axial direction and radial direction. In contrast, the numerical results of the degassed case (Y_{N_2}= 2E-6) has presented more unsteadiness and oscillations which is consistent with the results presented in Figure 5.9. Note that these oscillations also exist in the experimental radial profile. Thus, more complexities of the flow are witnessed in more degassed conditions. However, they are more pronounced in the numerical results compared to experimental predictions. This discrepancy may be due to a possible less degassed condition than (2E - 6) in the experiments. In addition, for the axial direction of the degassed case, except the strong oscillations, the overall LES void fraction distribution predictions compare fairly well to the experimental averaged profiles. Therefore, averaging the LES results based on longer computational time as well as realizing the spatial averaging (by computing the entire geometry) would

better highlight the correspondence with the averaged experimental results. This will be part of the future work.

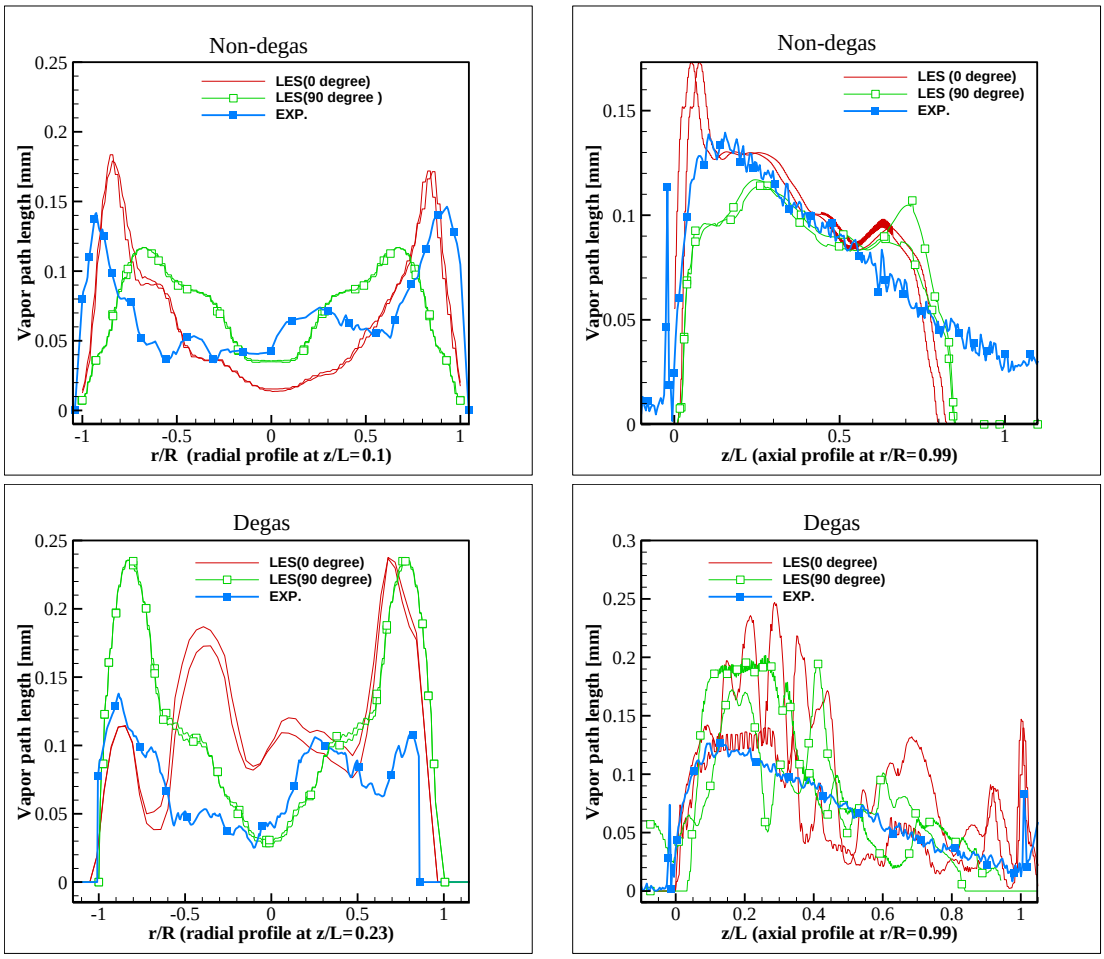

Figure 5.10 Quantified comparison between experimental data [104] and instantaneous LES results. The data for the dissolved gas case and degassed gas are collected at an time instant of 0.36 ms and 0.44 ms respectively.

5.4.2 Effect of N_2 on cavitation inception

As discussed in the previous section 5.1, higher N_2 concentration in the fluid will bring about the elevation of saturation pressure and the reduction of tensile strength for the cavitation inception. Thus, it is predictable that the cavitation will incept earlier if with more N_2 inside.

As shown in Figure 5.11, the cavitation zone is illustrated with the iso-surface of gas volume fraction equalling 0.5 (α_g = 0.5). As already discussed above, it is expected

to detect that the case with higher amount of N_2 ($Y_{N2} = 2E-5$) starts to cavitate at earlier time around 260 μs. In contrast, the inception of cavitation is severely lagged up to around 310 μs with less N_2 ($Y_{N2} = 2E-6$). The pressure is also larger for the fluid with more N_2 at the location of cavitation inception. Hence this result is consistent with the fact saturation pressure increases with higher amount of nitrogen, as discussed previously (Figure 5.2). One noting point is that the cavitation has not appeared in the inlet corner of the orifice for both cases. Instead, it starts in the shear stress layer as shown in the velocity contour in Figure 5.12. This phenomena has been confirmed in recent experimental observation. As a matter of fact, the cavitation inception has appeared at around z/L = 0.1 where pressure clip-planes are depicted in Figure 5.11. Then, the formed nuclei are transported downstream with the liquid flow, as shown in Figure 5.11. At the same time, more regions starts cavitating. It is interesting to note that with similar time interval (20 μs), the nuclei formation speed is much faster for the flow with a higher amount of N_2, as can be seen at the time interval [260 μs, 280 μs] , compared to the time interval [330 μs, 350 μs]. This implies that the dissolved gas increases the growth rate of the bubbles in addition to facilitating the inception of bubbles nuclei. With more gas in the fluid, the velocity of fluid is also slightly higher as shown in the Figure 5.12.

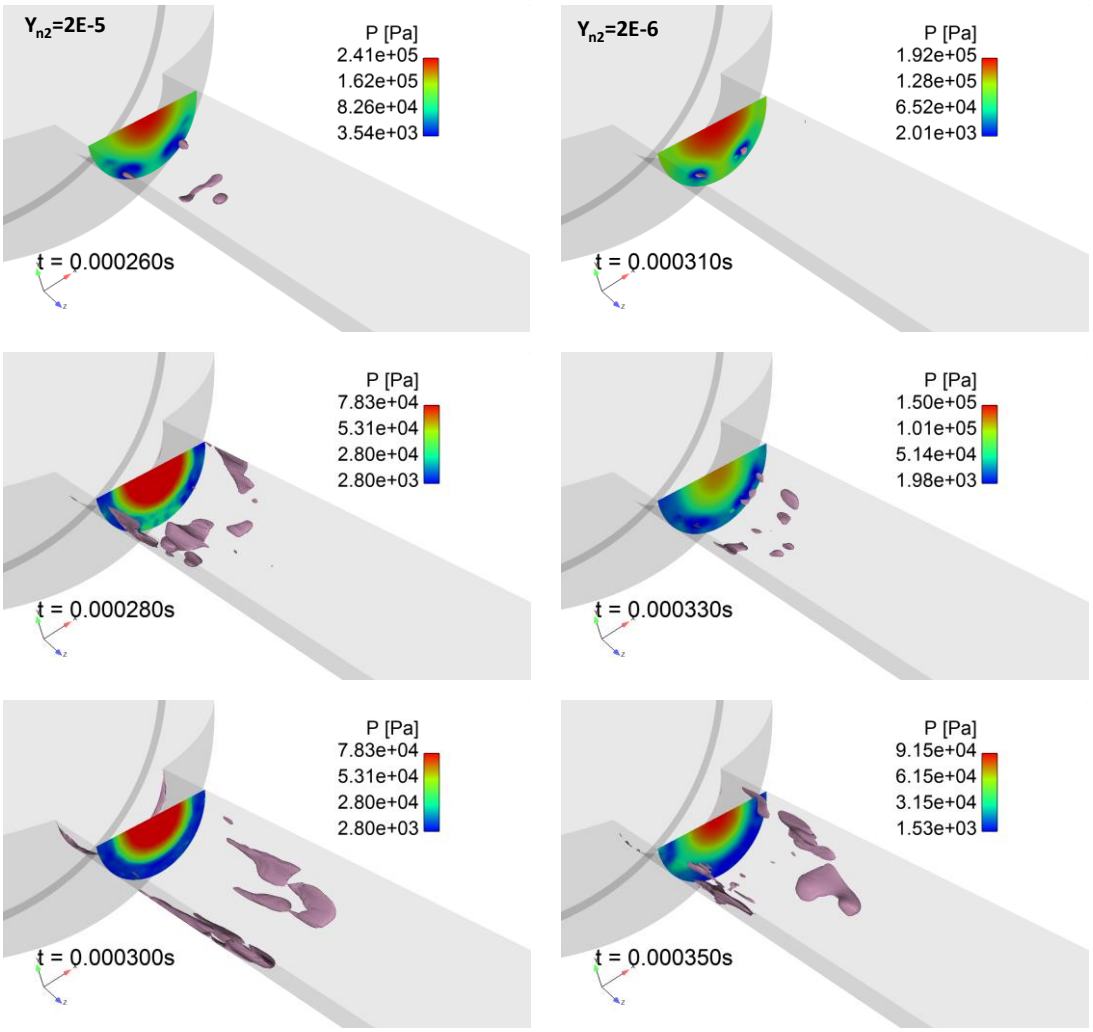

Figure 5.11 Demonstration of the effect of N_2 on cavitation inception and developing process. The cavity is presented with the iso-surface of gas volume fraction equalling 0.5 (α_g = 0.5). Case Y_{N_2} = 2E-5 (left images) and Case Y_{N_2} = 2E - 6 (right images).

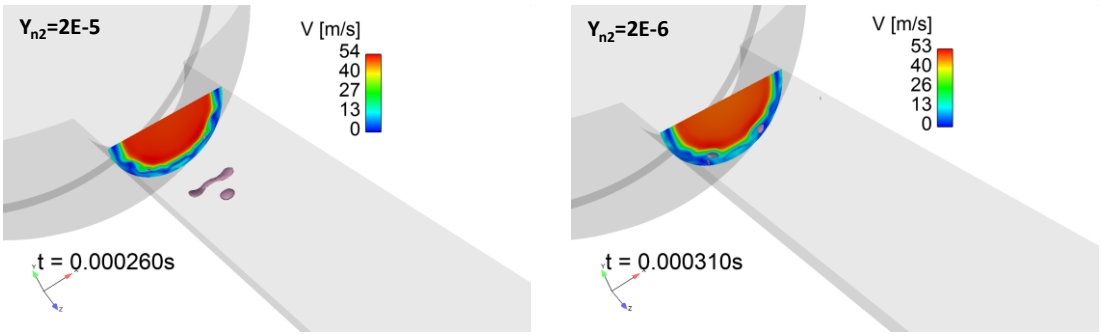

Figure 5.12 Demonstration of the effect of N_2 on the velocity contour at the location of cavitation inception. Case Y_{N_2} = 2E-5 (left images) and Case Y_{N_2} = 2E-6 (right images).

5.4.3 Effect of N_2 on cavitation developing

In fact, the difference of N_2 concentration not only affects the inception of cavitation, but also influences the cavitation developing process, as already discussed above. In this section, this phenomenon is discussed further. Figure 5.13 demonstrates the void distribution of the non-degassed and degassed cases at the same time instant (t = 0.36 ms). As can seen in this Figure, significant differences are detected for the two cases. With more dissolved gas, not only the nucleation process starts much earlier, but the growth rate of the cavitation is much faster than in the degassed case (*see* α_g= 0.2 iso-surface). Besides, the void zones are only found in the upper inlet positions of the nozzle in the degassed case, and the nucleation has not developed along the wall continuously. Instead, it starts at a concentrated region close to the inlet and spread around the same radial direction, in nearly the same section of the hole. With more N_2, the fluid flow behaves more stable and the formation of final cavitation zone (α_g = 0.8) is also slightly larger.

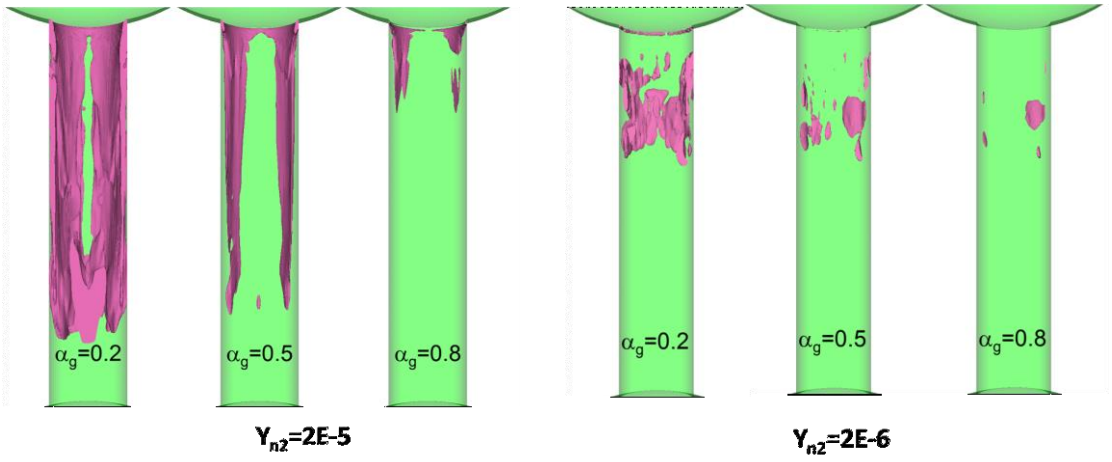

Figure 5.13 Demonstration of void fraction based on varied iso-surface of volume fraction of gas (α_g) at the time instant of 0.36 ms.

5.4.4 Analysis of nucleation process

With the phase equilibrium models developed in this work, the detailed analysis of nucleation process becomes possible. Indeed, the current cavitation test cases have demonstrated the phase transition from a multicomponent (Viscor, N_2) single-phase flow to a two-phase flow inside the orifice, automatically. In this section, phase transition (i.e. nucleation) is discussed further, as it constitutes one of the most important findings of this work.

The following discussion is based on the degassed case (Y_{N_2}= 2E-6). The initial fluid is thermodynamically proven to be at single phase state, even if the gas volume fraction (α_g) is as high as 1E- 4. The phase transition (i.e. nucleation) from a single liquid phase (pure multicomponent liquid) towards a two-phase, then further to a pure gas state, corresponds to the formation of resolved bubbles, as shown in Figure 5.14. In this Figure, the phase transition phenomena is highlighted by the variation of the void fraction from 1E- 4 to 0.01. The different nuclei keep growing from the fully dissolved N_2 state ($\alpha_g \leq 1E-4$) to two-phase situation ($\alpha_g \geq 1E-2$), finally free gas ($\alpha_g \geq 0.99$) if with enough long time, as can be seen by the increased maximum of the palettes in Figure 5.14.One noting point is the evolution of volume fraction of N_2 ($\alpha_{g,N2}$) which is defined with the formula $\alpha_{g,N2} = \alpha_g * y_{N2}$ (y_{N2} is the molar fraction of N_2 in the gas phase). The N_2 amount in the nuclei has kept increasing and almost 90% of the void is dominated by the N_2 as time evolves to 0.38 ms. However, in the earlier time (0.28-0.36 ms), the amount of N_2 is only half of the overall gas volume. In phase equilibrium model, restricted by the constraint $y_{N2} + y_{viscor} = 1$, the evolving of vaporous fuel and N_2 are mutually affected which also implies the procedures of gaseous cavitation and vaporous cavitation are mutually impacted. It is undeniable that gaseous cavitation plays a major role in the later stage of nucleation according to the current results. Another interesting point is that the nucleation process has seen the collapse of void bubbles, especially at later stage (t > 0.38 ms).

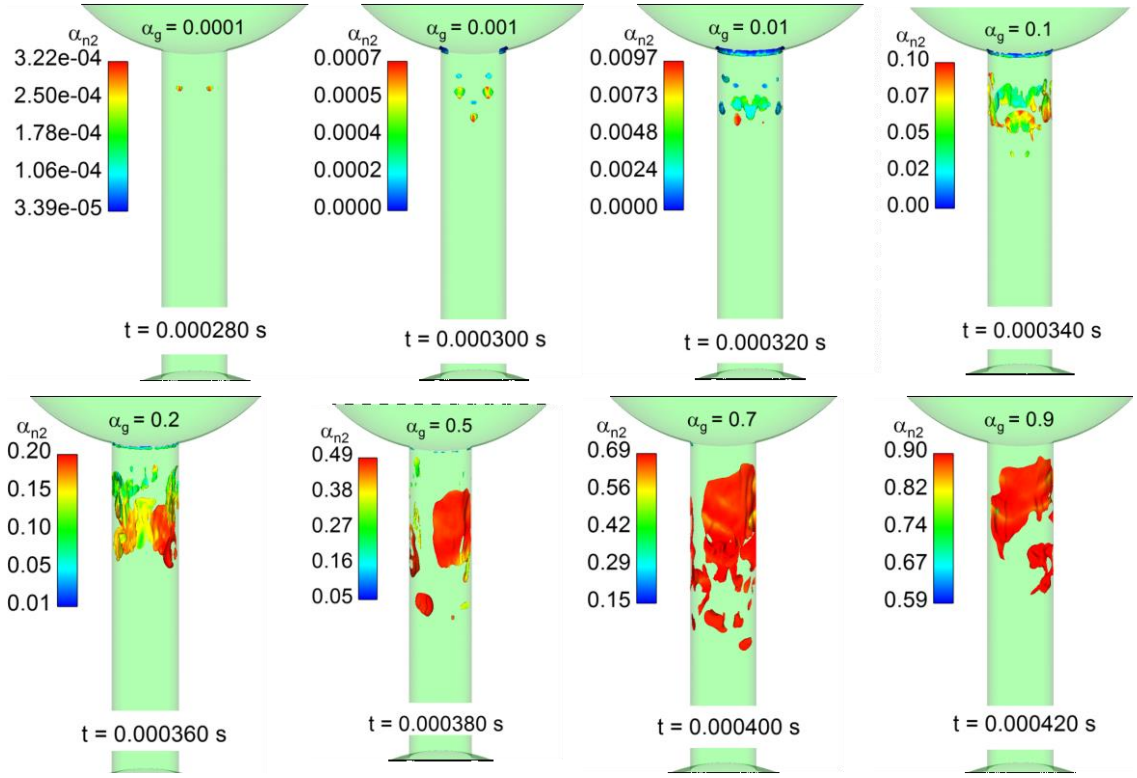

Figure 5.14 Demonstration of nucleation and cavitation development within the time intervals of 0.14 ms. The nucleation and cavitation zones are presented by iso-surface of varying void fraction at different time. The contour in the iso-surface represents the volume fraction of N_2.

5.5 Chapter Conclusions

In this chapter, the developed 6EQ-PR model and 4EQ-PR model have been employed to simulate the cavitation phenomena in a real size nozzle to investigate the effect of dissolved N_2 on the cavitation behaviour. As one of main findings of this work, the phase transition (i.e. nucleation) phenomena has been discussed in detail. To be more specific, the 6EQ-PR is used to model the 2D nozzle configuration with an initial saturated two-phase state. Then the 4EQ-PR model is used to model the 3D configuration with two different N_2 concentrations which represent the non-degassed case and degassed case, respectively. The results have been validated with available experimental data. Several conclusions have been drawn from the simulations:

1) Both the 6EQ-PR model and 4EQ-PR model are able to predict the cavitation phenomena qualitatively and quantitatively.
2) The solver is able to predict the nucleation process dynamically, as well as the effects of dissolved N_2 on the cavitation.
3) With more dissolved N_2, the cavitation inception time is much earlier than for degassed fluid.
4) Much unsteadiness is detected for the case with less N_2. More studies are needed to find the mutual effect of turbulence and dissolved N_2 as well as the effect of heterogeneous nucleation, especially at rough walls.
5) With the consideration of LES and real fluid effect, the time to reach quasi-steady state is much longer than previous reported RANS modelling results.

6 Transcritical and Supercritical Spray Modelling

In this section, the developed 4EQ-PR is applied to the 3D transcritical and supercritical spray modelling to further test the capability of the solver in dealing with multiscale configuration. The modelling results have been analysed with thermodynamics theory and available experimental results.

6.1 Low injection pressure sprays

I. Geometry configuration and computational set up

The computational configuration is a typical injector which consists of a single-hole (Length = 1 mm and Diameter =100 μm) fitted to a hexahedral chamber, as shown in Figure 6.1. The total number of cells are 1504800 with the minimum size of 10 μm. The boundary conditions are set with pressure inlet and outlet in the left and right side of the geometry, respectively, as shown in the cross-section of the grid presented in Figure 6.1. The injection pressure is set with 70 bar, which is above n-dodecane pressure critical point (18.2 bar).

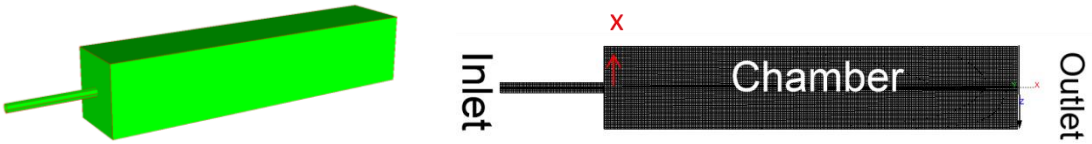

Figure 6.1 (a) is the 3D geometry; (b) is the mesh configuration in central section. The computations are conducted with 256000 cells and a CFL number equals to 0.25.

The details of initial boundary conditions are listed in Table 6.1. For all test cases, the working fluid is a mixture of n-dodecane and nitrogen. The global scenario is liquid n-dodecane (at 363 K) is injected into higher temperature gas (at 900 K) in the chamber. In the first two cases (Cases 1.1 and 1.2), an almost pure liquid n-dodecane (at 363 K lower than n-dodecane critical point 658 K) is injected into the chamber

filled with an almost pure vaporous n-dodecane (at temperature 900 K and pressure, 40 or 60 bar, higher than n-dodecane pressure critical point, 18.2 bar). On the other hand, Cases 2.1 and 2.2 are aimed at modelling a more realistic conditions of diesel injection in transcritical conditions. In these cases, the chamber is filled with an almost pure gaseous nitrogen (at temperature 900 K and pressure 40 or 60 bar, higher than nitrogen pressure critical point, 33.1 bar). In fact, the chamber conditions are above the critical point of any single component in this system regardless of pressure or temperature.

Table 6.1 Initial condition for the 3D injection modelling.

Case No.	P_{inlet} /Mpa	P_{outlet} /Mpa	$P_{chamber}$ /Mpa	T_{chambe} /K	$T_{liqzone}$ /K	$Y_{liqzone}^{c12}$	$Y_{gaszone}^{c12}$
1.1	7	6	6	900	363	0.99999	0.99999
1.2	7	4	4	900	363	0.99999	0.99999
2.1	7	6	6	900	363	0.99999	0.00001
2.2	7	4	4	900	363	0.99999	0.00001

Y_{c12} denotes the mass fraction of n-dodecane.

II. Results and Discussion

Firstly, as for Case1.1 and 1.2, the pressure in the whole injection process is above the critical point of fuel, but the temperature has been through the transition from subcritical to supercritical in the chamber. No phase transition is observed in whole injection process. In this mixing regime, the liquid jet behaves like a gaseous jet, as depicted by the fluid phase state TPD in Figure 6.2 (C, E) at 70 μs. The phase state is identified by the tangent plane distance (TPD) criterion [97]. In current study, for the post-processing convenience, we have employed different TPD values to show the flow state. TPD = 0, 1 or 2 correspond to single gas phase state, single liquid state or two-phase state, respectively. In current research, the model used to differentiate

between single liquid (or liquid-like) and single gas (or gas-like) is based on the relation of feed and equilibrium constant (i.e. species composition z_i and equilibrium constant K_i): $\sum \frac{z_i}{K_i} < 1$ (pure vapor) and $\sum z_i K_i < 1$ (pure liquid) [62]. Therefore, it is easy to verify from Figure 6.2 (C, E) that the overall flow is in single flow state (TPD = 0 and 1) and, the fluid is still in supercritical regime in all the cells of the computational domain. To be more specific, the flow has transited from pure liquid (TPD = 1) in the liquid core to higher temperature gas state (TPD = 0) directly without crossing the two-phase envelop (i.e. only crossing the pseudoboiling-line but not the vapor-liquid co-existence line here for supercritical conditions). Hence, the whole injection process is in supercritical regime. Moreover, the boundary of white isosurface marked with TPD = 1 in Figure 6.2 (D, F) is very close to the maximum value of heat capacity (Cp), which corresponds to the pseudoboiling-line, depicted in Figure 6.3 (G). To better understand these intricate phenomena of supercritical injection regime, reduced pressure (Pr) and temperature (Tr) radial profiles are plotted at 70 μs in Figure 6.3 (H), in a section located at a distance of 0.5 mm from the nozzle outlet, as depicted by the arrow in Figure 6.1 (B). The temperature has seen a gradual increase from liquid core to the out layer of the jet. However, the pressure is approximately constant, the same as chamber pressure along this section. The mixing layer exhibits a similar behaviour as a gaseous jet. When plotting the variation of heat capacity (Cp) at this section versus temperature, a maximum value can be observed for both cases, as shown in Figure 6.3 (I). These maximum points in the Cp curves belongs to the pseudoboiling-line depicted in Figure 6.3 (G), that separates liquid-like from gas-like supercritical fluids [7]. In addition, the collected Cp values are compared with the data from Coolfluid thermal properties library [105] and a good agreement has been achieved. It can be also seen in Figure 6.3 (I) that the maximum value becomes higher when the ambient pressure is closer to the critical point. Indeed, the variation of Cp at lower chamber pressure (Pr = 2.2, case 1.2) has presented stronger non-linearity than higher chamber pressure (Pr = 3.3, case 1.1). The Cp

distribution also widens and flattens at higher pressure as confirmed by Banuti [7]. The case with lower chamber pressure (Case 1.2) also corresponds to lower pseudoboiling temperature which can be proved in the path 2 and path 3 of Figure 6.3 (G).

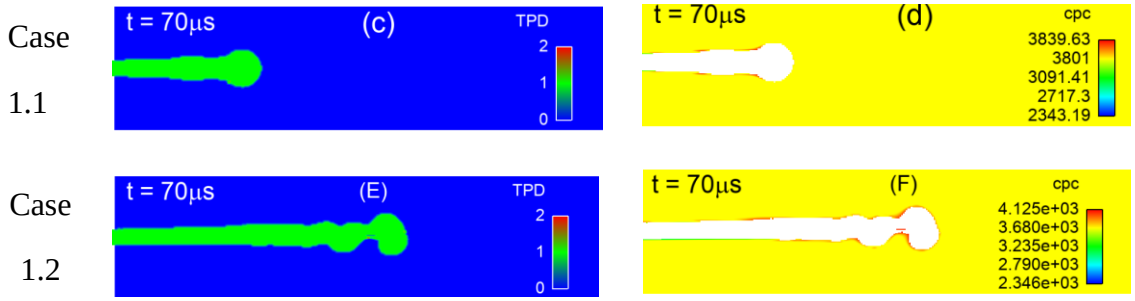

Figure 6.2 3D supercritical modelling with the 4EQ-PR model. (C, E) show the phase state (gas phase TPD = 0 and liquid phase TPD = 1) at different time instants. (D, F) show the heat capacity contours at 70 μs around the liquid core represented by isosurface between TPD = 0 and 1.

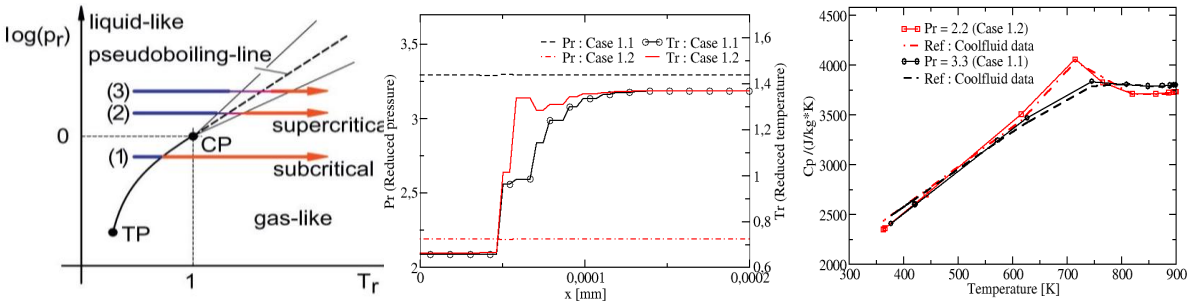

(G) (H) (I)

Figure 6.3 3D supercritical modelling with the 4EQ-PR model. (G) denotes different modelling regimes with regards to the variation of Tr and Pr from ref. [7]. (H) illustrates the evolution of pressure and temperature from the middle of liquid core to the out layer of the jet in the radial section with a distance of 0.5 mm from the outlet of the nozzle. (I) plots the variation of heat capacity with temperature in the radial section at a distance of 0.5 mm from the outlet of the nozzle for case 1.1-1.2 (solid line with symbols). The dashed lines are the data from CoolProp open source library [105].

In contrast, Cases 2.1- 2.2 demonstrate the transcritical regime. The thermal condition of Case 2.1 is similar to ECN Spray A [44] except the lower injection pressure of 70 bar that has been adopted in this study instead of 1500 bar. The results of high injection pressure will be demonstrated in the following section. Different with Cases 1.1-1.2, the chamber is, in Cases 2.1- 2.2, filled with almost pure nitrogen (see Table 6.1). During the simulation, there are a lot of N_2 mixing with the n-dodecane jet, which has raised significantly the mixture critical point. As mentioned in Section 1.2.2, the mixture critical pressure has proved to exceed 3000 bar at low n-dodecane concentration (around 0.05). As the chamber pressure is usually much lower than such high mixture critical pressure, some zones lying in subcritical regime surely exists around the liquid core. To verify this hypothesis, the TPD fluid state is shown at 46 μs and 70 μs in Figure 6.4 (K, M, O, Q). A clear two-phase zone (TPD = 2: red color) enveloping the liquid jet can be observed for both cases. This two-phase zone is the main feature of the transcritical regime making it distinct with the previous results of Case 1.1-1.2 (compared to Figure 6.2 (C, E)). These results corroborates the latest experimental findings from Crua et al. [8], who have proved that there exists phase transition even when the operating conditions is at supercritical condition with regards to the pure fuel critical point. Finally, it is worth noting that with smaller pressure difference, Case 2.1 has shown wider two-phase zone because of the lower velocity (

Figure 6.4 (K, M). Therefore, the two-phase zone enveloping the liquid core should be thinner using higher injection pressure. But, this work has proved that this subcritical zone exists and is the location of liquid evaporation and may be primary atomization. The contour of mass fraction of vaporous n-dodecane for these two cases are demonstrated in Figure 6.4 (L, N, P, R).

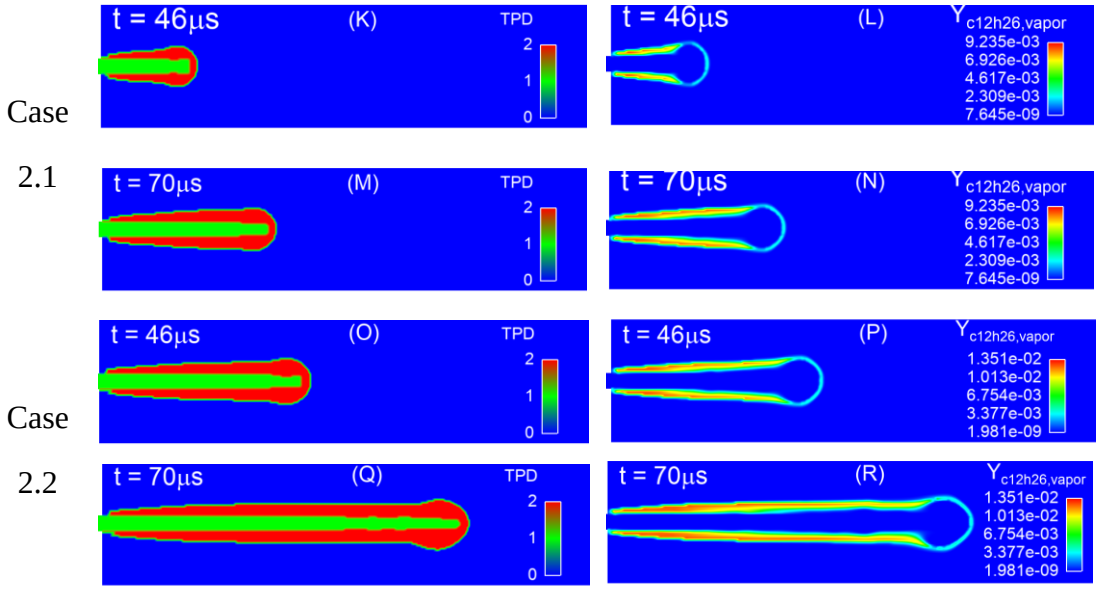

Figure 6.4 3D transcritical modelling with the 4EQ-PR model. (K,M,O,Q) show the phase state (gas phase TPD = 0, liquid phase TPD =1 and two-phase mixture TPD = 2) for four cases at different time instants. (L, N, P, R) show the mass fraction of vaporous n-dodecane for cases 2.1 and 2.2 at 46 μs and 70 μs.

The T-x phase diagram of $C_{12}H_{26}$-N_2 system is plotted in Figure 6.5. It includes the frozen temperature or adiabatic temperature T_f and equilibrium temperature T_e. The frozen temperature is computed without consideration of phase transition, formulated as,

$$h(T_f, P) = z_{fuel} * h(T_{fuel}, P) + (1 - z_{fuel}) * h(T_{ambient}, P) \quad (6.1)$$

In which, $z_{fuel}$and h represent the molar fraction of fuel and enthalpy at given temperature and pressure, respectively. T_{fuel} and $T_{ambient}$ denote the temperature of fuel and ambient, respectively. The obtained T_f actually symbles the adiabatic mixing temperature of different species. If further take into account the phase state, a stability test and phase equlibrium computation can be proceeded to obtain the final equilibrium temperature T_e. The T-x profiles are plotted at the constant pressure of 60 bar. It is evident to find that the scattered points of T_e from CFD simulation can

agree well with the equilibrium temperature calculated directly with phase equilibrium model for case 2.1. The non-uniform scattered points are attributed to the low mesh resolution. The non-conservativity of energy with current flow model has not adversely impacted the prediction of temperature. Actually, this temperature is more related with phase equilibrium model. Moreover, the curve of equilibrium temperature has crossed the two-phase region which proves the possibility of phase transition. Another intriguing point is that the frozen temperature has shown minor difference with equilibrium temperature in most regions except as the molar fraction of is approaching 75% which may imply the diesel injection process can be modelled with the mixing regime without losing significant accuracy. As the temperature of fuel is further increased to 670 K, the equilibrium curve will be tangent with the critical point. Due to the two-phase zone is not crossed, the whole injection regime will be fully in the supercritical mixing condition.

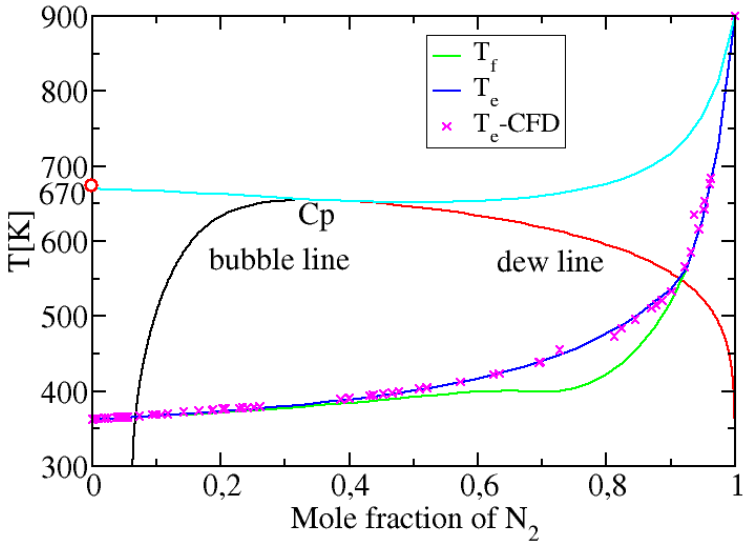

Figure 6.5 Temperature-composition (T-x) diagram at P = 40 bar, 60 bar, 80 bar. T_e and T_f are the equilibrium temperature and frozen temperature respectively. The scattered points are obtained from CFD modelling.

III. Discussion about the transition regimes

As proved in the work of Crua et al. [8], in classical diesel injection condition, the spray has been through the evaporation stage firstly, then a transition zone and finally enter the supercritical mixing regime. The transition time varies based on the fuel properties and chamber conditions. As observed in the experiments [8], the lighter fuel heptane can directly enter supercritical mixing regime as the chamber condition is above 1200 K and 106 bar. In contrast, the heavy fuel dodecane will sustain in the two-phase region for a rather long time. Actually, these phenomena can be explained by the phase equilibrium diagram. Figure 6.6 has illustrated the T-x diagram at a constant pressure of 106 bar for heptane, dodecane and hexadecane which corresponds to the experimental condition listed in ref. [8]. The initial temperature for all the fuels are set with 363 K. It is evident to find that the two-phase zone enclosed by the equilibrium temperature curve, bubble line and dew line has increased significantly from heptane, dodecane to hexadecane. The critical point of heptane is also much lower than the other two fuels. Especially for heptane, the transition temperature (around 480 K) from two-phase region to single phase is relatively low compared with the others. The amount of N_2 at the transition time is close to 70%. In contrast, the two-phase region for hexadecane is the largest and the temperature needed for entering transcritical mixing regime is above 600 K with around 90 % N_2 inside. In addition, for different fuels, once the initial temperature is high enough, the two-phase zone can be skipped and the whole injection is dominated by supercritical mixing regime from the inception moment. This temperature is very close to the critical value of each fuel. For example, for hexadecane, this transition temperature can reach 720 K shown as in Figure 6.6.

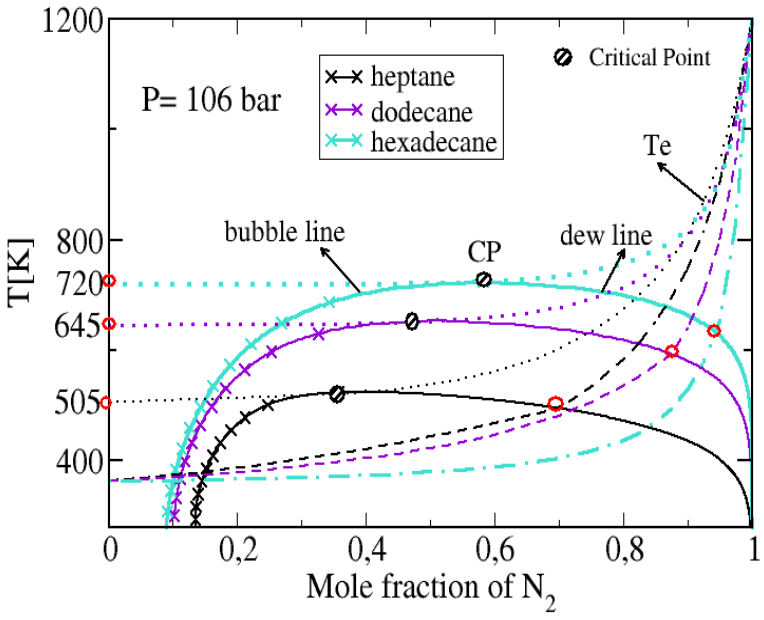

Figure 6.6 T-x diagram at the constant pressure of 106 bar for three different fuels (heptane, dodecane, hexadecane). T_e is the equilibrium temperature for three different fuels (heptane, dodecane, hexadecane) with an initial temperature of 363 K.

6.2 High injection pressure sprays

6.2.1 ECN Spray A injector modelling

In this section, the aforementioned two-phase flow compressible model 4EQ-PR is applied to simulate the real diesel injector Spray A from Engine Combustion Network [44]. Two models have been utilized to perform the simulation: one has considered the phase change part namely including vapor liquid equilibrium solver shorted for 4EQ-PR-EQ model; the other one has neglected the equalling of chemical potential and the vapor liquid equilibrium model is neglected during computation, named as 4EQ-PR-Wo-EQ model as a contrast. Referred to the previous discussions in Section 3.4, the 4EQ-PR-EQ model has included the relaxation of pressure, temperature and chemical potential as reaching the equilibrium state. Whereas, the 4EQ-PR-Wo-EQ model only considers the equalling of pressure and temperature. This assumption is valid based on the fact that the time scale of relaxing Gibbs energy

is much longer than relaxing pressure and temperature. It is reasonable to assume no phase change appears in such short time.

The simulation results from both models are compared to experimental data. A detailed discussion about the results of 4EQ-PR-EQ and 4EQ-PR-Wo-EQ results is also presented.

I. Introduction

The widespread applications of fuel injection at high pressure and high temperature (HPHT) conditions in compression ignition engines, gas turbines and rocket engines have stimulated great interest in studying the liquid injection experimentally and numerically.

Researches related to real-fluid injection were previously concentrated on the liquid rocket engine field, and then extended recently to the diesel engine industry. As confirmed in abundant experimental studies of liquid rocket fuel injections, the spray has been through an evident transition from two-phase atomization, breakup and droplets evaporation dominated physical processes to continuous diffusion and mixing phenomena as the pressure increases from subcritical condition towards supercritical condition. One primary reason for such transition is the gradual diminishing surface tension and latent heat as the ambient condition is above the critical point of the injected fuel. In fact, similar transition phenomena also occur during the injection in diesel engines, as investigated by several researchers [8], [15], [32], [48]. For example, Crua et al. [8] proposed a criterion for the mixing transition based their recent experimental observations. They observed the droplets undergo gradual transition from subcritical evaporation to mixing regime for different pressure and temperature above the pure fuel's critical point. Thereby, they confirmed that the fuel still stays in the subcritical two-phase state for some time before fully entering the diffusion mixing regime and the transition time varies with fuel types and droplets size. Thus, it is reasonable to conclude that in the whole injection process, the combination of classical evaporation regime for the main liquid core and transition to

the dense gas mixing state is possible at high ambient temperature especially for the droplets formed by possible primary atomization near the nozzle and for late injected droplets at the end of the injection events, the same as the droplets tracked experimentally by Crua et al. [8]. This conclusion indirectly justify the development of the proposed real-fluid diffused interface model (DIM) model, that aims to model the subcritical regime with the consideration of phase change, supercritical regime, as well as the transition from one to the other simultaneously. All the above experimental observations have provided valuable references and guidance for modelling. One classical benchmark case that may correspond to the mixing transition regime is the ECN spray A case operated under the high pressure and temperature evaporating conditions. Many researchers have contributed to the modelling of the spray issuing from this typical Diesel injector. Generally, the involved models are usually based on the Eulerian-Lagrangian (EL) approach. As the spray is modelled with Lagrangian approach, the liquid phase is generally treated as dispersed particles with various diameters, smaller than the grid size, while the gas phase is regarded as the continuous Eulerian carrier fluid. This computational strategy has shown excellent efficiency in the modelling Diesel spray using different sub-models including the "blobs" injection method, primary atomization and secondary break-up and evaporation [106]. However, because of the obvious EL approach deficiency in simulating the near nozzle region, some researchers have proposed an Eulerian Lagrangian Spray Atomization (ELSA) method in which an autonomous transition from liquid Eulerian jet method to Lagrangian method is used as the jet develops from the near nozzle dense zone to the downstream dilute zone [28]. Indeed, recent work from Xue et al. [35] has confirmed that turbulent-mixing based Eulerian model can predict better physics in the near nozzle region than Lagrangian method for the simulation of ECN spray A injector at non-evaporative condition. However, the incompressibility assumption of the liquid phase in their model and the absence of specific modelling for the primary atomization have limited the accuracy of the

downstream dispersed spray numerical results. This is the reason why Devassy et al. [2] have developed an Eulerian-Eulerian atomization model similar to the ELSA approach using a fully compressible model including a two surfaces density balance equations (TwoSD) model for the liquid core atomization and the droplets secondary breakup. This model has shown the huge effect of in-nozzle cavitation on primary atomization [20], and thereby demonstrating the necessity of considering physical primary atomization models directly linked to internal nozzle flows for more accurate injection simulations. In these conditions, the two successive Eulerian and then Lagrangian simulations -- coupled through collecting the flow information at the orifices exit as boundary conditions for the downstream Lagrangian spray simulation -- cannot provide better accuracy for the primary atomization of the liquid jet, especially for multiple short injections usually performed in advanced calibration of engines. In contrast, the Eulerian method based on the continuum fluid theory can easily realize the accurate modelling from the in-nozzle flow to dilute downstream spray continuously. While the computational cost is much higher than Lagrangian strategy, it is still tractable if applied with varying mesh resolution based on different regions or using automatic mesh refinement.

Currently, the compressible Eulerian based model has been successfully applied to the ECN spray A modelling as demonstrated in the earlier work of Lacaze et al. [15], as well as in the recent works of Matheis and Hickel [32], and Ma and Ihme [48], [36]. Since the physical properties of the fuel at HTHP condition are far away from ideal gas state, real-fluid EoS especially Peng Robinson (PR) EoS is widely employed for the modelling of transcritical flows and the transition from subcritical regime to the supercritical mixing regime, because of its good compromise between computational efficiency and accuracy. The involved thermodynamics models vary according to whether considering the phase change phenomenon or not. Indeed, in the case of a flow with phase change, the vapor-liquid equilibrium (VLE) theory is considered. Otherwise, if no evaporation nor condensation are expected in the whole computation,

a direct solving of PR EoS for the multicomponent single-phase mixture can readily provide the solution. However, the later single-phase simulation strategy may be risky if the flow thermodynamics state enters the vapor dome. As a consequence, the simulation may crash due to the appearance of negative pressures, as reported in [107]. According to Castier [79], negative pressure usually indicate that the fluid is in two-phase state. Since the cost of solving VLE equations is high especially for the full injector simulation, a compromising solution proposed by Knudsen [36] is to find an approximate saturation pressure corresponding to the point of $((\frac{\partial P}{\partial \rho})_T = 0)$ instead of solving the real saturation state. Even if this method is not theoretically valid and the phase change process is neglected, fairly good numerical results such as jet penetration length, mass and momentum flux can still be achieved in the simulation of ECN spray A injector [36]. The undeniable fact based on the experimental results is that two-phase subcritical regime indicators like droplets observation with relatively significant surface tension indeed exists when injecting fuel like n-dodecane or hexadecane in HTHP conditions, as discussed by Crua et al. [8]. However, the numerical results of Knudsen et al. [36] discussed above have stimulated us to wonder whether the evaporation process really play an important role in HTHP injection modelling. This is the main topic the current paper would like to investigate and discuss.

All the previous work experimentally or numerically has enlightened us to explore more about the transcritical modelling in HTHP diesel engine. In this section, a full spray A injector containing the needle to target part is simulated with the assumption of considering phase change and no phase change situations. The phase change procedure is realized with vapor-liquid equilibrium computation as described in our previous work [97]. The flow solver employed in the current work have been implemented in the in-house code IFP-C3D [55], in which a fully compressible non-equilibrium two-phase flow seven-equation model is resolved as presented in previous work of Habchi and Devassy [2], [33]. Since the involved EoS in the original

system is employing the Stiffed Gas (SG) EoS for liquid phase and ideal gas EoS for gas phase, it is not applicable for the HTHP injection modelling. Therefore, a real fluid phase equilibrium solver based on PR EoS has been developed and implemented into this seven equation two-phase flow solver, and has been applied to analyse a series of 1D academic test cases and 2D cavitation modelling [34]. Following this stage, a further reduced four-equation model with the assumption of mechanical and thermal equilibrium has been proposed and combined with the real fluid phase equilibrium solver [97]. This four-equation model has been successfully applied to 2D supercritical and transcritical injection modelling in [108], and achieved a good agreement with experimental results in the 1D flash boiling conditions, as reported in [97]. Based on these previous studies, the real fluid DIM solver will be further utilized to explore its potential in solving multi-scale injection problems at HTHP conditions.

II. Numerical set up

The spray A injector is a common-rail single-hole injector with a nominal diameter of 0.09 mm. To consider the effect of in-nozzle flow and expected pressure oscillations, the configuration has included the lower control chamber just above the needle, in addition to the sac and orifice, as shown in Figure 6.7 (a). Thus, the whole computation contains not only the classical spray inside the chamber, but also more challenging in-nozzle flow. In the simulation, the needle lift is assumed stationary at its maximum value taken to be equal to 500 μm. The computational grid has been generated by using the ANSYS ICEM Package with body-fitted multi-block hexahedral cells. In addition, the actual shape of the sac and orifice available at the ECN website [44] is used (stl* for the injector serial # 210675). To keep the computational costs tractable, a varying grid strategy is employed aimed at different zones of interest. Specifically, the in-nozzle part and main spray region is much more refined compared to other regions and the far downstream is distributed with relative coarse mesh (Figure 6.7 (c)). The orifice is discretized with 24 cells with an average size of 3.75 μm, as depicted in the zoomed view in Figure 6.7 (b, d). The minimum

mesh size is located in the near nozzle region. The coarsest mesh with the size of 8 mm exists in the far downstream region, which is not of interest in this study.

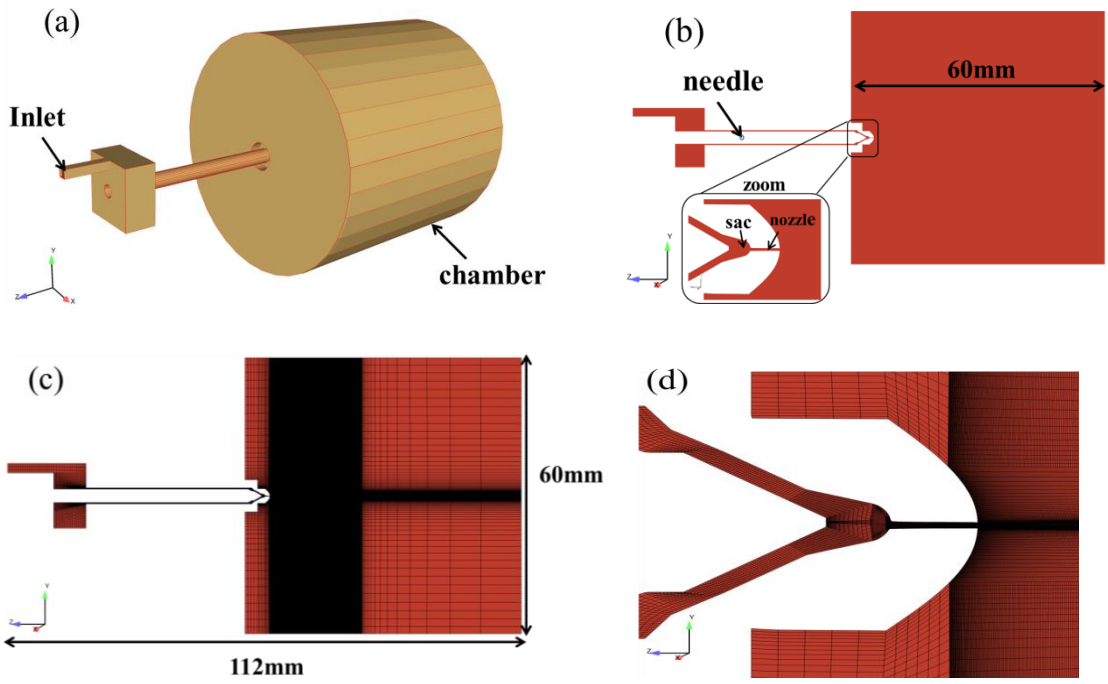

Figure 6.7 (a) Configuration of whole computational zone, note the lower control chamber at the fuel inlet. (b) Cut slice of the computational domain. (c) Mesh illustration in the cut plane, note that only the near nozzle region (20 mm axial length) is well refined. (d) Zoomed region in the near nozzle zone.

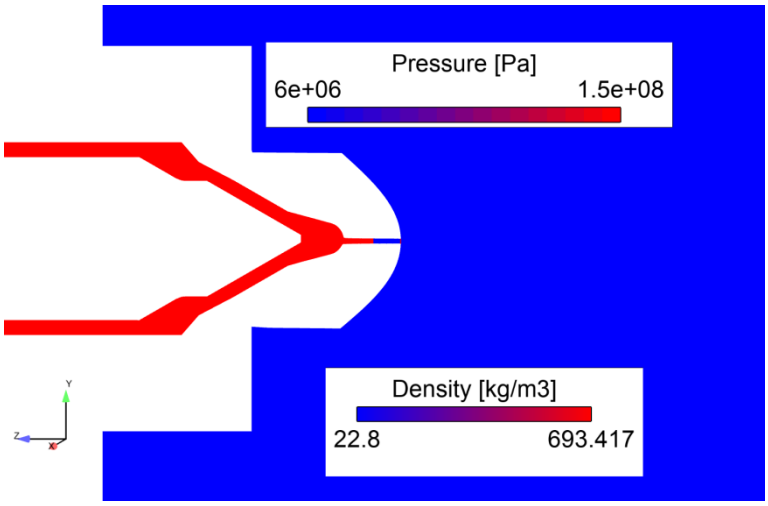

Figure 6.8 Initialization of the pressure and density (needle lift = 500 μm).

Since the modelling configuration contains different nozzle parts, including mainly the needle and the sac, appropriate initialization of the fluid is extremely important. Many different fluid states may exist in the sac as recently observed using x-ray experiments [109]. Indeed, due to multiple successive injection, the orifice and sac may be full of fuel or a mixture of fuel and air bubbles. The study here has referred to the conclusion from Payri, et al. [110], in which they have proposed to initialize simulations with the orifice filled with gas especially in the situation with high back pressure. As stated in this study [110], the presence of gas in the nozzle may significantly impact the initial transient phase of the jet. In this work, the initial pressure and density are illustrated in Figure 6.8. For the convenience of computation, the initial gradient is set in the middle of the orifice with almost pure liquid n-$C_{12}H_{26}$ (including an initial N_2 mass fraction equal to 10^{-5} in the left side and pure N_2 in the right. The working fluid is n-$C_{12}H_{26}$ with the temperature of 363 K. The chamber is initialized with N_2 at the temperature and pressure of 900 K and 60 bar, respectively, which corresponds to the gas density of 22.07 kg/m^3. The inlet and outlet of the overall configuration are both set with pressure boundary condition. Among them, the inlet is imposed with the operating pressure of 1500 bar to be close to the experimental condition. Other numerical settings can be found in Table 6.2. The simulations are conducted within the large eddy simulation (LES) framework. The involved sub-grid scale model is the Smagorinsky model.

Table 6.2 Operating conditions for the ECN Spray A modelling.

Models	4EQ-PR-EQ (Equilibrium solver) 4EQ-PR-Wo-EQ (Without Equilibrium solver)
Initial N_2 feed	1E-5
Compressibility	Fully compressible two-phase flow
Turbulence model	Large Eddy Simulation
Grid type	Hexahedral
Mesh resolution	total cells number: 2505255
Time integration precision	First order
Spatial discretization	Second order
Time step	2E-10, CFL:0.12
Inlet Boundary Condition	Pressure, 150 MPa
Outlet Boundary Condition	Pressure, 6 MPa
Chamber condition	Full of N_2, 6 MPa, 900 K, $\rho = 22.07\ kg/m^3$
Wall Condition	Adiabatic
Fuel	N-dodecane, 363 K
Binary Interaction Parameter	0.19
Initial needle lift	500 μm

I. Comparison with experimental results

In this section, the numerical results from the 4EQ-PR-EQ and 4EQ-PR-Wo-EQ models are compared to experimental data. Since no phase equilibrium is considered in the 4EQ-PR-Wo-EQ model, the computational efficiency is much higher than for the 4EQ-PR-EQ model. Therefore, the simulation with phase change were run only for 100 μs, due to limited computational resource. In contrast, the case without phase change has been run more than 230 μs.

a) Jet evolution comparison

During the simulations, no numerical instabilities are encountered for both models. The jet evolution from these two models at early times (up to 89 μs) are illustrated in Figure 6.9. The figures with back illumination are experimental data captured directly from the ECN website [44]. The relevant theory is according to the Mie-scatter theory based on the reference [111]. In the experimental images, the liquid core is identified by liquid volume fraction (LVF) iso-contours at the critical value of 0.0015 [112]. Similarly, this criterion (LVF = 0.0015) is applied to the numerical results from the evaporating 4EQ-PR-EQ model using iso-surfaces, in order to identify the liquid core and its penetration. In contrast, the criterion based on the mixture mass fraction of n-dodecane (Y_{c12h26} = 0.6) refered to the previous studies [15], is preferred in order to compare the 4EQ-PR-Wo-EQ model results with experimental liquid penetrations. This criterion (Y_{c12h26} = 0.6) is applied in Figure 6.9 to show iso-surfaces of the liquid core in the case of the 4EQ-PR-Wo-EQ model.

At the early time sequences (10 μs - 30 μs), the modelling results of both models have demonstrated slightly longer penetration than the experimental value. Since no vapor is generated by the 4EQ-PR-Wo-EQ model, the tip of the jet stay thinner than for the 4EQ-PR-EQ model. Thereby, evaporation seems to trigger earlier radial eddies that lead to higher cone angle and shorter penetration. This trend becomes more evident starting from 43 μs, as may be seen in Figure 6.9. At this moment, the vapor cloud formed in the tip of the jet with 4EQ-PR-EQ model has spread much wider than previous time instant. As time further evolves, both models can estimate the liquid penetration length (about 9 mm) very well compared to experimental value. However, obvious differences are detected in the vapor penetration, as discussed further below based on Figure 6.11 and Figure 6.10.

Even if a good qualitative agreement has been achieved for the liquid penetration, the near-nozzle spray angle seems underestimated compared to the experimental results (Figure 6.9). Indeed, a much slim jet can be observed for both simulation results. One

important reason for that may be ascribed to the initial setting of pressure gradient in the middle of the hole at the simulation beginning. As shown in Figure 6.8, the initial pressure specified in the sac (1500 bar) has proved to be not appropriate because it is far bigger than the actual pressure which should be rather of the order of the chamber pressure (60 bars). This is also the reason why the injection velocity is soared to 650 m/s in less than 15μs, also much higher than the average 600 m/s in the experiment. This may explain the longer liquid penetration in the earlier time sequence as mentioned above. Since the current Spray A injection condition is still in subcritical regime with weak but existent surface tension, the consideration of the primary atomization in the near-nozzle region may remedy the underestimation of spray angle. Other causes may be from the omission of mass diffusion and enthalpy diffusion in the numerical model as shown in the Equation ((3.21), (3.24)). Further study is needed to clarify this problem.

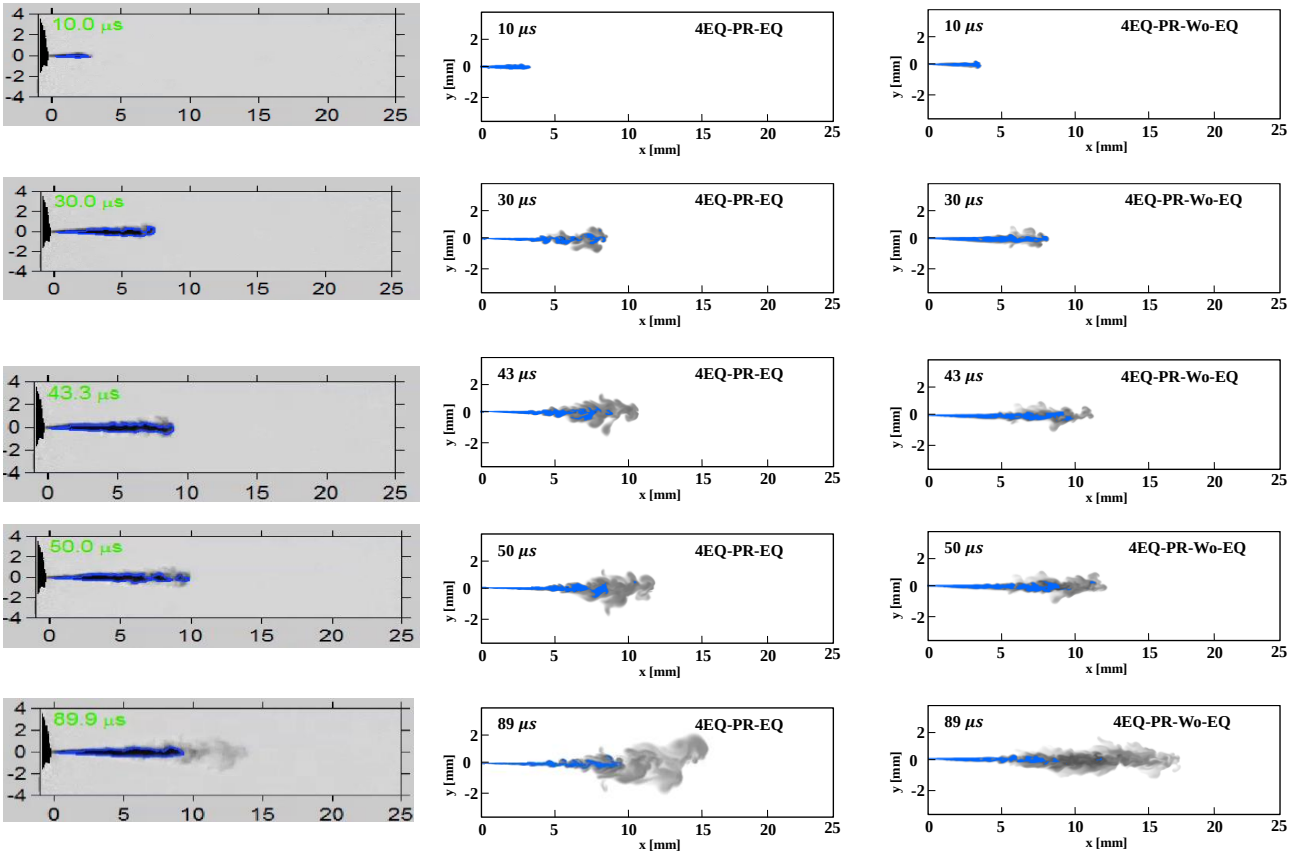

Figure 6.9 Illustration of jet evolution at different time instants. The liquid denoted with blue iso-surface representing the liquid core and penetration is determined with a liquid volume fraction criterion (LVF = 0.0015) for the 4EQ-PR-EQ model results; and a criterion based on mixture mass fraction of n-C12H26 (Y_{c12h26} = 0.6) for the 4EQ-PR-Wo-EQ model results.

b) <u>Jet penetrations and flowrate comparison</u>

As a further quantified validation, the rate of injection (ROI) and liquid and vapor penetration from both models have been compared with experimental data as plotted in Figure 6.11 and Figure 6.10. As mentioned above, affected by the pressure and density initialization (Figure 6.8), the overall penetration length from both models have exceeded the experimental results in the early time (<30 μs). The unappropriated initialization has also led to a much higher mass flow rate compared to the CMT ROI [113] as shown in Figure 6.11. Affected by the initial strong shock inside the nozzle, the mass flux has increased to the maximum value (2.48 g/m3) in less than 15 μs.

After this early injection time, the mass flow rate is approaching the CMT predictions (Figure 6.11), which denotes the pressure variation in the nozzle has resumed to the normal range.

As for the penetration predictions, both models can predict liquid penetration very well since the liquid penetration is largely affected by the ambient condition instead of upper-stream flow. However, as for the vapor penetration, the results from 4EQ-PR-EQ model can basically have a good agreement in the early 100 μs. It is worth noting that a 10 μs delay has been adopted in Figure 6.10 to adjust the initial penetration slopes and have fair comparisons. Another noting point is that the penetration length estimated by using the vaporous n-$C_{12}h_{26}$ in 4EQ-PR-EQ model can have a very close result with the predictions by employing the criterion of mixture mass fraction (Y_{c12h26} = 0.015). Whereas, significant deviations are detected for 4EQ-PR-Wo-EQ after 80 μs by using the criterion of mass fraction. Since no real vapor is generated with 4EQ-PR-Wo-EQ model, the empirical estimation by using mixture mass fraction appears to be not suitable with current model. Indeed, the liquid length predicted by LVF equalling 0.0015 in 4EQ-PR-Wo-EQ model has presented the same length as the vapor penetration predicted by using the criterion (Y_{c12h26} = 0.015). This coincidence implies the so-called 'vapor' in the 4EQ-PR-Wo-EQ can never represent the real vapor as generated in the phase change model. The overestimation of vapor penetration has also been reported in recent simulation of the spray A modelling with phase equilibrium model [32] in which they have attributed this deficiency to the shortcoming of PR EoS in predicting density. Some researcher has attributed this to the under-prediction of turbulent mixing in radial direction which induces an oversupply of axial momentum which convects vapor downstream faster [36]. In current study, the causes can be attributed mainly to the unappropriated initialization of pressure distribution inside the nozzle, as noted above.

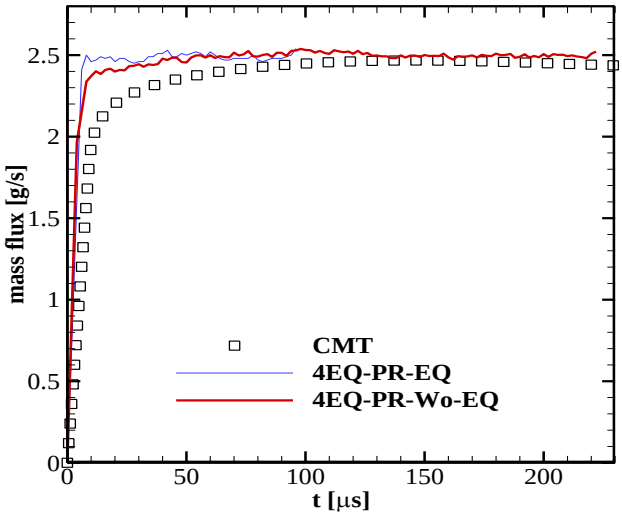

Figure 6.10 Illustration of rate of injection (ROI) from 4EQ-PR-EQ, 4EQ-PR-Wo-EQ models, as well as the predictive data by using the injection rate model [113]**.**

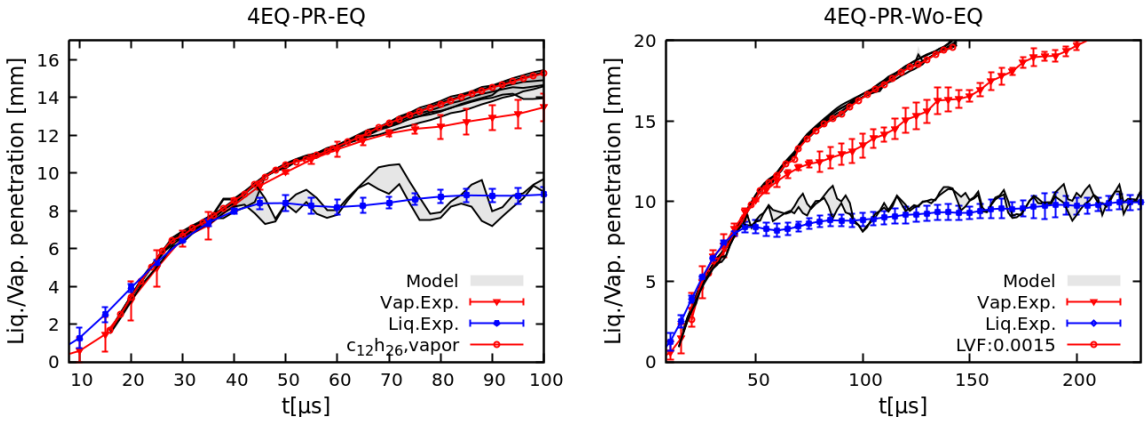

Figure 6.11 Illustration of liquid and vapor penetration for 4EQ-PR-EQ and 4EQ-PR-Wo-EQ models compared to experimental data from ECN website (https://ecn.sandia.gov/bkldaal4liquid/), referred to in [112], [114] The evaluation of vapor penetration is based on the mass fraction of n- $C_{12}H_{26}$ (Y_{c12h26} = {0.015, 0.01, 1e-5}) for 4EQ-PR-Wo-EQ model. The penetration length determined by vaporous n-$C_{12}H_{26}$ is also evaluated for 4EQ-PR-EQ model. The evaluation of liquid penetration is based on the liquid volume fraction with a critical value of 0.0015 (LVF = 0.0015) for 4EQ-PR-EQ and the mass fraction of n-$C_{12}H_{26}$ at the critical values of 0.6 (Y_{c12h26} = 0.6) for 4EQ-PR-Wo-EQ model. The penetration length determined by the liquid volume fraction of 0.0015 (LVF = 0.0015) is also evaluated for 4EQ-PR-Wo-EQ model.

c) Mixture mass fraction and velocity comparison for 4EQ-PR-Wo-EQ model

More validations concerning mixture mass fraction of n-$C_{12}H_{26}$ and actual velocity in radial direction are performed for 4EQ-PR-Wo-EQ model as shown in Figure 6.12. The instantaneous LES results of mass fraction are obtained within the time interval of 156-230 μs. A good agreement can be achieved in the amplitude of mass fraction. Some deviations are still detected in the cone angel as expected. The velocity distribution at the time interval of 212-222 μs are obtained and compared to the experimental average velocity at an instant of 217 μs. The overall velocity distribution has an excellent agreement with experimental results. These results may imply the evaporation will not seriously affect the material and velocity distribution in the radial direction.

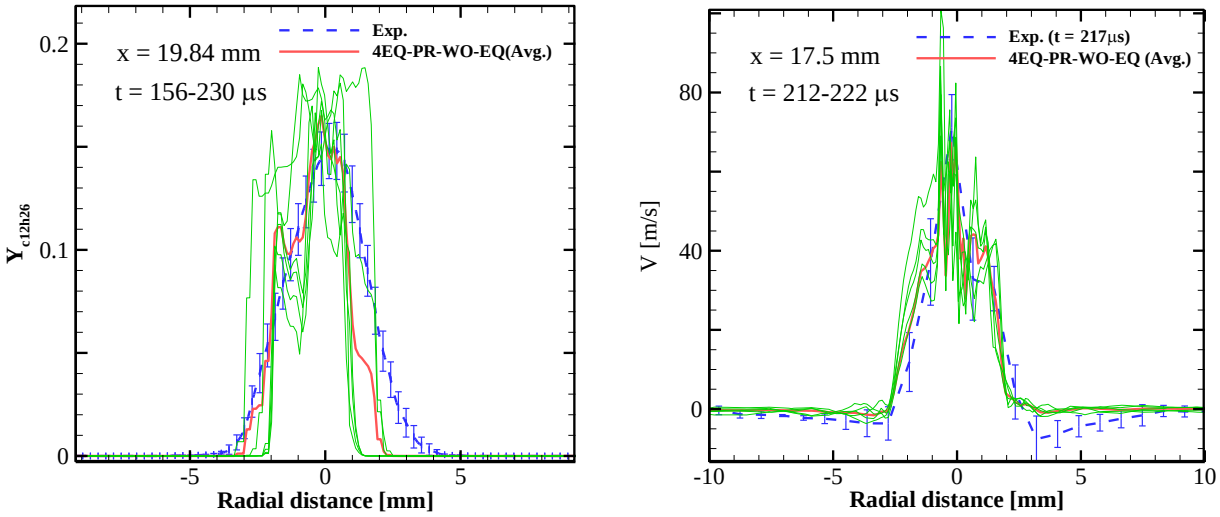

Figure 6.12 Validations of mixture mass fraction (Left side) and velocity (Right side) with experiments at an axial distance of 19.84 mm and 17.5 mm from the nozzle exit respectively. The instaneous LES results (green solid line) and the average value (red bold line) are from 4EQ-PR-Wo-EQ model. The experimental data (blue dash line) are referred to [114], [115].

II. Thermodynamics analysis

The T-$_X$ diagram of n-$C_{12}H_{26}$ and N_2 at the chamber pressure 60 bar is plotted in Figure 6.13. The frozen temperature T_F and equilibrium temperature T_E are also

calculated based on PR EoS. The scattered points are obtained from current numerical simulations at time 50 μs. The mixture temperature distribution from equilibrium 4EQ-PR-EQ model can follow very well the equilibrium temperature T_E in almost the whole N_2 concentrations range. Except a small temperature deviation that may be seen in the single-phase liquid region where the N_2 mole fraction is smaller than 5%. Indeed, since the basic T_F and T_E lines are calculated with the initial fuel temperature of 363 K, the lower temperature detected in the simulations has proved to be some degrees lower. As a matter of fact, the fuel has gone through a cooling stage in the hole before entering the chamber, which will be confirmed in the following section. Even if phase change is not considered, the trend of mixture temperature evolution from 4EQ-PR-Wo-EQ model can still correlate well with equilibrium temperature, particularly when the N_2 mole fraction is smaller than 0.6. Evident deviations start at N_2 mole fraction higher than 0.75, where equilibrium temperature differs from frozen temperature as shown in Figure 6.13. Indeed, a slightly lower temperature is detected by 4EQ-PR-Wo-EQ model near the two-phase vapor side. This temperature differences further enlarge with increasing N_2 mole fraction up to the two-phase vapor side limit. After transiting to single-phase gas region (with more than 90% N_2), the temperature profile resumes to the equilibrium trend. One noting point is that even only the internal energy is conserved in the flow system, no evident error is detected in the temperature prediction by these two models. The other intriguing point is the similar temperature predicted by these two models even inside the two-phase zone which may enlighten us to develop a simplified model which can autonomously transfer between the evaporation regime and single-phase mixing regime at prescribed ambient condition. Thus, the phase change phenomena will be only applied to the effective zone and a significant computational time saving could be expected thereby.

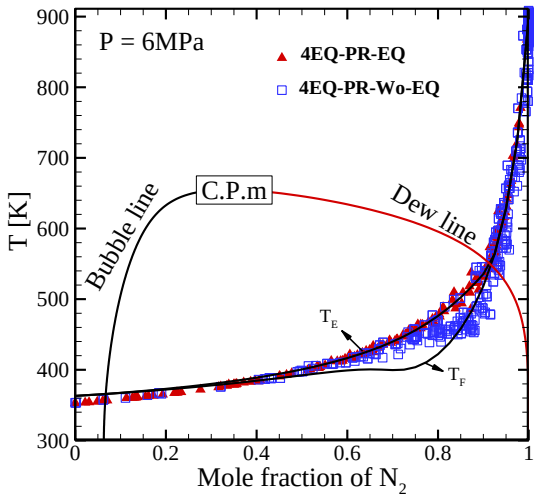

Figure 6.13 T-$_X$ diagram of n-$C_{12}H_{26}$ and N_2 system at a pressure of 60 bar. T_E denotes the equilibrium temperature between the mixture. T_F symbols the frozen temperature or adiabatic mixing temperature. The red scattered points are obtained from CFD modelling with 4EQ-PR-EQ model at t = 50 μs. The blue scattered points are obtained from CFD modeling with 4EQ-PR-Wo-EQ model at t = 50 μs.

Except its computational time consumption issue, the VLE model can provide abundant and accurate information related with phase properties. As aforementioned, one important step of VLE computation is to determine phase state. By solving TPD functions, the real phase number and state can be verified. The study here has adopted three integers to represent phase state (TPD = 0: single-gas phase; 2: two-phase; 1: single-liquid phase) [97]. To get a knowledge of the real fluid state during the jet developing, an iso-surface of TPD value equalling 2 (two-phase region) is presented in Figure 6.14. As shown in this Figure, the jet starts evolving from the exit of the orifice with single-liquid state corresponding to almost pure liquid n-dodecane, and forms an intact liquid core. Then as the jet penetrates further, high temperature ambient gas is entrained to heat the jet, which has naturally increased the evaporation and the formation of a two-phase region before the final vapor jet, as shown in Figure 6.14 (a). The mole fraction of vapor (ψ_v, including n-$C_{12}H_{26}$ + N_2) has also increased gradually from the liquid core to the downstream spray (Figure 6.14 (b)). As more N_2

is mixed into the jet, the mole fraction of n-$C_{12}H_{26}$ (z_{c12h26}) has witnessed a stable decrease from liquid core (Figure 6.14 (c)). The mixture sound speed as depicted in (Figure 6.14 (d)) computed with Wood formula (Equation (3.35)) [93] presents an obvious decrease from single-liquid phase region (~1100 m/s) to the two-phase region (~250 m/s), and then slightly increases in the leading vapor jet region. Particularly, the lowest sound speed is attained in the region where the mole fraction of n-$C_{12}H_{26}$ is around 0.5, in agreement with the Wood formula, as depicted in Figure 6.14 (e, f)). The relatively low speed of sound is obtained in the region ($0.1 < \alpha_{gas} < 0.9$) which corresponds to the two-phase region.

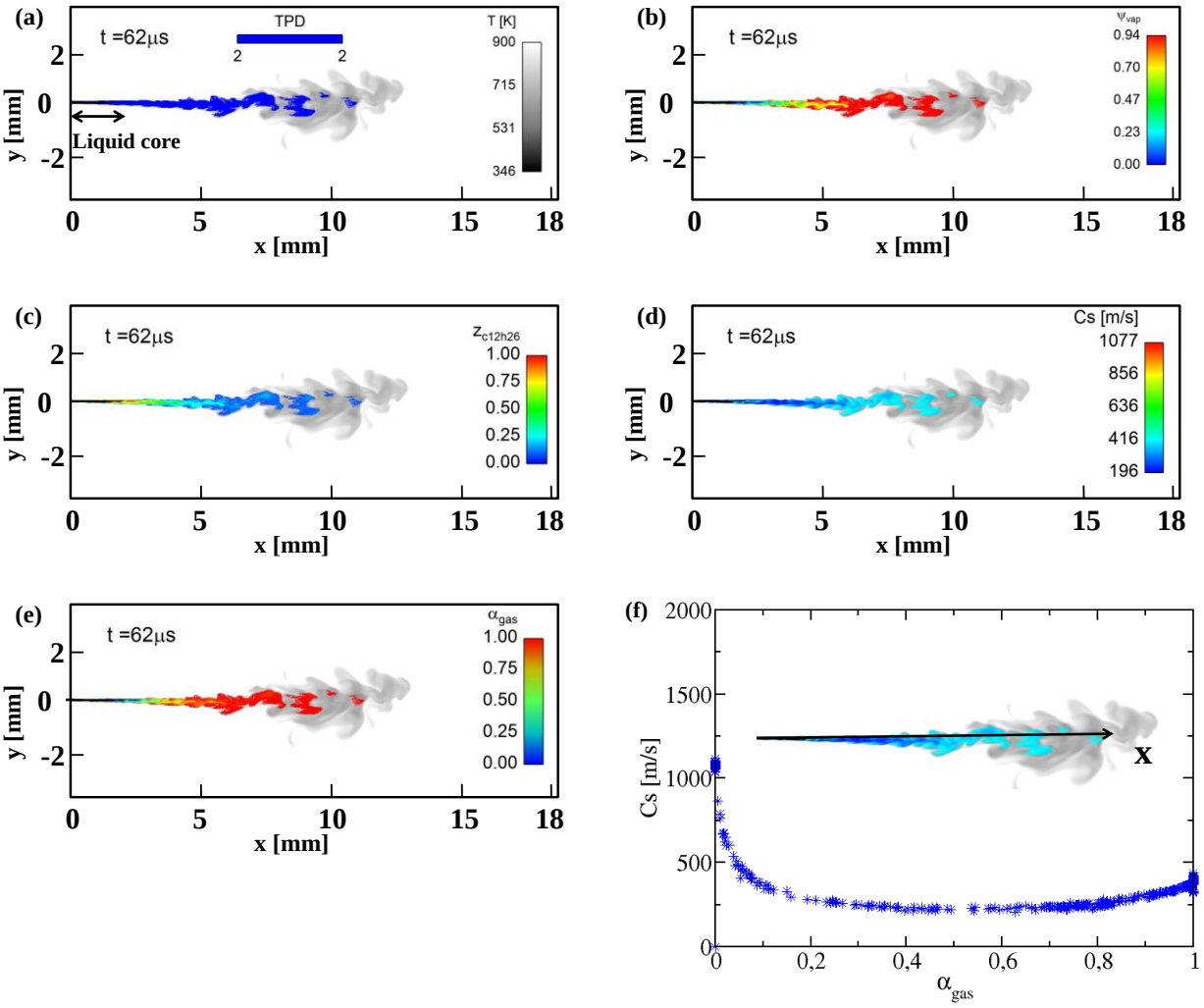

Figure 6.14 (a) depicts two-phase region in the jet by using an iso-surface of TPD = 2 at t = 62 μs.(b) illustrates the evolution of vapor mole fraction (ψ_{vap}) in the two-phase region at t = 62 μs.(c) illustrates the variation of mole fraction of n-dodecane (z_{c12h26}) in the two-phase region at t = 62 μs. Figure (d) illustrates the variation of speed of sound (Cs)in the two-phase region at t = 62 μs. (e) illustrates the evolution of volume fraction of gas (α_{gas}) (N_2+ $C_{12}H_{26}$) in the two-phase region at t = 62 μs. (f) demonstrates the variation of the mixture sound speed (Cs) with the gas volume fraction (α_{gas}) (including N_2 + $C_{12}H_{26}$) in the axial direction of the jet as depicted with the black arrow. The background contours in all pictures is the temperature field with the legend shown in (a).

With phase equilibrium model, the density of each component at any phase is also available. In current study, the mixture density is computed with $\rho = \alpha_g \rho_g + \alpha_l \rho_l$. The maximum density (646 kg/m3) is obviously in the liquid core where the liquid volume fraction approaches one (Figure 6.15 (a)). As more N_2 is mixed into the downstream jet, the mixture density of the jet decreases significantly. In Figure 6.15 (c), the mass fraction of any component in each phase ($Y_{p,k}$) is defined as the ratio of specific density with respect to mixture density $Y_{p,k} = \frac{\alpha_p \rho_{p,k}}{(\sum_k \alpha_p \rho_{p,k})}$. Thereby, the mass fraction of vaporous dodecane in Figure 6.15 (d) represents the percentage of generated vaporous dodecane related with the total mixture density. Since the vaporous dodecane is from the phase equilibrium computation, the location where the vaporous dodecane peaks certainly corresponds to the maximum value of overall vapor molar fraction (compare Figure 6.15 (d) and Figure 6.15 (b)). The generated vapor is accumulated in the jet front where the mass fraction of vaporous dodecane reaches 30%. The maximum specific density of vaporous dodecane is around 20 kg/m3, as shown in Figure 6.15 (d). Figure 6.15 ((e), (f)) present the variation of dissolved N_2 in the jet. Since the chamber pressure is very high (~60 bar), the dissolved N_2 part becomes non-negligible. The mass fraction of dissolved N_2 reaches 1% mostly located in the liquid core zone where the N_2 specific density arrives to 6 kg/m^3.

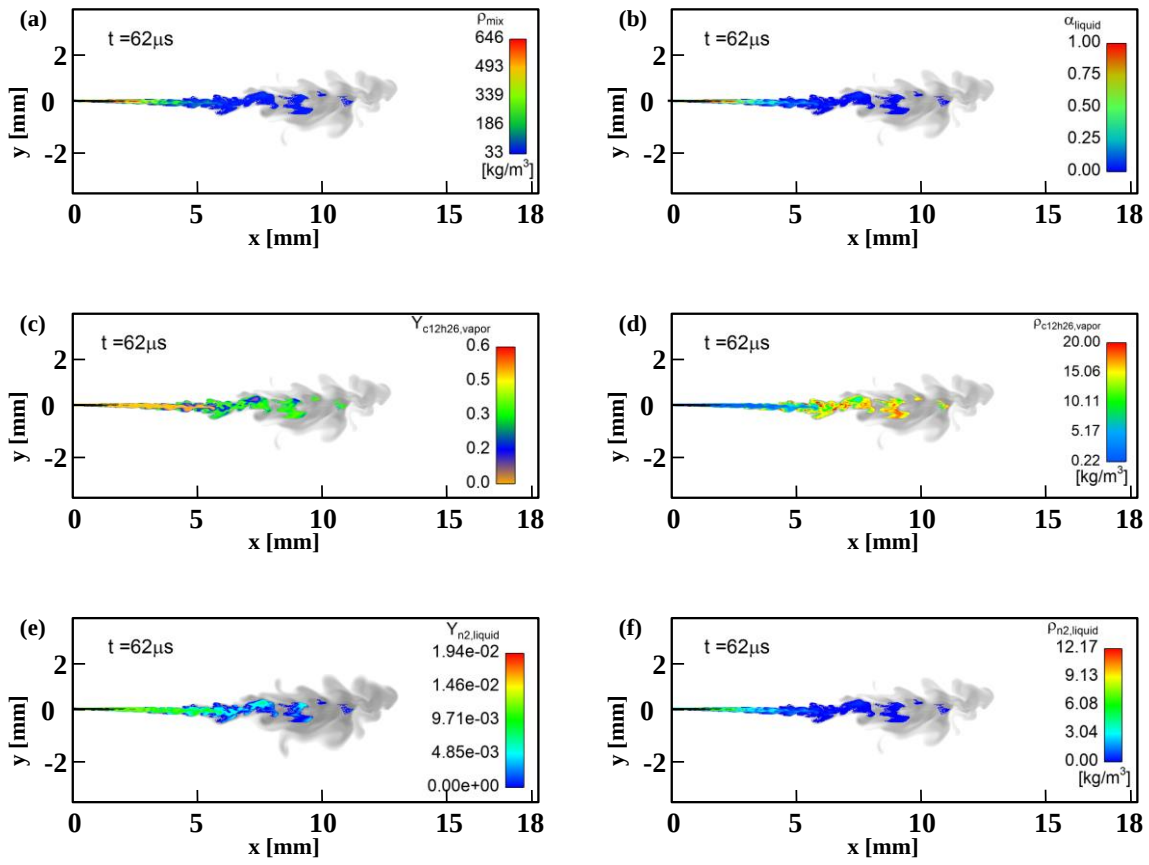

Figure 6.15 (a, d, f) depict the density of mixture fluid (ρ_{mix}), vaporous dodecane ($\rho_{c12h26,vapor}$) and N_2 in liquid phase($\rho_{n2,liquid}$) in the two-phase zone of the jet at the time of 62 μs, respectively. (b, c, e) demonstrate the evolution of volume fraction of liquid phase (α_{liquid}), mass fraction of vaporous n-$C_{12}H_{26}$ ($Y_{c12h26,vapor}$)and dissolved N_2 in the liquid phase ($Y_{n2,liquid}$) in the two-phase region at the time of 62μs, respectively. The background contour in all the pictures is the temperature field with the legend in Figure 6.14 (a).

Affected by the in-nozzle flow, a mushroom head is detected in the front of the jet at t = 6 μs as shown in Figure 6.16 (d). As mentioned above about the initialization of the modelling, some gas is assumed to be existent in the orifice at the beginning. Once the injection is started, the gas from the orifice will come out first and then the liquid which has induced the formation of mushroom head. With the jet evolving with time, the mushroom head has deformed after the mixing of N_2 (Figure 6.16 (d, f)). A strong shock is expected as the jet enters the chamber with the pressure gradient varying

from 1500 bar to 60 bar which explains the high pressure zone (70E5-80E5) in the stagnation point of the jet as shown in Figure 6.16 (a). In addition, obvious pressure oscillations can be observed in the shear layer of the jet. A minimum pressure lower than 40 bar can be seen in the pressure fields. These pressure oscillations may lead to the local pressure lower than pure n-dodecane critical pressure (18 bar). Thus, this induces the appearance of phase change which to some extent denotes the limitation of the model without using VLE. The maximum pressure can reach 100 bar at t = 60 µs. Even with high pressure gradient, the whole simulations for 4EQ-PR-EQ and 4EQ-PR-Wo-EQ have proceeded smoothly without meeting any instability

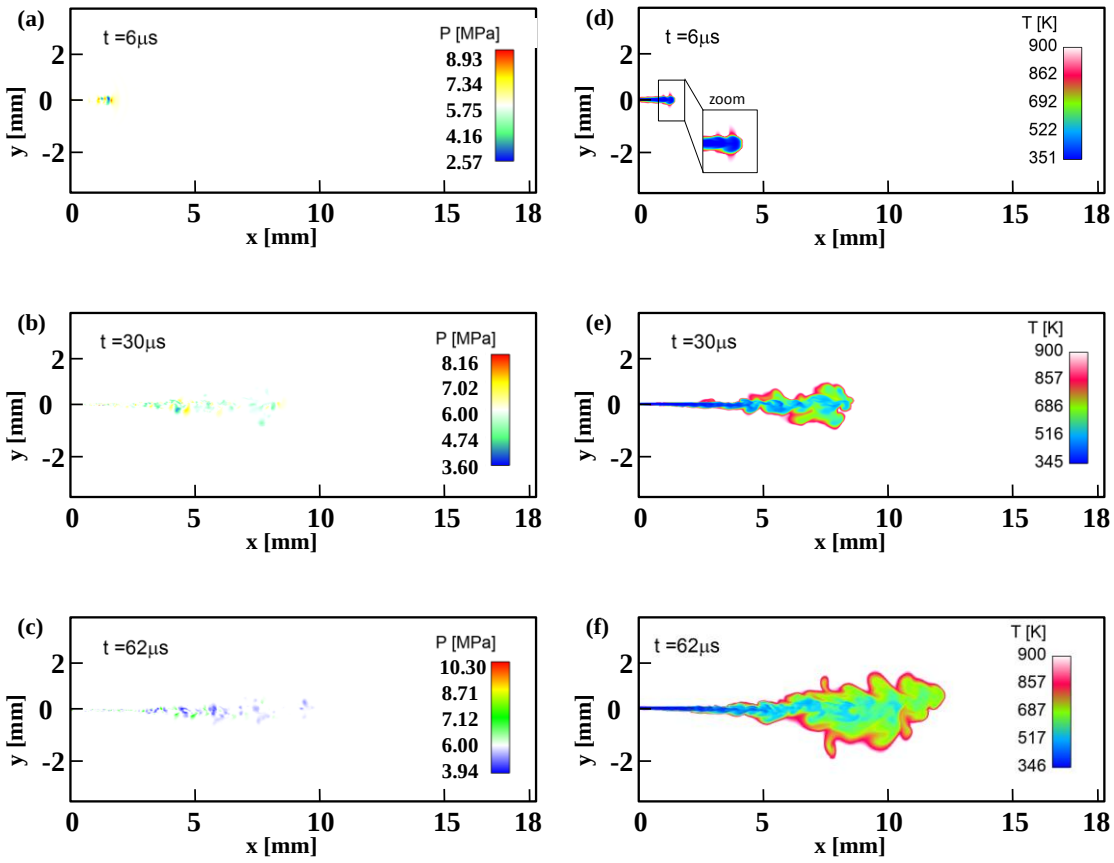

Figure 6.16 Evolution of temperature and pressure at an early time sequence from CFD modelling with 4EQ-PR-EQ model. Fig.(a, b, c) denotes the pressure variation and Fig.(d, e, f) illustrate the evolution of temperature variation.

The important influence of in-nozzle flow on the downstream spray development has been widely recognized in the community [35],[37]. Thereby, to have a clear idea about the instantaneous flow variation inside the sac and orifice, the evolution of pressure, temperature, compressibility factor and density stretching from the sac up to chamber (Figure 6.17) are illustrated in Figure 6.18 (a, b).

Firstly, an instantaneous pressure drop is seen inside the orifice. The strong shock has brought in rapid increase of velocity from 0 m/s to 650 m/s in less than 15 μs. The sudden increase of velocity also induces some cooling effect on the fuel (~10 K) which can be observed in the variation of temperature profile Figure 6.18 (a).This also explains the smaller temperature in the single-liquid phase region of the T-x diagram, as illustrated in Figure 6.13. One noting point is the evolution of compressibility factor. Since it is the repulse force that dominated among the molecular at high pressure condition, the compressibility factor also far exceeds 1 even in pure liquid condition as shown in Figure 6.18 (b). From the sac to the chamber, the fluid has been through the transition from the extreme dense liquid to less dense liquid which corresponds to the variation of the compressibility factor from 12 to 0.6. Accordingly, the strong expansion has brought in a reduction of density by around 40 kg/m^3. The significant variation of compressibility factor and density imply the compressibility of liquid is definitively not negligible in high pressure injection simulation.

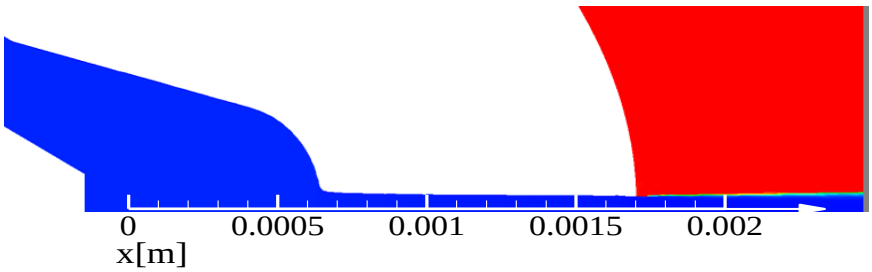

Figure 6.17 Demonstration of the axial direction from the sac to the chamber.

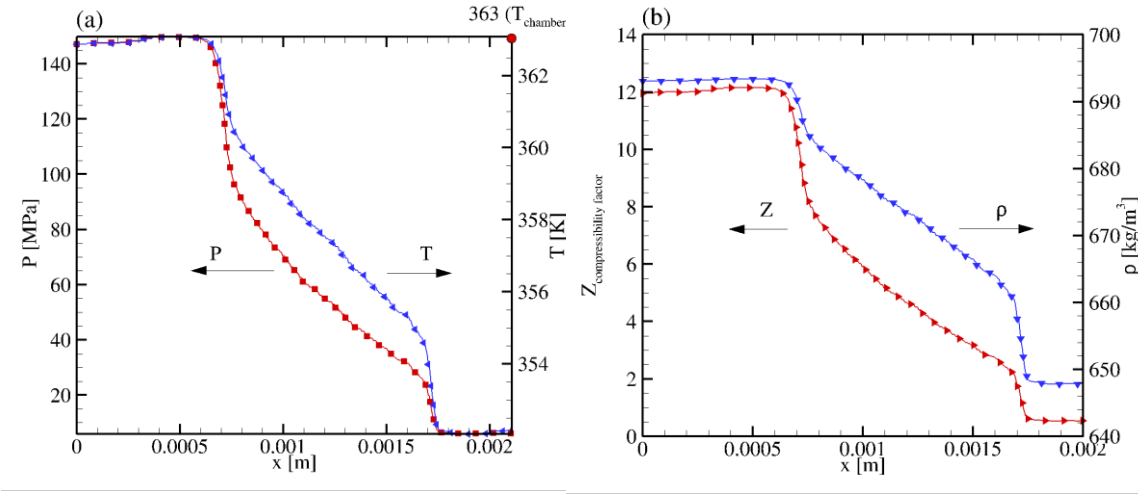

Figure 6.18 (a) denotes the evolution of pressure and temperature from the sac to the chamber. (b) depicts the variation of compressibility factor and density from the sac to the chamber.

III. Parametric study

A series of parametric study includes elevated temperature and pressure are stated in this section. Two cases are accounted for in which the same density (~22 kg/m3) is kept as previous simulations, along with a variant pressure and temperature as listed in Table 6.3. Since the computation has very high demand in CPU resource, both cases run not more than 80 μs. The early jet evolution for these two cases have been displayed in Figure 6.19 and Figure 6.20.

Table 6.3 Operating conditions for other Spray A modelling.

Case No.	T_a [K]	P_a [MPa]	ρ_a [kg/m^3]
1	1200	8	22.04
2	700	4.6	22.79

Both cases can achieve a relatively good agreement in the prediction of liquid penetration with experimental results. With higher temperature and pressure in the chamber, the liquid penetration has shortened (case1) compared to the low

temperature and pressure case 2. The cause is due to less evaporation appearing in case2 as proved in the contour of the mass fraction of vaporous dodecane (Figure 6.21). In high temperature situation, the area of the localized mass fraction of vaporous dodecane locating at the range 0.3-0.5 is obviously larger than the low temperature case (Figure 6.21 (b, d)). This also confirms the relatively short liquid penetration length for case1. In addition, the spray angle of high temperature case is also narrower than low temperature case which implies strong evaporation can bring potential cooling effect on the jet [114]. Since the initialization is similar with previous simulation, the length of vapor penetration also exceeds the experimental value as reported in previous case.

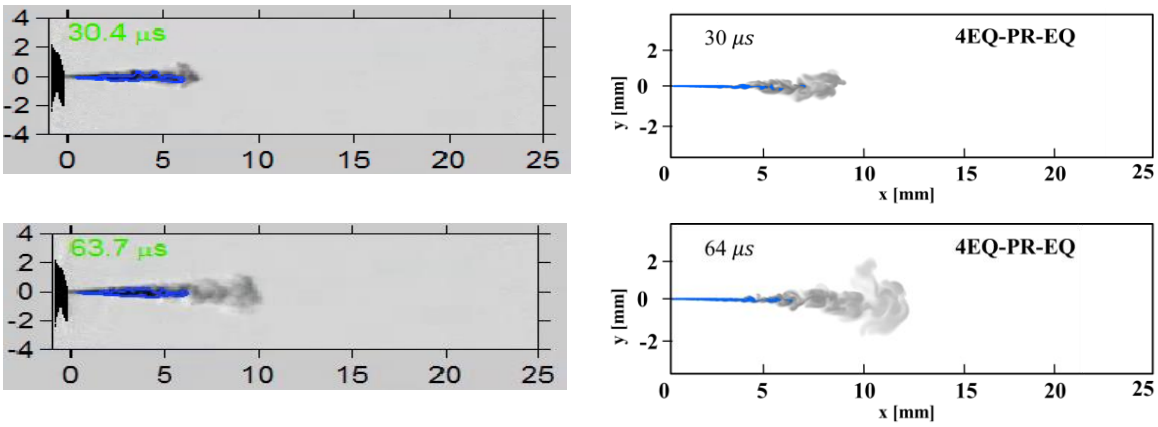

Figure 6.19 Illustration of early jet evolution for case 1 (Ta = 1200 K, Pa = 8 MPa). The liquid penetration length marked with blue iso-contour is presented with the criterion of LVF ={0.0015}. The left column is the experimental pictures snapped directly from ECN website (https://ecn.sandia.gov/dbi675/). The right column corresponds to the results of 4EQ-PR-EQ model.

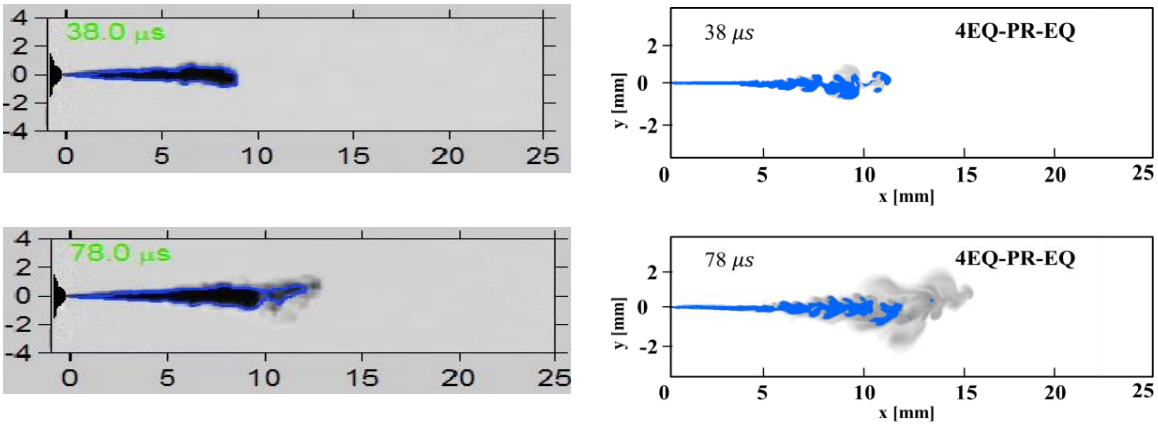

Figure 6.20 Illustration of early jet evolution for case 2 (Ta = 700 K, Pa = 4.6 MPa). The liquid penetration length marked with blue iso-contour is presented with the criterion of LVF = {0.0015}. The left column is the experimental pictures snapped directly from ECN website (https://ecn.sandia.gov/dbi675/). The right column corresponds to the results of 4EQ-PR-EQ model.

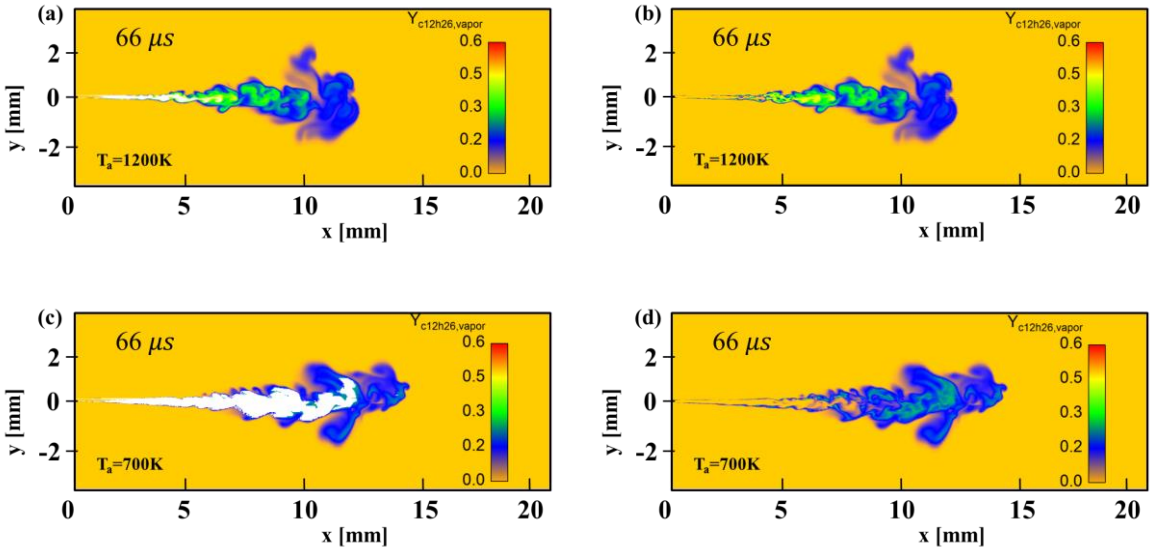

Figure 6.21 Demonstration of the mass fraction of vaporous dodecane ($Y_{c12h26,vapor}$) for case 1 (Fig. (a, b)) and Case2 (Fig. (c, d)) at a time instant of 66 μs. The two-phase zone is presented with the iso-volume of TPD equalling 2 as shown the white zone in Fig. (a, c).

6.3 Chapter Conclusions

In this chapter, the 4EQ-PR model has been used to model the injection process at supercritical and transcritical condition. To be more specific, the model is firstly used to simulate the injection with a moderate pressure gradient from the inlet to outlet to prove its capability in modelling the phase change in subcritical condition as well as handling the strong gradient at transcritical condition. Then the 4EQ-PR model is employed to simulate the ECN Spray A injector including the complex in-nozzle flow with the assumption of phase change and without phase change process. The obtained modelling results have been compared to experimental data and several conclusions are drawn as following:

1) The initialization of in-nozzle flow plays a significant role in the early jet development, cone angle and therefore on vapor phase penetration.
2) A good agreement has been achieved for the liquid penetration with both the phase change model and no phase change model.
3) Significant deviations are detected in the prediction of vapor penetration for the model without considering phase change with the conventional mass fraction based criterion which may be attributed to the unappropriated initialization.
4) Both models have underestimated the spray angle which may be caused by the non-fully resolved shear stress layer and the omission of enthalpy diffusion and mass diffusion terms in transport equation. Since the current Spray A injection condition is still in subcritical regime with weak but existent surface tension, the consideration of the primary atomization in the near-nozzle region may remedy the underestimation of spray angle. Further study is needed to clarify this problem.
5) The error caused by the non-conservative energy has not adversely affected the temperature prediction during CFD modelling.

6) The extreme large variation of liquid compressibility factor and density in the nozzle implies the importance of considering the compressibility of liquid during injector simulations.
7) Higher chamber temperature can induce stronger evaporation process which correspondingly diminishes the spray angle due to the cooling effect.

7 Summary, Conclusion and Future work

7.1 Summary and Conclusion

In this thesis, two real-fluid fully compressible two-phase flow models based on Eulerian approach with the consideration of phase equilibrium theory based on Peng-Robinson EoS have been developed and validated.

In particular, to handle the complex phase change behaviour at subcritical condition, as well as the non-linear variation of thermal properties at HTHP condition, a phase equilibrium model based on real fluid EoS has been developed in the current study. The phase equilibrium solver includes a vapour-liquid equilibrium (VLE) computation and a UV flash (Isochoric–Isoenergetic flash). The vapour-liquid equilibrium computation contains the premier stability test and the ensuing phase split computation (TP flash). The thermodynamic solver has been coupled with the fully compressible two-phase flow 6-Equation and 4-Equation systems which are the simplified versions of the classical non-equilibrium 7-Equation model. The coupled two equation systems have been employed to conduct a series of academic tests involving phase change (evaporation, condensation, etc) behaviours. Then, the fully compressible flow solver with phase change model has been used to model the cavitation in a real 3D nozzle to investigate the effect of dissolved N_2 on cavitation inception and development. At last, the solver is employed to model the diesel injection at HTHP condition based on ECN spray A injector. Several conclusions are drawn from these studies,

1) No significant differences are detected in the comparison of 1D academic tests between the 4-Equation and 6-Equation systems. Both models are able to predict the phase change behaviours very well. However, 4-Equation system is more efficient than 6-Equation model.
2) The classical spurious oscillations problem indeed exists for the 4-Equation system. This problem is controllable through refining the mesh.
3) Even only internal energy instead of total energy is transported in the flow system, the error brought by the energy loss is proved to be negligible which can be seen in the temperature prediction in the 3D injection modelling.
4) By using the phase equilibrium model based on real fluid EoS to model the cavitation, the solver is able to predict the inception of cavitation or nucleation process, as well as capable of modelling the effects of dissolved N_2 on the cavitating flows.
5) With the fully compressible Eulerian model, the solver is able to predict the variation of density, temperature and compressibility factor inside the injector and also the continuous modelling from the upper-stream in-nozzle flow to downstream injection process and mixing.
6) The efficiency of the Eulerian based model is limited by the extreme small mesh resolution. When applied with phase equilibrium model based on PR EoS, the computational efficiency is reduced by the iteratively root searching strategy.
7) At high pressure condition, the deficiency of PR EoS in predicting density and speed of sound may affect the accuracy of computation.
8) Overall, the phase equilibrium model based on real fluid EoS is able to predict the phase change behaviours and thermal properties at high temperature with reasonable accuracy.
9) Finally, the developed models in this thesis are able to deal with subcritical and supercritical flows simultaneously, as initially requested.

7.2 Future work

1) More work needs to be done to improve the computational efficiency of real fluid model. The ideal method is by using the tabulation method. Potential challenges related with this method is to realize the autonomous refining in the phase boundary.
2) Continue the cavitation nozzle case modelling with high efficiency model until to the steady state. More explorations are essential to unravel the connections between the cavitation and turbulence.
3) Add a primary atomization model, during the injection modelling to improve the prediction of near nozzle spray angle.
4) Explore more efficient algorithms to improve the computational efficiency in the phase boundary.
5) Use more sophisticated EoS (BWR, PC-SAFT, etc) in order to improve density and sound speed accuracy at high pressure condition.
6) Apply the 6EQ-PR model to the modelling of high pressure injection to investigate the effect of mechanical and thermal non-equilibrium on the injection process.
7) Simulate more realistic injection process with the consideration of needle movements.

List of Figures

liquid ($Cs^2 > 0$) in the left side, unstable fluid ($Cs^2 < 0$) in the middle zone and the metastable gas ($Cs^2 > 0$) in the right side. The unstable region is limited by the spinodal curves (red dashed line).

Figure 4.1 1D shock tube at time 1 ms. The computational results in Figures (a, b, c, d) (blue line: 6EQ-PR, red line: 4EQ-PR) are compared with results (bold black dashed line: 4EQ-SG) from Chiapolino et al. [91]. The computations were conducted with 100 cells. The thin dashed lines are the initial conditions.

Figure 4.2 1D shock tube at time 1 ms. Figures (e, f) illustrate the results of 6EQ-PR with different mesh resolution (100 cells and 1000 cells).

Figure 4.3 1D shock tube at an instant of 1 ms. The computational results (blue line: 6EQ-PR, red line: 4EQ-PR) are compared with results (bold black dashed line: 4EQ-SG) from Chiapolino et al. [91]. The thin dashed lines are the initial conditions. The computations were conducted with 100 cells and a CFL equalling 0.2.

Figure 4.4 1D shock tube at the time of 1 ms. The computational results of 6EQ-PR (blue line) are compared with results from 4EQ-PR (red lines). Both computations were conducted with 100 cells and a CFL number equals to 0.2.

Figure 4.5 1D two-phase shock tube operated with spray A conditions ($P_{inject} = 150\ MPa,\ T_{fuel} = 363\ K,\ P_{ambient} = 6\ MPa,$

$T_{ambient} = 900\ K$) using the 4EQ-PR model. (a, b, c, d) denotes the evolution of pressure, density, speed of sound and mass fraction of vaporous dodecane at an instant of 0.2 ms with a varied mesh resolution from 1 mm, 0.2 mm to 0.02 mm.

Figure 4.6 1D Double expansion tube at an instant of 3.5 ms. The computational results of 6EQ-PR (blue line) are compared with the results from 4EQ-PR (red lines). Both computations were conducted with 100 cells and a CFL number equals to 0.2.

Figure 4.7 1D transcritical shock tube at an instant of 0.05 ms. The computational results (solid line with symbols) are compared with results from Ma. [51] (dashed bold line). The present work computations were conducted with 1000 cells and a CFL number equaling 0.1. The reference results are done with 50000 grid points.

Figure 4.8 1D advection tube at time 10 ms. The relative errors of pressure, temperature and velocity compared with initial value are illustrated at (a, b, c) respectively. The comparison of density at an instant of 10 ms and 0 ms is plotted in figure (d). The computations were conducted with 1000 cells and 2000 cells and a CFL number equaling 0.1.

Figure 4.9 The percentage of energy and mass variation related with initial time in the 10 ms. The computations were conducted with 1000 cells and 2000 cells and a CFL number equaling 0.1.

Figure 4.10 Comparisons of heat capacity at constant pressure and density between PR EoS and NIST in a temperature range of 300-1200K and at constant pressure of 60 bar. Illustration of different thermodynamics schemes for the three cases in Table 4.3.

Figure 4.11 Case 2 results: Results of 1D advection tube with subcritical condition at an instant of 5 ms. The relative error of pressure and velocity compared with initial value are illustrated at (a, b) respectively. The comparison of density at an instant of 5 ms and the initial time is plotted in Figure (c). The percentage of energy variation during the 5 ms is plotted in Figure (d). The computations were conducted with 1000 cells and 10000 cells and a CFL number equaling 0.1.

Figure 4.12 Case 3 results: Results of 1D advection tube with transcritical condition at an instant of 5 ms. The relative error of pressure and velocity compared with initial value are illustrated at (a, b) respectively. The comparison of density at an instant of 5 ms and the initial time is plotted in Figure (c). The percentage of energy variation during the 5 ms is plotted in Figure (d). The computations were conducted with 1000 cells and 10000 cells and a CFL number equaling 0.1.

Figure 4.13 Case 4 results: Results of 1D advection tube with supercritical condition at an instant of 5 ms. The relative error of pressure and velocity compared with initial value are illustrated at (a, b) respectively. The comparison of density at an instant of 5 ms and the initial time is plotted in Figure (c). The percentage of energy deviations

during the 5 ms is plotted in Figure (d). The computations were conducted with 1000 cells and 10000 cells and a CFL number equaling 0.1.

Figure 5.1 (a) The variation of vapor mole fraction with the feed of N2 at T = 293 K; P = 1-10 bar. (b) denotes the amount of dissolved N2 at the pressure range of 0.01-10 bar.

Figure 5.2 Evolution of saturation pressure(bubble pressure) with varying N_2 concentration Y_{N_2}={0, 2E-3, 2E-4, 2E-5, 2E-6, 2E-7} for n-$C_{12}H_{26}$-N_2 (Left) and Viscor-N_2 (Right) systems at a temperature range of 293 K-670 K.

Figure 5.3 (a) Configuration of 3D geometry. (b) Illustration of mesh distribution in one clip plane.

Figure 5.4 Configuration of $1/8$ geometry and mesh refining zone with total 25982 cells and minimum grid resolution of 6.06 μm.

Figure 5.5 Configuration of $1/2$ geometry and mesh refining zone with 560425 total cells number and minimum grid resolution of 5 μm.

Figure 5.6 Results of the 2D cavitating nozzle.

Figure 5.7 Thermodynamics analysis of properties variation in the nozzle. (a) denotes the variation of void fraction with $Delta\_P$ at central axis (r/R = 0) and near wall direction (r/R = 0.99), $Delta\_P =$ (10 bar − P)10 bar; (b) denotes the variation of vapor molar fraction of fuel and nitrogen with $Delta\_P$ at near wall direction (r/R = 0.99); (c) denotes the variation of vapor molar fraction of fuel and nitrogen with the reduction of pressure at T = 293 K and $YN2$= 1E-3; (d) denotes the variation of pressure and temperature at central axis (r/R = 0) and near wall direction (r/R = 0.99); (e, f) illustrate the variation of density and heat capacity with dissolved nitrogen at central axis (r/R = 0) and near wall direction (r/R = 0.99) respectively.

Figure 5.8 Demonstration of radiography direction for the post-processing of LES modelling results. X direction is the rotating view based on Y direction.

Figure 5.9 Comparison of radiography contour for integrated void fraction between X-ray experimental data and LES simulation results in which the experimental data

are adapted from the ref. [104] and the modelling results are computed based on the line integration of volume fraction of gas (α_g) for the non-degassed case ($Y_{N2} = 2E{-}5$, t = 0.36 ms) and degassed gas case ($Y_{N2} = 2E-6$, t = 0.44 ms).

Figure 5.10 Quantified comparison between experimental data [104] and instantaneous LES results. The data for the dissolved gas case and degassed gas are collected at an time instant of 0.36 ms and 0.44 ms respectively.

Figure 5.11 Demonstration of the effect of N2 on cavitation inception and developing process. The cavity is presented with the iso-surface of gas volume fraction equalling 0.5 (α_g = 0.5).

Figure 5.12 Demonstration of the effect of N2 on the velocity contour at the location of cavitation inception.

Figure 5.13 Demonstration of void fraction based on varied iso-surface of volume fraction of gas (α_g) at the time instant of 0.36 ms.

Figure 5.14 Demonstration of nucleation and cavitation development within the time intervals of 0.14 ms. The nucleation and cavitation zones are presented by iso-surface of varying void fraction at different time. The contour in the iso-surface represents the volume fraction of N2.

Figure 6.1 (a) is the 3D geometry; (b) is the mesh configuration in central section. The computations are conducted with 256000 cells and a CFL number equals to 0.25.

Figure 6.2 3D supercritical modelling with the 4EQ-PR model. (C, E) show the phase state (gas phase TPD = 0 and liquid phase TPD = 1) at different time instants. (D, F) show the heat capacity contours at 70 μs around the liquid core represented by isosurface between TPD = 0 and 1.

Figure 6.3 3D supercritical modelling with the 4EQ-PR model. (G) denotes different modelling regimes with regards to the variation of Tr and Pr from ref. [7]. (H) illustrates the evolution of pressure and temperature from the middle of liquid core to the out layer of the jet in the radial section with a distance of 0.5 mm from the outlet of the nozzle. (I) plots the variation of heat capacity with temperature in the radial

section at a distance of 0.5 mm from the outlet of the nozzle for case 1.1-1.2 (solid line with symbols). The dashed lines are the data from CoolProp open source library [105].

Figure 6.4 3D transcritical modelling with the 4EQ-PR model. (K,M,O,Q) show the phase state (gas phase TPD = 0, liquid phase TPD =1 and two-phase mixture TPD = 2) for four cases at different time instants. (L, N, P, R) show the mass fraction of vaporous n-dodecane for cases 2.1 and 2.2 at 46 μs and 70 μs.

Figure 6.5 Temperature-composition (T-x) diagram at P = 40 bar, 60 bar, 80 bar. Te and Tf are the equilibrium temperature and frozen temperature respectively. The scattered points are obtained from CFD modelling.

Figure 6.6 T-x diagram at the constant pressure of 106 bar for three different fuels (heptane, dodecane, hexadecane). Te is the equilibrium temperature for three different fuels (heptane, dodecane, hexadecane) with an initial temperature of 363 K.

Figure 6.7 (a) Configuration of whole computational zone, note the lower control chamber at the fuel inlet. (b) Cut slice of the computational domain. (c) Mesh illustration in the cut plane, note that only the near nozzle region (20 mm axial length) is well refined. (d) Zoomed region in the near nozzle zone.

Figure 6.8 Initialization of the pressure and density (needle lift = 500 μm).

Figure 6.9 Illustration of jet evolution at different time instants. The liquid denoted with blue iso-surface representing the liquid core and penetration is determined with a liquid volume fraction criterion (LVF = 0.0015) for the 4EQ-PR-EQ model results; and a criterion based on mixture mass fraction of n-C12H26 (Y_{c12h26} = 0.6) for the 4EQ-PR-Wo-EQ model results.

Figure 6.10 Illustration of rate of injection (ROI) from 4EQ-PR-EQ, 4EQ-PR-Wo-EQ models, as well as the predictive data by using the injection rate model [113]**.**

Figure 6.11 Illustration of liquid and vapor penetration for 4EQ-PR-EQ and 4EQ-PR-Wo-EQ models compared to experimental data from ECN website (https://ecn.sandia.gov/bkldaal4liquid/), referred to in [112], [114] The evaluation of

vapor penetration is based on the mass fraction of n- C12H26 ($Yc12h26$ = {0.015, 0.01, 1e-5}) for 4EQ-PR-Wo-EQ model. The penetration length determined by vaporous n-C12H26 is also evaluated for 4EQ-PR-EQ model. The evaluation of liquid penetration is based on the liquid volume fraction with a critical value of 0.0015 (LVF = 0.0015) for 4EQ-PR-EQ and the mass fraction of n-C12H26 at the critical values of 0.6 (Y_{c12h26} = 0.6) for 4EQ-PR-Wo-EQ model. The penetration length determined by the liquid volume fraction of 0.0015 (LVF = 0.0015) is also evaluated for 4EQ-PR-Wo-EQ model.

Figure 6.12 Validations of mixture mass fraction (Left side) and velocity (Right side) with experiments at an axial distance of 19.84 mm and 17.5 mm from the nozzle exit respectively. The instaneous LES results (green solid line) and the average value (red bold line) are from 4EQ-PR-Wo-EQ model. The experimental data (blue dash line) are referred to [114], [115].

Figure 6.13 T-X diagram of n-C12H26 and N2 system at a pressure of 60 bar. TE denotes the equilibrium temperature between the mixture. TF symbols the frozen temperature or adiabatic mixing temperature. The red scattered points are obtained from CFD modelling with 4EQ-PR-EQ model at t = 50 μs. The blue scattered points are obtained from CFD modeling with 4EQ-PR-Wo-EQ model at t = 50 μs.

Figure 6.14 (a) depicts two-phase region in the jet by using an iso-surface of TPD = 2 at t = 62 μs.(b) illustrates the evolution of vapor mole fraction (ψ_{vap}) in the two-phase region at t = 62 μs.(c) illustrates the variation of mole fraction of n-dodecane (z_{c12h26}) in the two-phase region at t = 62 μs. Figure (d) illustrates the variation of speed of sound (Cs)in the two-phase region at t = 62 μs. (e) illustrates the evolution of volume fraction of gas (α_{gas}) (N2+ $_{C12H26}$) in the two-phase region at t = 62 μs. (f) demonstrates the variation of the mixture sound speed (Cs) with the gas volume fraction (α_{gas}) (including $N2 + C12H26$) in the axial direction of the jet as depicted with the black arrow. The background contours in all pictures is the temperature field with the legend shown in (a).

Figure 6.15 (a, d, f) depict the density of mixture fluid (ρ_{mix}), vaporous dodecane ($\rho_{c12h26,vapor}$) and N2 in liquid phase($\rho_{n2,liquid}$) in the two-phase zone of the jet at the time of 62 μs, respectively. (b, c, e) demonstrate the evolution of volume fraction of liquid phase (α_{liquid}), mass fraction of vaporous n-C12H26 ($Y_{c12h26,vapor}$)and dissolved N2 in the liquid phase ($Y_{n2,liquid}$) in the two-phase region at the time of 62μs, respectively. The background contour in all the pictures is the temperature field with the legend in Figure 6.14 (a).

Figure 6.16 Evolution of temperature and pressure at an early time sequence from CFD modelling with 4EQ-PR-EQ model. Fig.(a, b, c) denotes the pressure variation and Fig.(d, e, f) illustrate the evolution of temperature variation.

Figure 6.17 Demonstration of the axial direction from the sac to the chamber.

Figure 6.18 (a) denotes the evolution of pressure and temperature from the sac to the chamber. (b) depicts the variation of compressibility factor and density from the sac to the chamber.

Figure 6.19 Illustration of early jet evolution for case 1 (Ta = 1200 K, Pa = 8 MPa). The liquid penetration length marked with blue iso-contour is presented with the criterion of LVF ={0.0015}. The left column is the experimental pictures snapped directly from ECN website (https://ecn.sandia.gov/dbi675/). The right column corresponds to the results of 4EQ-PR-EQ model.

Figure 6.20 Illustration of early jet evolution for case 2 (Ta = 700 K, Pa = 4.6 MPa). The liquid penetration length marked with blue iso-contour is presented with the criterion of LVF = {0.0015}. The left column is the experimental pictures snapped directly from ECN website (https://ecn.sandia.gov/dbi675/). The right column corresponds to the results of 4EQ-PR-EQ model.

Figure 6.21 Demonstration of the mass fraction of vaporous dodecane ($Y_{c12h26,vapor}$) for case 1 (Fig. (a, b)) and Case2 (Fig. (c, d)) at a time instant of 66 μs. The two-phase zone is presented with the iso-volume of TPD equalling 2 as shown the white zone in Fig. (a, c).

List of Tables

Nomenclature

T_c	Critical temperature	P_c	Critical pressure
T_r	Reduced temperature: T/T_c	P_r	Reduced pressure: P/P_c
a, b	Coefficients in PR EoS	A, B	Coefficients in PR EoS
ψ_v	Vapor mole fraction	ϕ	Fugacity coefficient
v	Specific volume	ω	Acentric factor
R_g	Universal gas number	Y	Mass fraction
x_i, y_i	Phase composition	z_i	Mole fraction of component (feed)
$\dot{m}$	Ratio of Mass change	Pr	Prandtl number
$f_{liquid}, f_l, f_{gas}, f_g$	Liquid, gas fugacity	α_g	Gas volume fraction
ρ	Density	e	Internal energy
K_i	Equilibrium constant for each component	ε	Tolerance
Δt	Time-step	C_s	Speed of sound
M_w	Molar weight	Z	Compressibility factor
VLE	Vapor Liquid Equilibrium	VOF	Volume of Fluid
ECN	Engine Combustion Network	SGS	Sub-grid scale
BWR	Benedict–Webb–Rubin	PR EoS	Peng Robinson Equation of State
1D, 3D	One-, three-dimensional	DIM	Diffused interface model

BIP/$k_{i,j}$	Binary interaction factor	SG Eos	Stiffened Gas Equation of State
HTHP	High temperature high pressure	ICE	Internal combustion engine
4EQ-PR	Four equation model closed with Peng Robinson EoS	6EQ-PR	Six equation model closed with Peng Robinson EoS
4EQ-SG	Four equation model closed with Stiffened Gas EoS	TP flash	Isothermal-isobaric flash
TPD	Tangent Plane Distance	UV flash	Isoenergetic-Isochoric flash
4EQ-PR-EQ	Four equation model with phase equilibrium model	4EQ-PR-Wo-EQ	Four equation model without phase equilibrium model

Appendix

A. Analytical solution of cubic equation

There are three roots when solving the cubic EoS (e.g., PR EoS). In this study, an exact analytical solution of cubic EoS is adopted based on the approach of [144]. During the calculation, the non-physical meaning roots like negative or conjugate complex values will appear. However, these non-physical roots are excluded, and only real positive roots are selected. The detailed analytical solution is described as following:

$$x^3 + Ax^2 + Bx + C = 0 \tag{A. 1}$$

where, A, B and C are numerical coefficients.

Firstly, two coefficients, D and E, are defined as:

$$\mathrm{D} = (\frac{A}{3})^3 - \left(\frac{AB}{6}\right) + \frac{C}{2} \tag{A. 2}$$

$$\mathrm{E} = \left(\frac{B}{3}\right) - (\frac{A}{3})^2 \tag{A. 3}$$

Then, the discriminant is computed as $\Delta = D^2 + E^2$.

(1) If $\Delta = 0$, there are three roots with at least two equal roots as:

$$x_1 = 2\sqrt[3]{-D} - \left(\frac{A}{3}\right), x_2 = x_3 = -\sqrt[3]{-D} - \left(\frac{A}{3}\right) \tag{A. 4}$$

(2) If $\Delta > 0$, there are one real root and two complex conjugate roots. Two other coefficients F, G are defined as:

$$F = \sqrt[3]{(-D) + \sqrt{\Delta}}, \qquad G = \sqrt[3]{(-D) - \sqrt{\Delta}} \tag{A.5}$$

The roots are formulated as:

$$\begin{cases} x_1 = F + G - \left(\frac{A}{3}\right) \\ x_2 = -\left[\frac{1}{2}(F+G) + \frac{A}{3}\right] + \frac{\sqrt{3}}{2}(F-G)i \\ x_3 = -\left[\frac{1}{2}(F+G) + \frac{A}{3}\right] - \frac{\sqrt{3}}{2}(F-G)i \end{cases} \quad \text{(A.6)}$$

(3) If $\Delta < 0$, there are three real and unequal roots. A new parameter θ is defined as:

$$\theta(radians) = \arccos\left(\frac{-D}{\sqrt{-E^3}}\right) \quad \text{(A.7)}$$

The three roots are formulated as:

$$\begin{cases} x_1 = 2\sqrt{-E}\cos\left(\frac{\theta}{3}\right) - \frac{A}{3} \\ x_2 = 2\sqrt{-E}\cos\left(\frac{\theta}{3} + \frac{2}{3}\pi\right) - \frac{A}{3} \\ x_3 = 2\sqrt{-E}\cos\left(\frac{\theta}{3} + \frac{4}{3}\pi\right) - \frac{A}{3} \end{cases} \quad \text{(A. 8)}$$

References

[1] L. Selle and T. Schmitt, “Large-eddy simulation of single-species flows under supercritical thermodynamic conditions,” *Combust. Sci. Technol.*, vol. 182, no. 4–6, pp. 392–404, 2010.

[2] B. M. Devassy, C. Habchi, and E. Daniel, “Atomization Modelling of Liquid Jets Using a Two-Surface-Density Approach,” *At. Sprays*, vol. 25, no. 1, pp. 47–80, 2015.

[3] R. N. Dahms, J. Manin, L. M. Pickett, and J. C. Oefelein, “Understanding high-pressure gas-liquid interface phenomena in Diesel engines,” *Proc. Combust. Inst.*, vol. 34, no. 1, pp. 1667–1675, 2013.

[4] V. Yang, “Modeling of supercritical vaporization, mixing, and combustion processes in liquid-fueled propulsion systems,” *Proc. Combust. Inst.*, vol. 28, no. 1, pp. 925–942, 2000.

[5] J. Bellan, “Supercritical (and subcritical) fluid behavior and modeling: drops, streams, shear and mixing layers, jets and sprays,” *Prog. Energy Combust. Sci.*, vol. 26, no. 4, pp. 329–366, 2000.

[6] M. Oschwald *et al.*, “Injection of fluids into supercritical environments,” *Combust. Sci. Technol.*, vol. 178, no. 1–3, pp. 49–100, 2006.

[7] D. T. Banuti, “Crossing the Widom-line - Supercritical pseudo-boiling,” *J. Supercrit. Fluids*, vol. 98, pp. 12–16, 2015.

[8] C. Crua, J. Manin, and L. M. Pickett, “On the transcritical mixing of fuels at diesel engine conditions,” *Fuel*, vol. 208, pp. 535–548, 2017.

[9] T. Schmitt, A. Ruiz, L. Selle, and B. Cuenot, “Large-Eddy Simulation of Transcritical Round Jets,” *AIAA J.*, vol. 48, no. 9, pp. 2133–2144, 2010.

[10] M. P. J. Matheis, H. Müller, S. Hickel, “Large-eddy simulation of cryogenic jet injection at supercritical pressures,” *Sonderforschungsbereich/Transregio 40 – Annu. Rep. 2016*, pp. 131–149, 2016.

[11] A. Chiapolino, P. Boivin, and R. Saurel, “A simple phase transition relaxation solver for liquid–vapor flows,” *Int. J. Numer. Methods Fluids*, vol. 83, no. 7, pp. 583–605, 2017.

[12] J. Moreau, O. Simonin, and C. Habchi, “A numerical study of cavitation influence on diesel jet atomisation,” *19Th Annu. Meet. Inst. Liq. At. Spray Syst.*, no. September, p. Nottingham, 2004.

[13] H. Müller, C. A. Niedermeier, J. Matheis, M. Pfitzner, and S. Hickel, “Large-eddy simulation of nitrogen injection at trans- and supercritical conditions,” *Phys. Fluids*, vol. 28, no. 1, 2016.

[14] J.-P. Hickey and M. Ihme, “Large Eddy Simulation of Supercritical Mixing and Combustion for Rocket Applications,” *AIAA SciTech, 52nd Aerosp. Sci. Mtg*, no. January, pp. 1–13, 2014.

[15] G. Lacaze, A. Misdariis, A. Ruiz, and J. C. Oefelein, “Analysis of high-pressure Diesel fuel injection processes using LES with real-fluid thermodynamics and transport,” *Proc. Combust. Inst.*, vol. 35, no. 2, pp. 1603–1611, 2015.

[16] “IPPAD ITN Project-Marie Skłodowska-Curie actions (MSCA).” [Online]. Available: http://ippad-itn.eu.

[17] H. Roth, M. Gavaises, and C. Arcoumanis, “Cavitation Initiation, Its Development and Link with Flow Turbulence in Diesel Injector Nozzles,” vol. 2002, no. 724, 2002.

[18] C. Habchi, N. Dumont, and O. Simonin, “Multidimensional Simulation of Cavitating Flows in Diesel Injectors By a Homogeneous Mixture Modeling Approach,” *At. Sprays*, vol. 18, no. 2, pp. 129–162, 2008.

[19] Y. Wang, L. Qiu, R. D. Reitz, and R. Diwakar, “Simulating cavitating liquid jets using a compressible and equilibrium two-phase flow solver,” *Int. J. Multiph. Flow*, vol. 63, pp. 52–67, 2014.

[20] C. Habchi, J. Bohbot, A. Schmid, and K. Herrmann, “A comprehensive Two-Fluid Model for Cavitation and Primary Atomization Modelling of liquid

jets - Application to a large marine Diesel injector," *J. Phys. Conf. Ser.*, vol. 656, no. 1, 2015.

[21] N. Dumont, O. Simonin, and C. Habchi, "Cavitating flow in Diesel injectors and atomization: a bibliographical review," *8th Int. Conf. Liq. At. Spray Syst.*, no. July, pp. 314–323, 2000.

[22] S. Systems, "A Gibbs free Energy Relaxation Model for Cavitation Simulation in Diesel injectors Chawki Habchi 1 1:," no. September, pp. 1–4, 2013.

[23] R. D. Patterson, M. A., Kong, S. C., Hampson, G. J., & Reitz, "Modeling the effects of fuel injection characteristics on diesel engine soot and NOx emissions," *SAE Trans.*, pp. 836–852, 1994.

[24] D. L. Siebers, "Scaling liquid-phase fuel penetration in diesel sprays based on mixing-limited vaporization," *SAE Trans.*, pp. 703–728, 1999.

[25] R. Lugo, V. Ebrahimian, and C. Habchi, "A Compositional Representative Fuel Model for Biofuels - Application to Diesel Engine Modelling Objectives of this work The ReFGen procedure Case study," *SAE Tech. Pap.*, no. No. 2010-01-2183., pp. 1–23, 2010.

[26] T. Beard, P., Duclos, J. M., Habchi, C., Bruneaux, G., Mokaddem, K., & Baritaud, "Extension of lagrangian-eulerian spray modeling: Application to high pressure evaporating diesel sprays," *SAE Trans.*, pp. 1417–1434, 2000.

[27] W. Ning, R. D. Reitz, A. M. Lippert, and R. Diwakar, "Development of a Next-generation Spray and Atomization Model Using an Eulerian- Lagrangian Methodology," *17th Int. Multidimens. Engine Model. User's Gr. Meet.*, 2007.

[28] F. X. Lebas, R., Blokkeel, G., Beau, P. A., Demoulin, "Coupling vaporization model with the Eulerian-Lagrangian spray atomization (ELSA) model in diesel engine conditions(No. 2005-01-0213).," *SAE Tech. Pap.*, 2005.

[29] C. von Kuensberg Sarre, S.-C. Kong, and R. D. Reitz, "Modeling the Effects of Injector Nozzle Geometry on Diesel Sprays," in *SAE Technical Paper Series*, 1999, pp. 1375–1388.

[30] M. Battistoni, D. J. Duke, A. B. Swantek, F. Z. Tilocco, C. F. Powell, and S. Som, "Effects of Noncondensable Gas on Cavitating Nozzles," *At. Sprays*, vol. 25, no. 6, pp. 453–483, 2015.

[31] M. Battistoni, S. Som, and D. E. Longman, "Comparison of Mixture and Multifluid Models for In-Nozzle Cavitation Prediction," *J. Eng. Gas Turbines Power*, vol. 136, no. 6, p. 061506, 2014.

[32] J. Matheis and S. Hickel, "Multi-component vapor-liquid equilibrium model for LES of high-pressure fuel injection and application to ECN Spray A," *Int. J. Multiph. Flow*, no. October, 2017.

[33] C. Habchi, "a Gibbs Energy Relaxation (Germ) Model for Cavitation Simulation," *At. Sprays*, vol. 25, no. 4, pp. 317–334, 2015.

[34] et al. Yang, S., "Cavitation Modelling Using Real-Fluid Equation of State.," *Proc. 10th Int. Symp. Cavitation(CAV2018)*, 2018.

[35] Q. Xue *et al.*, "Eulerian CFD Modeling of Coupled Nozzle Flow and Spray with Validation Against X-Ray Radiography Data," *SAE Int. J. Engines*, vol. 7, no. 2, pp. 1061–1072, 2014.

[36] E. Knudsen, E. M. Doran, V. Mittal, J. Meng, and W. Spurlock, "Compressible Eulerian needle-to-target large eddy simulations of a diesel fuel injector," *Proc. Combust. Inst.*, vol. 36, no. 2, pp. 2459–2466, 2017.

[37] M. Battistoni, Q. Xue, and S. Som, "Large-Eddy Simulation (LES) of Spray Transients: Start and End of Injection Phenomena," *Oil Gas Sci. Technol. – Rev. d'IFP Energies Nouv.*, vol. 71, no. 1, p. 4, 2016.

[38] Z. Yue and R. D. Reitz, "An equilibrium phase spray model for high-pressure fuel injection and engine combustion simulations," *Int. J. Engine Res.*, vol. 20, no. 2, pp. 203–215, 2019.

[39] D. L. Siebers, "Scaling Liquid-Phase Fuel Penetration in Diesel Sprays Based on Mixing-Limited Vaporization," in *SAE Technical Paper Series*, 2010, vol. 1, pp. 703–728.

[40] B. Chehroudi, “Recent experimental efforts on high-pressure supercritical injection for liquid rockets and their implications,” *Int. J. Aerosp. Eng.*, vol. 2012, 2012.

[41] J. Oefelein, “Mixing and combustion of cryogenic oxygen-hydrogen shear-coaxial jet flames at supercritical pressure,” *Combust. Sci. Technol.*, vol. 178, no. 1–3, pp. 229–252, 2006.

[42] N. Zong and V. Yang, “Cryogenic fluid jets and mixing layers in transcritical and supercritical environments,” *Combust. Sci. Technol.*, vol. 178, no. 1–3, pp. 193–227, 2006.

[43] M. Oschwald and A. Schik, “Supercritical nitrogen free jet investigated by spontaneous Raman scattering,” *Exp. Fluids*, vol. 27, no. 6, pp. 497–506, 1999.

[44] “ECN- Engine Combustion Network.” .

[45] F. Poursadegh, J. Lacey, M. Brear, and R. Gordon, “The Direct Transition of Fuel Sprays to theDense-Fluid Mixing Regime in the Contextof Modern Compression Ignition Engines,” in *SAE Technical Paper Series*, 2018.

[46] H. Terashima and M. Koshi, “Strategy for simulating supercritical cryogenic jets using high-order schemes,” *Comput. Fluids*, vol. 85, pp. 39–46, 2013.

[47] L. Qiu and R. D. Reitz, “Simulation of supercritical fuel injection with condensation,” *Int. J. Heat Mass Transf.*, vol. 79, pp. 1070–1086, 2014.

[48] P. C. Ma, M. Ihme, and L. Bravo, “Modeling and Simulation of Diesel Injection at Transcritical Conditions,” no. May, p. arXiv preprint arXiv:1705.07232., 2017.

[49] C. Rodriguez, A. Vidal, P. Koukouvinis, and M. Gavaises, “Supercritical and transcritical real-fluid mixing using the PC-SAFT EOS,” *Proc. ILASS–Europe 2017. 28th Conf. Liq. At. Spray Syst.*, no. September, 2017.

[50] R. Saurel and R. Abgrall, “A Multiphase Godunov Method for Compressible Multifluid and Multiphase Flows,” *J. Comput. Phys.*, vol. 150, no. 2, pp. 425–467, 1999.

[51] P. C. Ma, Y. Lv, and M. Ihme, “An entropy-stable hybrid scheme for simulations of transcritical real-fluid flows,” *J. Comput. Phys.*, vol. 340, no. March, pp. 330–357, 2017.

[52] S. Kawai, H. Terashima, and H. Negishi, “A robust and accurate numerical method for transcritical turbulent flows at supercritical pressure with an arbitrary equation of state,” *J. Comput. Phys.*, vol. 300, pp. 116–135, 2015.

[53] “Simulis Thermodynamics - Calculs de propriétés de mélanges et d’équilibres entre phases, propriétés de transfert, enthalpie, entropie, analyse exergie, propriétés de compressibilité, propriétés d’écar.” .

[54] M. S. Baer and J. W. Nunziato, “A two-phase mixture theory for the deflagration to detonation (DDT) transition in reactive granular materials,” *Int. J. Multiph. Flow*, vol. 12, no. 6, pp. 861–889, 1986.

[55] J. Bohbot, N. Gillet, and A. Benkenida, “IFP-C3D: an Unstructured Parallel Solver for Reactive Compressible Gas Flow with Spray,” *Oil Gas Sci. Technol.*, vol. 64(3), no. 3, pp. 309–335, 2009.

[56] J. VIDAL, *Thermodynamics - Applications in Chemical Engineering and the Petroleum Industry 1th Edition*. 2003.

[57] F. A. Aly and L. L. Lee, “Self-consistent equations for calculating the ideal gas heat capacity, enthalpy, and entropy,” *Fluid Phase Equilib.*, vol. 6, no. 3–4, pp. 169–179, 1981.

[58] M. Trujillo, P. O’Rourke, and D. Torres, “Generalizing the Thermodynamics State Relationships in KIVA-3V,” NM (US), 2002.

[59] S. Sonntag, R. E., Borgnakke, C., Van Wylen, G. J., & Van Wyk, *Fundamentals of thermodynamics*, 6th ed. New York: Wiley., 1998.

[60] J. Mollerup and M. L. Michelsen, *Thermodynamic Models: Fundamentals & Computational Aspects*. 2004.

[61] L. E. Baker, A. C. Pierce, and K. D. Luks, “Gibbs Energy Analysis of Phase Equilibria,” *Soc. Pet. Eng. J.*, vol. 22, no. 5, pp. 1–12, 1982.

[62] M. L. Michelsen, “The isothermal flash problem. Part I. Stability,” *Fluid Phase Equilib.*, vol. 9, no. 1, pp. 1–19, 1982.

[63] Z. Li and A. Firoozabadi, “General Strategy for Stability Testing and Phase-Split Calculation in Two and Three Phases,” *SPE J.*, vol. 17, no. 04, pp. 1096–1107, 2012.

[64] C. M. Crowe and M. Nishio, “Convergence promotion in the simulation of chemical processes—the general dominant eigenvalue method,” *AIChE J.*, vol. 21, no. 3, pp. 528–533, 1975.

[65] M. L. Michelsen, “The isothermal flash problem. Part II. Phase split calculation.,” *Fluid Phase Equilib.*, vol. 9, pp. 21–40, 1982.

[66] J. F. Boston and H. I. Britt, “A radically different formulation and solution of the single-stage flash problem,” *Comput. Chem. Eng.*, vol. 2, no. 2–3, pp. 109–122, 1978.

[67] J. E. Dennis, Jr and R. B. Schnabel, *Numerical Methods for Unconstrained Optimization and Nonlinear Equations*. 1996.

[68] H. Hoteit and A. Firoozabadi, “Simple phase stability-testing algorithm in the reduction method,” *AIChE J.*, vol. 52, no. 8, pp. 2909–2920, 2006.

[69] D. Vladimir *et al.*, “Phase stability analysis with cubic equations of state by using a global optimization method,” *Fluid Phase Equilib.*, vol. 197, pp. 411–437, 2002.

[70] N. Saber and J. M. Shaw, “Rapid and robust phase behaviour stability analysis using global optimization,” *Fluid Phase Equilib.*, vol. 264, no. 1–2, pp. 137–146, 2008.

[71] R. K. Mehra, R. A. Heidemann, and K. Aziz, “An accelerated successive substitution algorithm,” *Can. J. Chem. Eng.*, vol. 61, no. 4, pp. 590–596, 1983.

[72] P. Gill and W. Murray, “Quasi-Newton methods for unconstrained optimization,” *IMA J. Appl. Math.*, no. February, pp. 91–108, 1972.

[73] D. V. Nichita, S. Gomez, and E. Luna, “Multiphase equilibria calculation by

direct minimization of Gibbs free energy with a global optimization method," *Comput. Chem. Eng.*, vol. 26, no. 12, pp. 1703–1724, 2002.

[74] R. Okuno, R. T. Johns, and K. Sepehrnoori, "A New Algorithm for Rachford-Rice for Multiphase Compositional Simulation," *Spe J.*, vol. 15, no. 2, pp. 313–325, 2010.

[75] C. H. Whitson and M. L. Michelsen, "The negative flash," *Fluid Phase Equilib.*, vol. 53, no. C, pp. 51–71, 1989.

[76] S. Saha and J. J. Carroll, "The isoenergetic-isochoric flash," *Fluid Phase Equilib.*, vol. 138, pp. 23–41, 1997.

[77] F. M. Gonçalves, M. Castier, and O. Q. F. Araújo, "Dynamic simulation of flash drums using rigorous physical property calculations," *Brazilian J. Chem. Eng.*, vol. 24, no. 2, pp. 277–286, 2007.

[78] E. R. A. Lima, M. Castier, and E. C. Biscaia, "Differential-algebraic approach to dynamic simulations of flash drums with rigorous evaluation of physical properties," *Oil Gas Sci. Technol.*, vol. 63, no. 5, pp. 677–686, 2008.

[79] M. Castier, "Solution of the isochoric-isoenergetic flash problem by direct entropy maximization," *Fluid Phase Equilib.*, vol. 276, no. 1, pp. 7–17, 2009.

[80] M. L. Michelsen, "State function based flash specifications," *Fluid Phase Equilib.*, vol. 158, pp. 617–626, 1999.

[81] T. García-Córdova, D. N. Justo-García, B. E. García-Flores, and F. García-Sánchez, "Vapor-liquid equilibrium data for the nitrogen + dodecane system at temperatures from (344 to 593) K and at pressures up to 60 MPa," *J. Chem. Eng. Data*, vol. 56, no. 4, pp. 1555–1564, 2011.

[82] G. Silva-Oliver, G. Eliosa-Jiménez, F. García-Sánchez, and J. R. Avendaño-Gómez, "High-pressure vapor-liquid equilibria in the nitrogen-n-pentane system," *Fluid Phase Equilib.*, vol. 250, no. 1–2, pp. 37–48, 2006.

[83] G. Eliosa-Jiménez, G. Silva-Oliver, F. García-Sánchez, and A. De Ita De La Torre,

"High-pressure vapor-liquid equilibria in the nitrogen + n-hexane system," *J. Chem. Eng. Data*, vol. 52, no. 2, pp. 395–404, 2007.

[84] F. García-Sánchez, G. Eliosa-Jiménez, G. Silva-Oliver, and A. Godínez-Silva, "High-pressure (vapor + liquid) equilibria in the (nitrogen + n-heptane) system," *J. Chem. Thermodyn.*, vol. 39, no. 6, pp. 893–905, 2007.

[85] T. FLÅTTEN and H. LUND, "RELAXATION TWO-PHASE FLOW MODELS AND THE SUBCHARACTERISTIC CONDITION," *Math. Model. Methods Appl. Sci.*, vol. 21, no. 12, pp. 2379–2407, 2011.

[86] A. Zein, M. Hantke, and G. Warnecke, "Modeling phase transition for compressible two-phase flows applied to metastable liquids," *J. Comput. Phys.*, vol. 229, no. 8, pp. 2964–2998, 2010.

[87] B. E. Poling, J. M. Prausnitz, and J. P. O'Connell, *The Properties of Gases and Liquids*. 2001.

[88] L. Qiu, "Development of a Phase Stability-Based Fuel Condensation Model for Advanced Low Temperature Combustion Engines By," 2014.

[89] T. C. Horng, M. Ajlan, L. L. Lee, K. E. Starling, and M. Ajlan, "Generalized Multiparameter Correlation for Nonpolar and Polar Fluid Transport Properties," *Ind. Eng. Chem. Res.*, vol. 27, no. 4, pp. 671–679, 1988.

[90] R. Saurel, P. Boivin, and O. Le Métayer, "A general formulation for cavitating, boiling and evaporating flows," *Comput. Fluids*, vol. 128, pp. 53–64, 2016.

[91] A. Chiapolino, P. Boivin, and R. Saurel, "A simple and fast phase transition relaxation solver for compressible multicomponent two-phase flows," *Comput. Fluids*, vol. 150, pp. 31–45, 2017.

[92] G. Allaire, S. Clerc, and S. Kokh, "A five-equation model for the simulation of interfaces between compressible fluids," *J. Comput. Phys.*, vol. 181, no. 2, pp. 577–616, 2002.

[93] "A Textbook of Sound. A. B. Wood. Third Edition. Bell, London, 1955. 610 pp. Illustrated. 42s.," *J. R. Aeronaut. Soc.*, 2016.

[94] P. Embid and M. Baer, “Mathematical analysis of a two-phase continuum mixture theory,” *Contin. Mech. Thermodyn.*, vol. 4, no. 4, pp. 279–312, 1992.

[95] A. K. Kapila, R. Menikoff, J. B. Bdzil, S. F. Son, and D. S. Stewart, “Two-phase modeling of deflagration-to-detonation transition in granular materials: Reduced equations,” *Phys. Fluids*, vol. 13, no. 10, pp. 3002–3024, 2001.

[96] C. J. Wareing, R. M. Woolley, M. Fairweather, and S. A. E. G. Falle, “A composite equation of state for the modeling of sonic carbon dioxide jets in carbon capture and storage scenarios,” *AIChE J.*, vol. 59, no. 10, pp. 3928–3942, 2013.

[97] P. Yi, S. Yang, C. Habchi, and R. Lugo, “A multicomponent real-fluid fully compressible four-equation model for two-phase flow with phase change,” *Phys. Fluids*, vol. 31, no. 2, p. 026102, 2019.

[98] C. Pantano, R. Saurel, and T. Schmitt, “An oscillation free shock-capturing method for compressible van der Waals supercritical fluid flows,” *J. Comput. Phys.*, vol. 335, pp. 780–811, 2017.

[99] R. Abgrall, “How to prevent oscillations in multicomponent flow calculations: A quasi conservative approach,” *J. Comput. Phys.*, vol. 125, pp. 150–160, 1996.

[100] P. J. Linstrom and W. G. Mallard, “The NIST Chemistry WebBook: A chemical data resource on the Internet,” *J. Chem. Eng. Data*, vol. 46, no. 5, pp. 1059–1063, 2001.

[101] D. J. Duke *et al.*, “X-ray radiography of cavitation in a beryllium alloy nozzle,” *Int. J. Engine Res.*, vol. 18, no. 1–2, pp. 39-50., 2017.

[102] B. Li, Y. Gu, and M. Chen, “An experimental study on the cavitation of water with dissolved gases,” *Exp. Fluids*, vol. 58, no. 12, pp. 1–9, 2017.

[103] D. J. Duke, A. L. Kastengren, A. B. Swantek, K. E. Matusik, and C. F. Powell, “X-ray fluorescence measurements of dissolved gas and cavitation,” *Exp. Fluids*, vol. 57, no. 10, pp. 1–14, 2016.

[104] D. J. Duke, A. L. Kastengren, F. Z. Tilocco, A. B. Swantek, and C. F. Powell,

"X-Ray Radiography Measurements of Cavitating Nozzle Flow," *At. Sprays*, vol. 23, no. 9, pp. 841–860, 2013.

[105] I. H. Bell, J. Wronski, S. Quoilin, and V. Lemort, "Pure and pseudo-pure fluid thermophysical property evaluation and the open-source thermophysical property library coolprop," *Ind. Eng. Chem. Res.*, vol. 53, no. 6, pp. 2498–2508, 2014.

[106] C. Habchi, D. Verhoeven, C. Huynh Huu, L. Lambert, J. L. Vanhemelryck, and T. Baritaud, "Modeling Atomization and Break Up in High-Pressure Diesel Sprays," in *SAE Technical Paper Series*, 1997, pp. 1391–1406.

[107] P. C. Ma, H. Wu, D. T. Banuti, and M. Ihme, "On the numerical behavior of diffuse-interface methods for transcritical real-fluids simulations," *Int. J. Multiph. Flow*, vol. 113, pp. 231–249, 2019.

[108] R. Yang, S., Habchi, C., Yi, P., Lugo, "Towards a multicomponent real-fluid fully compressible two-phase flow model.," in *ICLASS 14th Triennial International Conference on Liquid Atomization and Spray Systems*, 2018.

[109] J. Manin, L. M. Pickett, and K. Yasutomi, "Transient cavitation in transparent diesel injectors," in *ICLASS 14th Triennial International Conference on Liquid Atomization and Spray Systems*, 2018.

[110] R. Payri, J. Gimeno, P. Marti-Aldaravi, and M. Carreres, "Assessment on Internal Nozzle Flow Initialization in Diesel Spray Simulations," in *SAE Technical Paper Series ,No. 2015-01-0921*, 2015.

[111] L. M. Pickett, C. L. Genzale, and J. Manin, "UNCERTAINTY QUANTIFICATION FOR LIQUID PENETRATION OF EVAPORATING SPRAYS AT DIESEL-LIKE CONDITIONS," *At. Sprays*, vol. 25, no. 5, 2015.

[112] L. M. Pickett, C. L. . Genzale, and J. Manin, "Measurement Uncertainty of Liquid Penetration in Evaporating Diesel Sprays," in *ILASS2011-111*, 2011.

[113] "CMT-Motores Térmicos, Rate of Injection Model," 2015. .

[114] L. M. Pickett, J. Manin, C. L. Genzale, D. L. Siebers, M. P. B. Musculus, and C. A.

Idicheria, “Relationship Between Diesel Fuel Spray Vapor Penetration/Dispersion and Local Fuel Mixture Fraction,” *SAE Int. J. Engines*, vol. 4, no. 1, pp. 764-799., 2011.

[115] L. M. T. Meijer, M., & Somers, “Engine Combustion Network:" Spray A" basic measurements and advanced diagnostics,” in *Proceedings of the 12th International Conference on Liquid Atomization and Spray Systems, ICLASS*, 2012.

Résumé étendu

Pour satisfaire aux dernières réglementations en matière d'émissions, des progrès importants sont encore attendus des moteurs à combustion interne. De plus, améliorer l'efficacité du moteur pour réduire les émissions et la consommation de carburant est devenu plus essentiel qu'auparavant. Mais, de nombreux phénomènes complexes restent mal compris dans ce domaine, tels que le processus d'injection de carburant. Les méthodes d'investigation du processus d'injection de carburant comprennent la modélisation numérique et l'observation expérimentale. Cependant, les conditions de fonctionnement extrêmes dans la chambre, telles qu'une pression élevée et une température élevée, ont posé de sérieux problèmes pour les études expérimentales. D'autre part, avec le développement continu du matériel informatique, la modélisation numérique devient de plus en plus répandue. Actuellement, de nombreux logiciels pour la dynamique des fluides numérique (CFD) prenant en compte les changements de phase (tels que la cavitation) et la modélisation d'injection ont été développés et utilisés avec succès dans le processus d'injection. Néanmoins, il existe peu de codes CFD capables de simuler avec précision les conditions d'injection transcritiques, d'une condition de température de carburant

sous-critique à un mélange supercritique dans la chambre de combustion. En effet, la plupart des modèles existants ne peuvent simuler que des écoulements monophasés, éventuellement dans des conditions supercritiques, ou des écoulements diphasiques dans des conditions sous-critiques. Par conséquent, un modèle complet capable de traiter les conditions transcritiques, y compris la transition de phase possible entre les régimes sous-critique et supercritique, ou entre les flux monophasiques et diphasiques, manque de manière dynamique. Le but de cette thèse est de relever ce défi. À cette fin, des modèles d'écoulement de fluide réel diphasique compressible basés sur une approche eulérienne-eulérienne tenant compte de l'équilibre de phase ont été développés et discutés dans le présent travail.

La thèse est basée sur le code interne, IFP-C3D. Dans le code d'origine, il inclut le modèle classique d'écoulement en deux phases à 7 équations. Dans le système à 7 équations, le débit de gaz et le débit de liquide sont résolus indépendamment avec une équation d'état différente. Pour le flux de gaz, la loi des gaz idéale est appliquée. L'EoS sous gaz renforcé est utilisé pour le flux de liquide. L'objectif principal étant de développer un modèle capable de simuler l'injection transcritique à haute température et sous haute

pression, l'EoS d'origine ne peut pas satisfaire les conditions. Par conséquent, le nouveau modèle basé sur l'EoS à fluide réel doit être développé.

Plus précisément, sur la base du système à 7 équations, un modèle à 6 équations entièrement compressible comprenant des équations de bilan de phase liquide et gazeuse résolues séparément; et un modèle à 4 équations qui résout les équations des équilibres liquide et gazeux en équilibre mécanique et thermique sont proposés dans ce manuscrit. L'équation d'état de Peng-Robinson EoS est sélectionnée pour fermer les deux systèmes et pour traiter les éventuels changements de phase et la transition ou la séparation de phase. En particulier, un résolveur d'équilibre de phase a été développé et validé. Ensuite, une série de tests académiques 1D sur les phénomènes d'évaporation et de condensation réalisés dans des conditions sous-critiques et supercritiques a été simulée et comparée aux données de la littérature et aux résultats académiques disponibles. Ensuite, des modèles d'écoulement à deux phases entièrement compressibles (systèmes à 6 équations et à 4 équations) ont été utilisés pour simuler les phénomènes de cavitation dans une buse 3D de taille réelle afin d'étudier l'effet de l'azote dissous sur la création et le développement de la cavitation. Le bon accord avec les

données expérimentales prouve que le solveur proposé est capable de gérer le comportement complexe du changement de phase dans des conditions sous-critiques. Enfin, la capacité du solveur à traiter l'injection transcritique à des pressions et à des températures élevées a été validée par la modélisation réussie de l'injecteur Spray A du réseau de combustion du moteur (ECN).